

Alma Mater Studiorum – Università di Bologna

DOTTORATO DI RICERCA IN

CHIMICA

Ciclo XXXII

Settore Concorsuale: 03/B1

Settore Scientifico Disciplinare: CHIM/03

STATIC AND DYNAMIC CRYSTAL ENGINEERING: TOWARDS NEW
MATERIALS BASED ON BORONIC ACIDS AND SOLID-STATE
MOLECULAR MOTION

Presentata da: Luca Fornasari

Coordinatore Dottorato

Prof. Domenica Tonelli

Supervisore

Prof. Dario Braga

Esame finale anno 2020

Index

Abstract.....	1
Chapter 1 - Introduction.....	2
1.1 Crystal Engineering.....	3
1.1.1 Self-assembly and intermolecular interactions	5
1.2 Aim of the work.....	9
References.....	10
Chapter 2 - Crystal Engineering of Boronic Acids.....	12
2.1 Overview	13
2.1.1 Interactions.....	14
References.....	17
2.2 Self-Assembly and Exfoliation of a Molecular Solid Based on Cooperative B–N and Hydrogen Bonds	19
2.2.1 Conclusions	25
References.....	26
2.3 Zwitterionic Systems Obtained by Condensation of Heteroaryl- Boronic Acids and Rhodizonic Acid	28
2.3.1 Introduction	28
2.3.2 Results and Discussion.....	30
2.3.3 Conclusions	42
2.3.4 Experimental Section	43
References.....	46
2.4 Supramolecular Zwitterions Based on a Novel Boronic Acid–Squarate Dianion Synthons.....	48
2.4.1 Introduction	48
2.4.2 Experimental	50
2.4.3 Results and discussion.....	52

2.4.4 Conclusions	56
References	57
Chapter 3 - Crystal Engineering and Solid-State Molecular Motion	60
3.1 Overview	61
3.1.1 Orientational motion in crystals	63
3.1.2 Design principles	65
References	66
3.2 Precessional Motion in Crystalline Solid Solutions of Ionic Rotors ..	69
3.2.1 Introduction	69
3.2.2 Results and discussion.....	72
3.2.3 Conclusions	81
3.2.4 Experimental Section	82
References	85
3.3 Solid-state Dynamics and High-pressure Studies of a Supramolecular Spiral Gear.....	87
3.3.1 Introduction	87
3.3.2 Experimental Section	90
3.3.3 Results and Discussion.....	94
3.3.4 Conclusions	103
3.3.5 Supporting Information.....	104
References	114
3.4 Binary and Ternary Solid Solutions of Ionic Plastic Crystals, and Modulation of Plastic Phase Transitions	116
3.4.1 Introduction	116
3.4.2 Experimental section	119
3.4.3 Results and discussion.....	121
3.4.4 Conclusions	130
References	131
Chapter 4 - Summary	133

Abstract

The ultimate goal of crystal engineering is *making crystals with a purpose*. This means designing *de novo* molecular solids possessing precise structural and physicochemical properties and inducing subtle modifications to conveniently modulate said properties.

In the continuous quest for novel crystalline materials, it is of fundamental importance to search for new building blocks, explore new interaction modes and new strategies for the modification of the structural properties of solids, such as the formation of co-crystals, salts, complexes or solid solutions.

The research activity performed in my PhD was mainly dedicated to two topics:

1. the design and synthesis of new single-component and multi-component assemblies based on hetero-aryl boronic acids and the investigation of their recognition features;
2. the study of molecular motion in some crystalline complexes and salts and the modification of those dynamics through the principles of crystal engineering.

The first topic is addressed in the second chapter of this thesis. A number of different solid forms were obtained exploiting the various interaction modes of some simple and inexpensive boronic acids, including an exfoliable layered co-crystal, supramolecular zwitterions, a polymeric ternary co-crystal and covalent zwitterionic adducts. The third chapter is dedicated to the latter topic. Supramolecular crystalline complexes and salts possessing parts in rapid motion were synthesised and characterised by means of combined XRD and solid-state NMR analyses. The formation of solid solutions was successfully employed to fine-tune the dynamical properties of those compounds. Finally, the high-pressure behaviour of some supramolecular crystalline *rotors* was studied by using diamond anvils cells (DACs).

Chapter 1

Introduction

1.1 Crystal Engineering

The first use of the term crystal engineering is commonly attributed to Schmidt. In the late 1960s, while studying the effect of crystal packing on photo-activated cyclization reactions of olefins, he wrote: *“The systematic development of our subject will be difficult if not impossible until we understand the intermolecular forces responsible for the stability of the crystalline lattice of organic compounds: a theory of the organic solid state is a requirement for the eventual control of molecular packing arrangement. Once such a theory exists we shall, in the present context of synthetic and mechanistic photochemistry, be able to ‘engineer’ crystal structures having intermolecular contact geometries appropriate for chemical reaction, much as, in other context, we shall construct organic conductors, catalysts, etc.”*¹

Crystal engineering has since developed into an established discipline that stands at the intersection between different fields of research: supramolecular chemistry, nanochemistry and molecular machines, solid-state chemistry and chemistry of materials.² Its goal is essentially to achieve a complete understanding of the intermolecular interactions governing the assembly of molecules and ions in the solid state and to exploit such understanding in the design and synthesis of solids with predetermined chemical and physical properties.

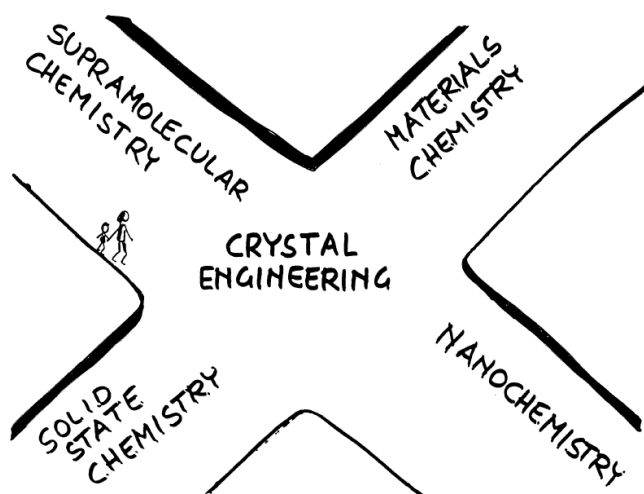


Figure 1.1.1 Molecular crystal engineering can be seen as the logical intersection between the route leading from supramolecular chemistry to nanochemistry and molecular machines and the route leading from solid state chemistry to a molecular-based chemistry of materials. (reproduced from ref. 2)

It is clear, therefore, that crystal engineering shares many traits with supramolecular chemistry.^{3,4} By the words of Dunitz, a crystal is “*the supermolecule par excellence*”,⁵ in that crystals are defined by the periodic arrangement of numbers of Avogadro of molecules connected by the same non-covalent interactions responsible for supramolecular recognition, and the properties are determined by the collection of molecules as a whole rather than the single component.

This concept is not just a theoretical exercise, it is of fundamental importance in defining crystal engineering as a method that applies a retrosynthetic approach to crystal making.^{6,7} The final product, *i.e.* the solid with desired properties, is obtained through the stages of modeling, synthesis, characterisation and evaluation of the properties.

Modeling is exemplified by the words of Etter: “*Organizing molecules into predictable arrays is the first step in a systematic approach to designing organic solid-state materials*”. In substance, the “prior art” is examined to retrieve information on intermolecular interactions and recognition, then this knowledge is utilised to design molecular building blocks containing a combination of characteristics (functional groups, shape, symmetry, charge, acidity/basicity etc.) such that they will organise in a predictable manner. This aspect, together with the study of the nucleation/crystal growth process and the solid-state chemical reactivity, contributes to developing a synthetic strategy in the context of crystal making.

However, it should be kept in mind that predicting the crystal structure of a given molecule is still essentially a crystal engineer’s dream. The outcome of crystallization is the optimization of such a vast number of interactions that is, in fact, impossible to grasp *a priori*, moreover, such optimization is highly dependent on the experimental conditions. A given crystal structure is just one out of an often large number of energy minima in the thermodynamic landscape of a crystal; even the most indiscernible change can lead the process to a different minimum. The phenomenon of polymorphism⁹⁻¹³ is an example of how the final goal of crystal engineering remains ambitious despite the progress made in this discipline.

1.1.1 Self-assembly and intermolecular interactions

Self-assembly can be defined as: “*The spontaneous and reversible association of molecular species to form larger, more complex supramolecular entities according to the intrinsic information contained in the components*”.¹⁴ This definition is rather generic in view of the broadening it has undergone over time to encompass many aspects of intermolecular association in different fields, ranging from biochemistry and macromolecules to nanotechnology. Nevertheless, some key concepts, deeply connected with crystal engineering, are expressed here.

The assembly is spontaneous, so the system arranges itself. The control that can be exerted by the synthetic chemist is therefore limited to “program” the assembly process by designing building blocks that contain the appropriate information and finding suitable experimental conditions. The information is primarily delivered by functional groups in the way they interact with each other and form intermolecular contacts. In a typical self-assembly process, a large number of interactions of different types are present; the system then optimises the set of interactions to reach a minimum in the thermodynamic landscape. It is usually assumed that the optimisation proceeds starting from those interactions that provide the greatest stabilisation to the system, followed by the weaker ones. For this reason, in designing the building blocks it is crucial to correctly envision a hierarchy amongst the various interactions at play.

An invaluable tool to this end is represented by the Cambridge Structural Database (CSD),¹⁵ that to date counts more than one million crystal structures of organic and metal-organic compounds. The CSD is routinely analysed to assess the statistical occurrence and the chemical and structural features of interaction motifs. Coherently to the retrosynthetic approach discussed above, *supramolecular synthons* are identified, i.e. “*structural units within supermolecules which can be formed and/or assembled by known or conceivable synthetic operations involving intermolecular interactions*” according to the definition proposed by Desiraju.⁷ A key concept is the robustness of a synthon, that is connected to its occurrence in crystal assemblies versus other competing intermolecular interaction motifs.

It is then useful to introduce the complementary term *tecton*,^{16–18} based on the assumption that control over “*specific architectural or functional features*”

of the assembly can be achieved by tuning “*particular associative forces*”. While the definition of synthon is operative and mostly derived in a *bottom-up* fashion from the data mining approach to crystal synthesis, the idea of molecular tectonics implies *top-down* decoding and encoding of the intermolecular recognition phenomena based on chemical reasoning. The molecular tectonics approach is useful in the design of extended networks formed by *multi-component* assemblies, however, it should be noted that it is based on the assumption of self-repair of the process. In other words, every step in the self-assembly process is completely reversible and thus lead the system to the most thermodynamically stable product. As discussed above, this is rarely the case in a crystallisation, since the kinetical bias often diverts the process to a local thermodynamic minimum and hence a metastable product.

Supramolecular species are held together by non-covalent interactions. The energies involved range from ca. 300 kJ/mol for ion-ion interactions, comparable to covalent bonds, to 1-2 kJ/mol for dispersion interactions (see Table 1.1.1). A brief overview of the main non-covalent interactions is given below.

Table 1.1.1 Summary of supramolecular interactions

Interaction	Strength (kJ/mol)
Ion-ion	200-300 ^a
Ion-dipole	50-200 ^a
Dipole-dipole	5-50 ^a
Hydrogen bonding	4-120 ^a
Halogen-bonding	10-150 ^b
π - π	0-50 ^a
van der Waals	<5 ^a

^aobtained from ref. 14; ^bobtained from ref. 19

*Ionic and dipolar interactions*²⁰

Based on the Coulombic forces acting between electrostatic charges, can be divided in (i) ion-ion interactions, (ii) ion-dipole interactions and (iii) dipole-dipole interactions. Their nature is non-directional, however, interactions involving dipoles require some degree of alignment of the species in order to optimise the attraction and repulsion factors. Ionic interactions are

significantly stronger since ions have a higher charge density and they are predominant at long range. Some notable examples are the cation-anion interactions in common salts and the complexes forming between crown-ethers and alkali metal cations.²¹

*Hydrogen bonding*²²

It can be seen as a special kind of dipole-dipole interaction between a proton donor (D) and an acceptor (A). Donors are groups with a hydrogen atom attached to an electronegative atom (e.g. oxygen or nitrogen) so that a dipole is formed with a partial positive charge on the H-atom; acceptors, on the other hand, are groups terminating with an electron-rich atom that can interact with the electron-accepting H-atom. Sometimes one or both of the groups involved in a hydrogen bond can bear a formal charge, as in the case of $[\text{N-H}]^+$ donors or carboxylate acceptors. In such cases the hydrogen bond is termed *charged-assisted*, it is usually stronger than its “neutral” counterpart and it is somewhat more similar in character to a covalent bond.

Hydrogen bonds are highly directional as there exists a correlation between the angle $\text{D-H}\cdots\text{A}$ and the strength (and therefore length) of the bond. It is common to divide H-bonds into three categories: (i) strong bonds are close to linearity ($175\text{-}180^\circ$), their energies are in the range $60\text{-}120$ kJ/mol and the $\text{D}\cdots\text{A}$ lengths are $2.2\text{-}2.5$ Å; (ii) moderate bonds have angle in the range $130\text{-}180^\circ$, energy $16\text{-}60$ kJ/mol and length $2.5\text{-}3.2$ Å; (iii) weak bonds are characterised by angles in the range $90\text{-}150^\circ$, energies < 12 kJ/mol and $\text{D}\cdots\text{A}$ lengths $3.2\text{-}4.0$ Å.

The specific geometric features of hydrogen bonds, together with the natural abundance of hydrogen-bearing groups have determined their broad success in crystal engineering and supramolecular chemistry in general as a tool for the design of complex architectures.

*Halogen bonding*¹⁹

The definition proposed by the IUPAC states: “A halogen bond occurs when there is evidence of a net attractive interaction between an electrophilic region associated with a halogen atom in a molecular entity and a nucleophilic region in another, or the same, molecular entity”.²³ Parallelism can, therefore, be seen

between the hydrogen and halogen bonding, except in the latter a halogen atom acts as the electron acceptor.

Similar to hydrogen bonds, halogen bonds are usually schematised as D-X \cdots A, where X=F, Cl, Br, I; The bonds strength follows the trend I>Br>Cl>F, with I-atoms forming the strongest bonds, while interactions involving F-atoms are rare. Moreover, halogen bonds have directional character, with a preference for linear arrangements.

π - π interactions

π - π are *de facto* interactions best referred to as *aromatic interactions*.²⁴ The interaction arises from a combination of electrostatic, van der Waals and charge transfer effects and it is highly case dependent.^{25,26} Although the phenomenon is not theoretically well understood, it is convenient to use the “ π - π ” denomination as a geometric descriptor of the interaction in unsaturated molecules. The most common interaction modes are defined as *face-to-face* (or *π -stacked*) and *T-shaped*. The former is established, for example, between two parallel aromatic rings offset at a distance of approximately 3.5 Å; in the latter, one aromatic ring interacts in a perpendicular orientation with the second ring. An example of face-to-face aromatic interactions is observed in the layered structure of graphite.

Van der Waals interactions⁴

The term van der Waals interactions indicate dispersion effects arising from fluctuations of the electron density distribution in molecules that are in proximity to one another. These effects comprise two attractive components, the *London forces* and *Debye forces*, and a repulsive component, the *exchange and repulsion* interaction. The fluctuations in the electron density create instantaneous multipoles that tend to interact with each other. The London forces act between instantaneous multipoles, while the Debye forces act between instantaneous and permanent dipoles. The repulsive component accounts for both transient electrostatic repulsion and quantum mechanical repulsion (or exchange interaction) based on the *Pauli exclusion principle*.

These interactions are non-directional and act at a very short range: the potential energy of attractive forces depends on the distance r according to $1/r^6$, while the dependence of repulsive interactions is $1/r^{12}$. Attractive van der

Waals interactions are additive and, in general, their energy is proportional to the surface area of contact. Repulsive interactions define the molecular shape and the “macroscopic” steric effect. In the solid state, the optimisation of such a multitude of interactions in order to minimise the lattice energy is the main factor governing the crystallisation, leading to the *close packing* principle.²⁷ The influence of molecular shape and volume must be kept in mind when designing the building blocks for crystal engineering, as crystal structures can as well be seen as the minimisation of repulsions other than the maximisation of interactions.

1.2 Aim of the work

The aim of my PhD research activity was two-fold:

- The study of some hetero-aryl substituted boronic acid in the context of crystal engineering. Such molecules can establish essentially three types of interactions that are relevant from a supramolecular perspective, namely H-bonds, N-B bonds and condensation with diols. The goal was, therefore, to explore how these interactions compare to each other and, consequently, to achieve a structural understanding that could be exploited to deliberately design and prepare different single-component and multi-component molecular solids.
- The design and synthesis of crystalline materials possessing components in rapid motion. These dynamical phenomena on the molecular scale have a profound influence on the physicochemical properties of the solids. The idea behind this project was to employ the principles of crystal engineering to modulate such dynamics and to characterise them using, in particular, a combination of XRD and solid-state NMR techniques.

In the next chapters, an overview of the two topics is presented, followed, for copyright reasons, by the authorised reproduction of the manuscripts that were published as part of my PhD activity. With the aim of keeping the thesis as concise as possible, the supporting information relative to published works

is not reproduced here, as it can be retrieved free of charge from the links provided at the beginning of each paragraph. Therefore, the original numbering scheme for figures and tables referring to the supporting information has been retained to help the reader.

References

- (1) Schmidt, G. M. J. Photodimerization in the Solid State. *Pure Appl. Chem.* **1971**, *27* (4), 647–678.
- (2) Braga, D.; Grepioni, F.; Orpen, A. G. *Crystal Engineering: From Molecules and Crystals to Materials*; Braga, D., Grepioni, F., Orpen, A. G., Eds.; Springer Netherlands: Dordrecht, 1999.
- (3) Lehn, J. *Supramolecular Chemistry*; Wiley, 1995.
- (4) Steed, J. W.; Atwood, J. L. *Supramolecular Chemistry: Second Edition*; John Wiley & Sons, Ltd: Chichester, UK, 2009.
- (5) Dunitz, J. D. Thoughts on Crystals as Supermolecules. In *The Crystal as a Supramolecular Entity*; John Wiley & Sons, Ltd, 2007; Vol. 2, pp 1–30.
- (6) Desiraju, G. R. *Crystal Engineering: The Design of Organic Solids*; Elsevier: Amsterdam and New York, 1989.
- (7) Desiraju, G. R. Supramolecular Synthons in Crystal Engineering—A New Organic Synthesis. *Angew. Chemie Int. Ed. English* **1995**, *34* (21), 2311–2327.
- (8) Panunto, T. W.; Urbinczyk-lipkowska, Z.; Johnson, R.; Etter, M. C. Hydrogen-Bond Formation in Nitroanilines: The First Step in Designing Acentric Materials. *J. Am. Chem. Soc.* **1987**, *109* (25), 7786–7797.
- (9) Bernstein, J. *Polymorphism in Molecular Crystals*; Clarendon Press, 2002.
- (10) Hilfiker, R. *Polymorphism: In the Pharmaceutical Industry*; Hilfiker, R., Ed.; Wiley, 2006.
- (11) Bučar, D. K.; Lancaster, R. W.; Bernstein, J. Disappearing Polymorphs Revisited. *Angew. Chemie - Int. Ed.* **2015**, *54* (24), 6972–6993.
- (12) Cruz-Cabeza, A. J.; Bernstein, J. Conformational Polymorphism. *Chem. Rev.* **2014**, *114* (4), 2170–2191.
- (13) Cruz-Cabeza, A. J.; Reutzler-Edens, S. M.; Bernstein, J. Facts and Fictions about Polymorphism. *Chemical Society Reviews*. The Royal Society of Chemistry November 16, 2015, pp 8619–8635.
- (14) Steed, J. W.; Turner, D. R.; Wallace, K. J. *Core Concepts in Supramolecular Chemistry and Nanochemistry*; John Wiley & Sons, Ltd: Chichester, 2007.
- (15) Groom, C. R.; Bruno, I. J.; Lightfoot, M. P.; Ward, S. C.; IUCr. The Cambridge Structural Database. *Acta Crystallogr. Sect. B Struct. Sci. Cryst. Eng. Mater.* **2016**, *72* (2), 171–179.
- (16) Simard, M.; Su, D.; Wuest, J. D. Use of Hydrogen Bonds to Control Molecular Aggregation. Self-Assembly of Three-Dimensional Networks with Large Chambers. *J. Am. Chem. Soc.* **1991**, *113* (12), 4696–4698.
- (17) Brunet, P.; Simard, M.; Wuest, J. D. Molecular Tectonics. Porous Hydrogen-Bonded Networks with Unprecedented Structural Integrity. *J. Am. Chem. Soc.* **1997**, *119* (11), 2737–2738.
- (18) Hosseini, M. W. Molecular Tectonics: From Simple Tectons to Complex Molecular Networks. *Acc. Chem. Res.* **2005**, *38* (4), 313–323.
- (19) Cavallo, G.; Metrangolo, P.; Milani, R.; Pilati, T.; Priimagi, A.; Resnati, G.; Terraneo, G. The Halogen Bond. *Chemical Reviews*. American Chemical Society February 24, 2016, pp 2478–2601.
- (20) Anslын, E. V.; Dougherty, D. A. *Modern Physical Organic Chemistry*; University Science, 2006.
- (21) Steed, J. W. First- and Second-Sphere Coordination Chemistry of Alkali Metal Crown Ether Complexes. *Coordination Chemistry Reviews*. Elsevier May 1, 2001, pp 171–221.

- (22) Jeffrey, G. A. *An Introduction to Hydrogen Bonding*; Oxford University Press, 1997.
- (23) Desiraju, G. R.; Shing Ho, P.; Kloo, L.; Legon, A. C.; Marquardt, R.; Metrangolo, P.; Politzer, P.; Resnati, G.; Rissanen, K. Definition of the Halogen Bond (IUPAC Recommendations 2013). *Pure Appl. Chem.* **2013**, *85* (8), 1711–1713.
- (24) Martinez, C. R.; Iverson, B. L. Rethinking the Term “Pi-Stacking.” *Chemical Science*. The Royal Society of Chemistry June 6, 2012, pp 2191–2201.
- (25) Hunter, C. A.; Lawson, K. R.; Perkins, J.; Urch, C. J. Aromatic Interactions. *Journal of the Chemical Society, Perkin Transactions 2*. The Royal Society of Chemistry January 1, 2001, pp 651–669.
- (26) Grimme, S. Do Special Noncovalent π - π Stacking Interactions Really Exist? *Angew. Chemie - Int. Ed.* **2008**, *47* (18), 3430–3434.
- (27) Kitaigorodskii, A. I. *Organic Chemical Crystallography*; Consultants Bureau: New York, 1961.

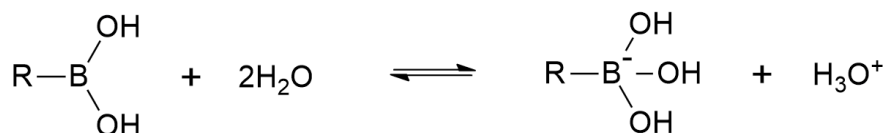
Chapter 2

Crystal Engineering of Boronic Acids

2.1 Overview

Boronic acids are boron-containing organic compounds that possess one C-B bond and two hydroxyls. The boron atom is trigonal planar, with sp^2 hybridisation and only six valence electrons, therefore having an empty p_z orbital perpendicular to the plane of the boronic acid. The B-C bond length lies approximately in the 1.55 – 1.59 Å range, so it's slightly longer and less energetic of a single C-C bond (323 *vs.* 358 kJ/mol). By contrast, the B-O bonds are shorter and stronger than typical C-O bonds (1.31 – 1.38 Å and 519 kJ/mol *vs.* 1.43 Å and 384 kJ/mol).¹ This is due to the conjugation between the oxygens lone pairs and the empty p_z orbital of the boron atom, that confers partial double bond character to those bonds.

The empty orbital plays a primary role in defining the peculiar chemistry of boronic acids. They are indeed Lewis acids since the B-atom can accept electron density from Lewis bases to form tetracoordinated adducts. Owing to this, trigonal boronic acids exist in water in equilibrium with the tetragonal boronate ions, as described in Scheme 2.1.1. In the tetragonal form, the B-O bond length increases to roughly 1.43 – 1.48 Å.



Scheme 2.1.1 Water equilibrium of boronic acids

This unique ability of the boronic acids to coordinate even mild electron donors is at the bottom of their revolutionary use in carbon-carbon coupling reactions.² Moreover, the formation of relatively stable tetracoordinate boronate complexes has proven useful for enzyme inhibition and a number of other medicinal applications,³⁻⁶ the clearance of the drug Velcade® for the treatment of multiple myeloma being the most notable example.⁷

Recently another peculiar feature of boronic acids has drawn a great deal of attention, namely the reversible condensation with diols to form boronic esters. This has been extensively studied for glucose and saccharides sensing,⁸ sensing of other diol-containing molecules, such as dopamine, and controlled drug release.⁹⁻¹¹

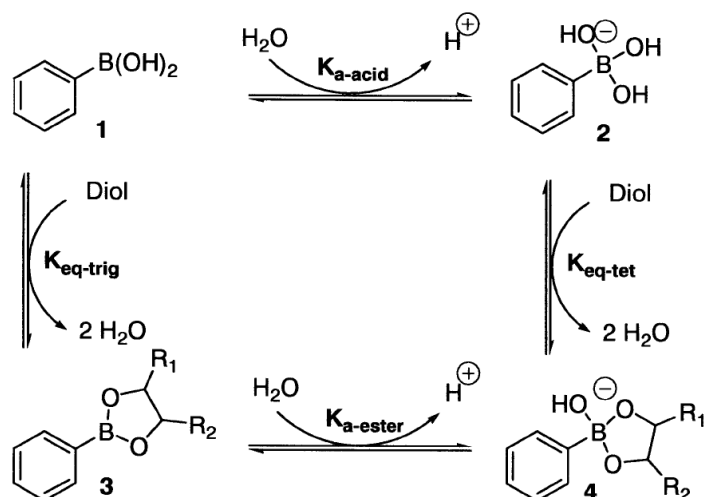
The rich chemistry of boronic acids, unsurprisingly, has found use also in supramolecular chemistry and crystal engineering. The formation of B-O bonds with diols, the coordination of electron-rich species, basic N-atoms above all, coupled with the hydrogen bonding capability of the hydroxyls groups have been exploited in the synthesis of a plethora of architectures, ranging from the porous Covalent Organic Frameworks (COFs), to supramolecular polymers, cycles, cages and gels just to name a few.¹²⁻¹⁵ Great interest is generated by the reversible character of such interactions and the possibility of combining them in an orthogonal manner:¹⁶ Ideally, the one-pot self-assembly of complex architectures can be achieved by “simple” programming of the assembly process through the design of the building blocks.

2.1.1 Interactions

Boronic acid – diol condensation

Boronic acids rapidly and reversibly interact with dicarboxylic acids, α -hydroxy carboxylic acids and diols to form boronate esters in aqueous media. Most commonly the interaction is with 1,2- and 1,3-diols to form, respectively, five- and six- membered covalently bonded cycles. The mechanism of the condensation is still not well understood, however in a simple schematisation it can be broken down to a thermodynamic cycle involving different equilibria for the trigonal neutral boronic acid (K_{trig}) and the tetragonal boronate anion (K_{tet}), as represented in Scheme 2.1.2.¹⁷

Previous knowledge had suggested that the condensation would be favoured in media with pH above the $\text{p}K_{\text{a}}$ of the boronic acid, *i.e.* involving the boronate ion as the reactive species, with $K_{\text{tet}} > K_{\text{trig}}$ by as much as 5 orders of magnitude.^{12,17} However, this assumption has been questioned, as examples were reported in which the trigonal boronic acid is more reactive;¹⁸⁻²⁰ in summary, boronic acid – diol complexation depends on a number of factors, including pH, $\text{p}K_{\text{a}}$ of both reagents, structure and the other unknown factors, so that it is difficult to draw general conclusions.



Scheme 2.1.2 The equilibria between phenylboronic acid and its diol ester (reproduced from ref. 17)

Since, regardless of the reaction mechanism, the condensation entails the loss of two equivalents of water, a convenient synthetic strategy for solids based on boronic esters is the removal of water through a dean stark trap. In this regard, solid-state synthetic methods offer another viable option, in that they circumvent the requirement to solubilise the reagents and control the pH of the medium.^{21,22}

B–N interaction

The B–N interaction, also termed dative or coordinative bond, is essentially a Lewis acid – Lewis base interaction, therefore “classical” electronic considerations on the effect of substituents apply: electron-withdrawing groups enhance the acidity of the boron atom, and electron-donating groups increase the basicity of the N-atom, thus strengthening the bond. The length of B–N bonds spans from 1.57 Å in the covalent boron nitride to more than 2 Å, that is close to the sum of the van der Waals radii;²³ according to the Cambridge Structural Database (CSD), the mean value for boronic acids is 1.650(55) Å.

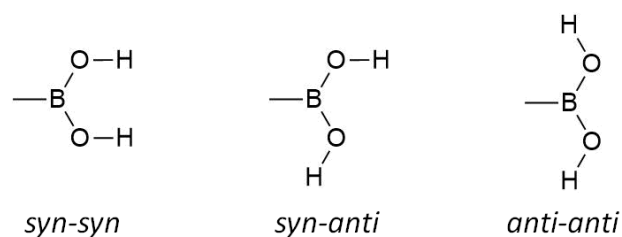
Energy values of the B–N interaction in boronic acids were derived experimentally and calculated in the range 12 – 25 kJ/mol;¹² from a crystal engineering perspective the strength of B–N bonds is comparable to that of a moderate hydrogen bond. The interaction is in a way directional: upon binding an N-atom the geometry of the boron atom changes from trigonal to

tetrahedral. Moreover, in the vast majority of cases, B–N bonds are formed jointly with boronic esters. A search in the CSD for structures containing the N-B(OH)₂R moiety returns just three hits: the reason is probably a kinetical advantage of H-bonds over B–N bonds.

H-bonds

The general features of H-bonds have already been discussed in paragraph 1.1.1, here just some specific features regarding boronic acids are introduced.

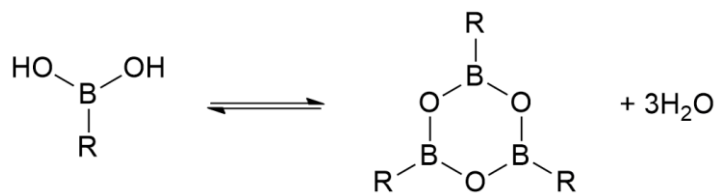
Boronic acids can adopt three conformations in H-bonding, namely the *syn,syn*, the *syn,anti* and the *anti,anti*-conformations, as depicted in Scheme 2.1.3. Energetically, the favoured conformation is the *syn,anti*;^{24,25} a frequent supramolecular motif is indeed the boronic acid dimer, structurally similar to the carboxylic acid and amide dimers, that adopts this conformation.



Scheme 2.1.3 H-bond conformations of boronic acids

Self-condensation

This can be regarded as a special case of boronic acid – diol condensation, as the -B(OH)₂ is, in fact, a geminal diol. Self-condensation of boronic acids yields six-membered B₃O₃ rings, dubbed boroxines (Scheme 2.1.4); the reaction is reversible, boroxines are susceptible of hydrolysis and are often in equilibrium with the reagents.¹



Scheme 2.1.4 Boroxine formation

The six-membered ring tends to planarity, however, coordination of electron-rich species, such as N-atoms, on the boron atoms cause a distortion of the ring. The structural rigidity and directionality of boroxine rings, coupled with the click-like attributes of their formation has been instrumental in the development of Covalent Organic Frameworks.^{26,27}

References

- (1) Hall, D. G. Structure, Properties, and Preparation of Boronic Acid Derivatives. In *Boronic Acids: Preparation and Applications in Organic Synthesis, Medicine and Materials, 1&2, Second Edition*; Wiley-VCH Verlag GmbH & Co. KGaA: Weinheim, Germany, 2011; pp 1–133.
- (2) Miyaoura, N.; Suzuki, A. Palladium-Catalyzed Cross-Coupling Reactions of Organoboron Compounds. *Chem. Rev.* **1995**, *95* (7), 2457–2483.
- (3) Yang, W.; Gao, X.; Wang, B. Boronic Acid Compounds as Potential Pharmaceutical Agents. *Med. Res. Rev.* **2003**, *23* (3), 346–368.
- (4) Trippier, P. C.; McGuigan, C. Boronic Acids in Medicinal Chemistry: Anticancer, Antibacterial and Antiviral Applications. *MedChemComm.* The Royal Society of Chemistry September 1, 2010, pp 183–198.
- (5) Baker, S. J.; Tomsho, J. W.; Benkovic, S. J. Boron-Containing Inhibitors of Synthetases. *Chemical Society Reviews.* The Royal Society of Chemistry July 14, 2011, pp 4279–4285.
- (6) Groll, M.; Berkers, C. R.; Ploegh, H. L.; Ovaa, H. Crystal Structure of the Boronic Acid-Based Proteasome Inhibitor Bortezomib in Complex with the Yeast 20S Proteasome. *Structure* **2006**, *14* (3), 451–456.
- (7) Velcade (bortezomib) Information | FDA <https://www.fda.gov/drugs/postmarket-drug-safety-information-patients-and-providers/velcade-bortezomib-information>.
- (8) Sun, X.; James, T. D. Glucose Sensing in Supramolecular Chemistry. *Chem. Rev.* **2015**, *115* (15), 8001–8037.
- (9) Nishiyabu, R.; Kubo, Y.; James, T. D.; Fossey, J. S. Boronic Acid Building Blocks: Tools for Sensing and Separation. *Chem. Commun.* **2011**, *47* (4), 1106.
- (10) Cambre, J. N.; Sumerlin, B. S. Biomedical Applications of Boronic Acid Polymers. *Polymer.* Elsevier September 29, 2011, pp 4631–4643.
- (11) Guan, Y.; Zhang, Y. Boronic Acid-Containing Hydrogels: Synthesis and Their Applications. *Chem. Soc. Rev.* **2013**, *42* (20), 8106–8121.
- (12) Fujita, N.; Shinkai, S.; James, T. D. Boronic Acids in Molecular Self-Assembly. *Chem. - An Asian J.* **2008**, *3* (7), 1076–1091.
- (13) Nishiyabu, R.; Kubo, Y.; James, T. D.; Fossey, J. S. Boronic Acid Building Blocks: Tools for Self Assembly. *Chem. Commun.* **2011**, *47* (4), 1124–1150.
- (14) Severin, K. Boronic Acids as Building Blocks for Molecular Nanostructures and Polymeric Materials. *Dalton Trans.* **2009**, *9226* (27), 5254–5264.
- (15) Luisier, N.; Bally, K.; Scopelliti, R.; Fadaei, F. T.; Schenk, K.; Pattison, P.; Solari, E.; Severin, K. Crystal Engineering of Polymeric Structures with Dative Boron–Nitrogen Bonds: Design Criteria and Limitations. *Cryst. Growth Des.* **2016**, *16* (11), 6600–6604.
- (16) Wong, C. H.; Zimmerman, S. C. Orthogonality in Organic, Polymer, and Supramolecular Chemistry: From Merrifield to Click Chemistry. *Chem. Commun.* **2013**, *49* (17), 1679–1695.
- (17) Springsteen, G.; Wang, B. A Detailed Examination of Boronic Acid-Diol Complexation. *Tetrahedron* **2002**, *58* (26), 5291–5300.
- (18) Yan, J.; Springsteen, G.; Deeter, S.; Wang, B. The Relationship among PKa, PH, and Binding Constants in the Interactions between Boronic Acids and Diols - It Is Not as Simple as It Appears. *Tetrahedron* **2004**, *60* (49), 11205–11209.

- (19) Miyamoto, C.; Suzuki, K.; Iwatsuki, S.; Inamo, M.; Takagi, H. D.; Ishihara, K. Kinetic Evidence for High Reactivity of 3-Nitrophenylboronic Acid Compared to Its Conjugate Boronate Ion in Reactions with Ethylene and Propylene Glycols. *Inorg. Chem.* **2008**, *47* (5), 1417–1419.
- (20) Tomsho, J. W.; Benkovic, S. J. Elucidation of the Mechanism of the Reaction between Phenylboronic Acid and a Model Diol, Alizarin Red S. *J. Org. Chem.* **2012**, *77* (5), 2098–2106.
- (21) Schnürch, M.; Holzweber, M.; Mihovilovic, M. D.; Stanetty, P. A Facile and Green Synthetic Route to Boronic Acid Esters Utilizing Mechanochemistry. *Green Chem.* **2007**, *9* (2), 139–145.
- (22) Pascu, M.; Ruggi, A.; Scopelliti, R.; Severin, K. Synthesis of Borasiloxane-Based Macrocycles by Multicomponent Condensation Reactions in Solution or in a Ball Mill. *Chem. Commun. (Camb)*. **2013**, *49* (1), 45–47.
- (23) Höpfl, H. The Tetrahedral Character of the Boron Atom Newly Defined - A Useful Tool to Evaluate the N → B Bond. *J. Organomet. Chem.* **1999**, *581* (1–2), 129–149.
- (24) Varughese, S.; Sinha, S. B.; Desiraju, G. R. Phenylboronic Acids in Crystal Engineering: Utility of the Energetically Unfavorable Syn,Syn-Conformation in Co-Crystal Design. *Sci. China Chem.* **2011**, *54* (12), 1909–1919.
- (25) Durka, K.; Jarzemska, K. N.; Kamiński, R.; Luliński, S.; Serwatowski, J.; Woźniak, K. Structural and Energetic Landscape of Fluorinated 1,4-Phenylenediboronic Acids. *Cryst. Growth Des.* **2012**, *12* (7), 3720–3734.
- (26) Korich, A. L.; Iovine, P. M. Boroxine Chemistry and Applications: A Perspective. *Dalton Transactions*. The Royal Society of Chemistry January 26, 2010, pp 1423–1431.
- (27) Ockwig, N. W.; Cote, A. P.; Keeffe, M. O.; Matzger, A. J.; Yaghi, O. M. Porous, Crystalline, Covalent Organic Frameworks. *Science (80-.)*. **2005**, *310* (November), 1166–1171.

2.2 Self-Assembly and Exfoliation of a Molecular Solid Based on Cooperative B–N and Hydrogen Bonds

Reproduced with permission from [Fornasari, L.; Mazzaro, R.; Boanini, E.; D'Agostino, S.; Bergamini, G.; Grepioni, F.; Braga, D. *Cryst. Growth Des.* **2018**, *18* (12), 7259–7263.] Copyright [2019] American Chemical Society.

<https://pubs.acs.org/doi/10.1021/acs.cgd.8b01674>

Two-dimensional (2D) materials are being intensively studied because of the unique properties that single-atom or few-atoms-thick materials exhibit compared to their bulk counterparts. The most extensively studied 2D material is graphene.¹ However, a class of 2D materials beyond graphene is rapidly emerging, comprising a wide choice of organic, inorganic, and hybrid materials.^{2,3} The top-down exfoliation strategy has been generally regarded as a suitable approach in the preparation of nanosheets from inorganic van der Waals solids,^{4,5} whereas a supramolecular approach based on weak interactions has been employed in the bottom-up self-assembly of 2D materials either from solution or on a surface.^{6,7} The boron–nitrogen interaction has recently gained attention in supramolecular chemistry as a promising tool for the design and realization of a variety of functional materials. Boronic esters, obtained from the condensation of alkyl or aryl boronic acids with diols/alcohols, are Lewis acidic sites that readily interact with a basic N atom. Both B–O and B–N bonds possess dynamic character, thus allowing easily accessible self assembly of supramolecular architectures.^{8–10} B–N bonds have been successfully used as a structure-directing agent in the preparation of organogels,¹¹ soft and crystalline supramolecular polymers,^{12,13} nanoparticles,¹⁴ clathrates,¹⁵ cages,^{16,17} tweezer-type inclusion complexes,¹⁸ macrocycles,^{12,19,20} and 2D and 3D networks.^{11,21} A major drawback in structure design by B–N bonds, though, is that esterification of the corresponding boronic acid is usually required in order for the bond to be effective. Severin et al. in 2012¹³ suggested that complex architectures should in principle be obtained by combining B–N bonds with supramolecular interactions such as hydrogen bonds via orthogonal self-assembly. To date, however, no results have been published describing this approach, and the structure of only one molecule containing both a B–N bond and a $-B(OH)_2$ moiety is known as the serendipitous result (dating 2005) of a crystal engineering strategy “gone awry”.²² In our continuous quest for new building blocks to be used in the design, construction, and exploitation of crystalline materials, i.e., within the

framework of crystal engineering as the science of “making crystals with a purpose”,²³ and on the basis of our past experience²⁴ with systems containing both the boronic acid and the pyridine groups, we decided to explore the possibility of combining the two moieties into an all-organic framework, using the B(OH)₂ group both as an acceptor of electron density from the N atom and as a hydrogen bonding donor/acceptor.

To this end, we have selected two compounds, namely, the 4-pyridinylboronic acid (**1**) and the 4-(pyridin-4-yl)-phenylboronic acid (**2**). The crystal structures of **1** and **2** have been determined from single crystal and powder X-ray diffraction (XRD) data, respectively, and their crystal packing features were studied in detail. Interestingly, we found that upon crystallization **1** self-assemble into tetramers via B–N bonds. The tetramers, in turn, are linked by hydrogen bonds. As a matter of fact B–N and OH···O bonds effectively cooperate in the formation of a layered solid which can be easily exfoliated as it will be demonstrated in the following. Intralayer interactions have been assessed to be more than twice as strong as interlayer ones; the solid could be successfully separated in molecular nanosheets by means of sonication-assisted liquid-phase exfoliation (LPE). In contrast, the crystal packing of the structurally related compound **2** is based on the well-recognized hydrogen bonding interaction between B–OH and N(pyridine), B–OH···N(py) hydrogen bonding pattern²⁵ and does not show any anisotropy with respect to interaction energies.

Compound **1** is scarcely soluble in all the common laboratory solvents (except for alcohols, with which **1** reacts forming the corresponding boronic esters), and good quality single crystals for structural characterization could only be grown from a mixture of H₂O and DMSO under reflux (see Supporting Information for experimental details). A macrocyclic tetramer forms through B–N bonds which further assemble into 2D layers through hydrogen bonds involving the acidic groups and orthogonal to the B–N bonds (Figure 2.2.1).

The macrocycle has a squared shape with an internal width of 6.5 Å, with a cavity volume potentially able to contain a small molecule like water; the 2-D layers, however, are stacked in an ABAB sequence (Figure 2.2.1, bottom), thus preventing the formation of open channels. The boron atoms adopt a distorted tetrahedral geometry, with B–N bonds distances [1.661(6) and 1.669(6) Å]. The boronic acid OH groups (*syn,syn* conformation) act both as hydrogen bond donors and acceptors, forming the cube-like motif evidenced in Figure 2.2.1 (O···O distances in the range 1.99(4)–2.04(4) Å, see Table SI-2). Each

macrocycle contains a cavity that accounts for ca. 9% of the unit cell.²⁶ Given that B–N bonds and hydrogen bonds involving the boronic acid OH groups are comparable in energy, and that boronic B–N complexes have often found to be slightly higher in energy than the corresponding H-bonded complexes,^{27,28} one can assume that B–N and hydrogen bonds in crystalline **1** act in a truly cooperative rather than competing fashion.

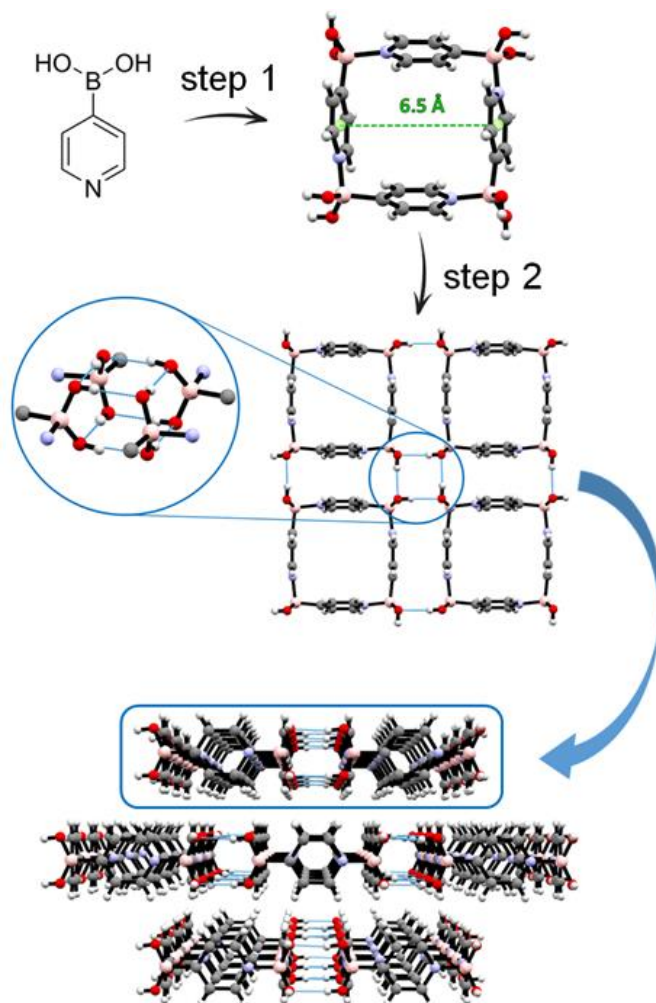


Figure 2.2.1 Hierarchical self-assembly of **1** from the single-component to the tetramer (step 1) and the 2D layers (step 2); a detail of the H-bonding motif is represented in the blue circle.

Crystal packing features of the closely related compound 4-(pyridine-4-yl)phenylboronic acid (**2**), whose solid-state structure was determined from XRD data (see Supporting Information for experimental details and Figure SI-2 for difference pattern), were also investigated. No B–N bonds, however, are

present in crystalline **2**; although the pyridyl moiety ought to be a better electron donor with respect to the one in **1**, the bonding motif observed in **1** is not replicated here. The boronic acid groups in **2** are in *syn,anti* conformation, forming an O–H···O hydrogen bonded chain [O···O 2.91(4) Å] with the neighboring molecules, at the same time O–H···N bonds are established involving the pyridinic substituent [O···N 2.888(2) Å], see Figure 2.2.2a and Table SI-2.

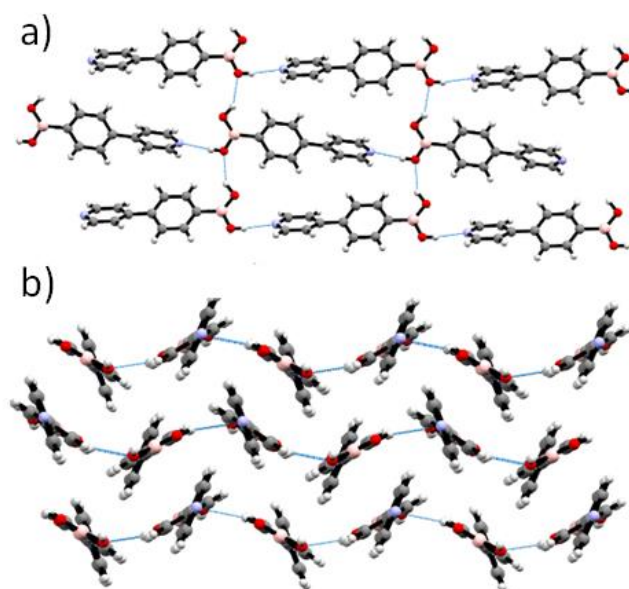


Figure 2.2.2 Hydrogen bonding motif in **2** (a) and perspective view of the zigzag sheets formed in the structure of **2** (b).

As a result, a zigzag sheet, comprising the two different H-bonds in orthogonal directions, is formed (Figure 2.2.2b). The driving force in the absence of B–N bonds might lie in the principle *natura abhorret a vacuo*: if the same square motif was to be maintained also in the case of **2**, much larger voids would then be generated.

Hirshfeld surface and intermolecular interaction energy (IIE)^{29,30} analyses were performed using the CrystalExplorer software package.³¹ For crystalline **1** IIEs calculations confirm that the strongest interactions involve the first neighbors within the plane, with a total energy of -126.3 and -129.7 $\text{kJ}\cdot\text{mol}^{-1}$, versus an energy of -54.4 and -51.8 $\text{kJ}\cdot\text{mol}^{-1}$ for the interactions with the first out-of-plane neighbors (see Supporting Information). As expected, given the electrostatic nature of the hydrogen bond, the in-plane contacts are in turn dominated by the electrostatic component of the total energy, while in the case

of interplanar interactions the dispersive term is the strongest (Table SI-3). In the case of **2** the strongest intermolecular interactions correspond to the OH \cdots Py bonds within the zigzag sheet and a stacking interaction with the adjacent sheets (Table SI-4). Overall the interaction energies assessed by IIEs calculations are comparable, with the total energies ranging from $-14\text{ kJ}\cdot\text{mol}^{-1}$ to $-28\text{ kJ}\cdot\text{mol}^{-1}$. Therefore, we turned our attention to the study of morphology and exfoliation properties of crystalline **1**.

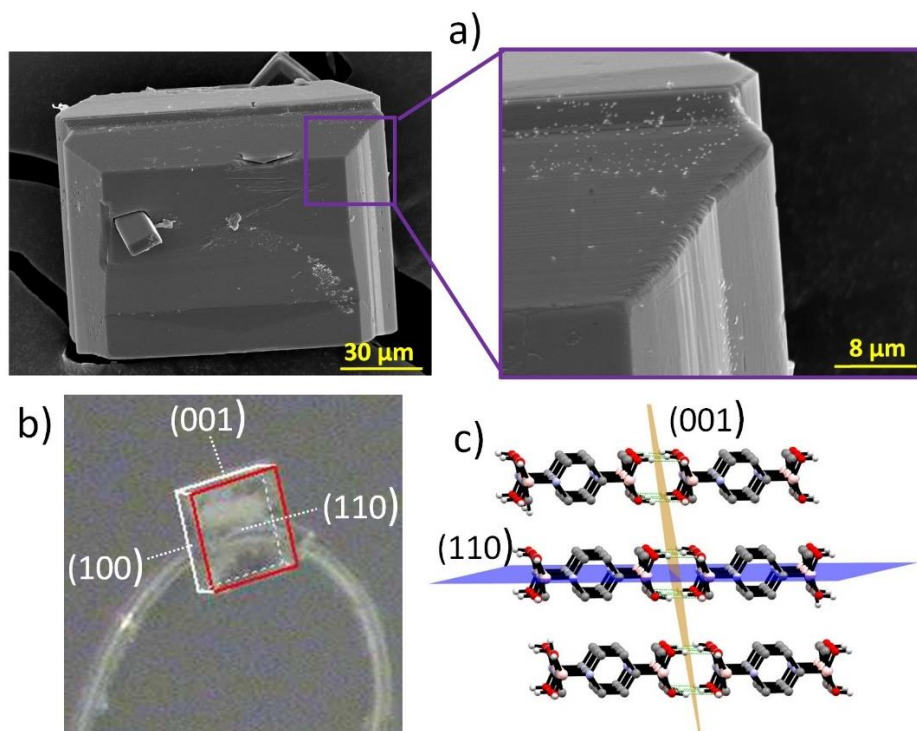


Figure 2.2.3 (a) SEM micrographs of a single crystal of **1**, (b) face indexing of the same crystal, and (c) crystal packing showing the (110) Miller plane, parallel to the face evidenced in red in (b) and the (001) Miller plane orthogonal to the former.

Scanning electron microscopy (SEM) images (Figure 2.2.3a) show single crystals of **1** with extremely regular shapes and presenting a broad and smooth face characterized by angles at 90° and mean dimensions of $150\ \mu\text{m} \times 110\ \mu\text{m}$. Along the directions orthogonal to this flat surface, the crystals clearly display a compact step-and-terrace morphology. These features are clearly visible also in polycrystalline samples of **1** (Figure SI-4). Crystal face indexing (Figure 2.2.3b) and powder XRD recorded on the same specimen lying flat on a quartz slide (Figure SI-4) confirm that the largest face (in Figure 2.2.3a) corresponds to the (110) plane (Figure 2.2.3c), which contains the 2D assembly held together by orthogonal B–N and O–H \cdots H interactions.

Exfoliation of **1** was thus attempted by ultrasonication of single crystals in the solvents dichloromethane and acetone (see Supporting Information for experimental details). In all cases, transmission electron microscopy (TEM) analysis revealed thin nanosheets, with different morphologies depending on the type of solvent used in the sonication process (see Figure 2.2.4). Square-like nanosheets from dichloromethane (**1-S**) most probably derive from the broad and smooth face characterized by angles at 90° previously observed with SEM (Figure 2.2.3a), and hexagon-like from acetone (**1-H**), likely due to the cleavage of planes orthogonal to the former. Chemical identity of the exfoliated materials was verified by comparing the FTIR spectra recorded after sonication (Figure SI-12), which are fully consistent with that recorded on the bulk polycrystalline sample. This observation suggests that the solvent not only acts as a “medium” for the propagation of the waves, but also plays an active role in determining the final morphology. A similar effect of the solvent in liquid phase exfoliation has been previously reported in the literature.^{32,33}

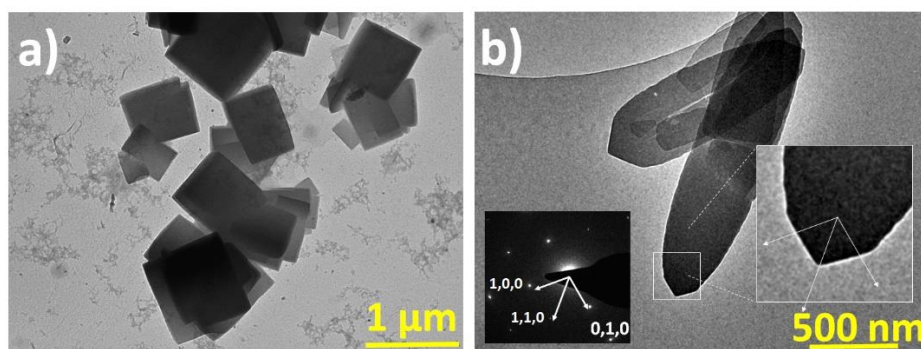


Figure 2.2.4 TEM images for the exfoliation of **1** as obtained by liquid-assisted sonication in (a) dichloromethane, and (b) acetone; the inset shows the corresponding SAED pattern.

To get more insights, we performed also selected area electron diffraction (SAED) measurements (see Supporting Information for details). However, the exfoliated sheets **1-S** were very sensitive to the electron beam and rapidly degraded during analysis (<8 s). Only the **1-H** sheets withstood enough under the beam and provided a clear diffraction pattern which agrees well with the $\langle 001 \rangle$ zone axis (Figure 2.2.4b and Figure SI-13). This key experiment proves that both the materials maintain crystalline order and that the hexagon-like morphology results from the cleavage of the (001) Miller plane (depicted in orange in Figure 2.2.3c). Atomic force microscopy (AFM) imaging revealed the presence of flat nanosheets in each case (Figure 2.2.5). Furthermore, the

height profile diagrams show that the thickness of the sheets lies in the range of ca. 50–60 nm and 20–30 nm, for **1** exfoliated from dichloromethane and acetone, respectively (Figures 2.2.5 and SI-14). Combining this information with the one provided by SAED measurements and the crystal structure, the thickness of the **1**-H sheets can be assessed at roughly 2–3 layers, while, assuming that the exfoliation plane in **1**-S is the (110) Miller plane, the thickness would be consistent with 8–10 layers.

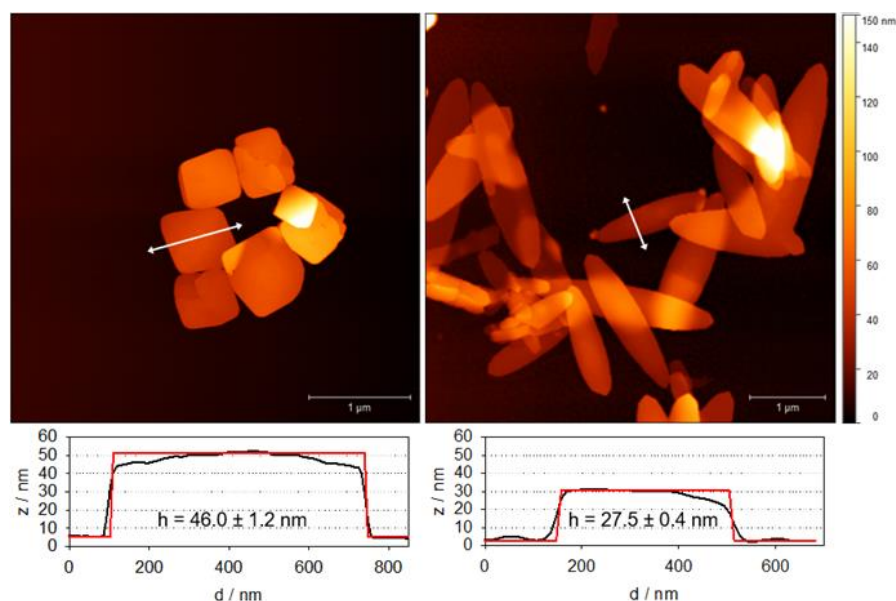


Figure 2.2.5 AFM images and corresponding height profiles for the exfoliation products **1**-S (left) and **1**-H (right).

2.2.1 Conclusions

In this paper we have reported that 4-pyridinylboronic acid (**1**) self-assembles in the solid state by forming supramolecular tetrameric units held together by B–N bonds and interacting in the crystal structure via O–H···O hydrogen bonds. This particular pattern generates a markedly anisotropic behavior that renders **1** a layered 2D material than can be exfoliated. We have found that in crystalline **1** B–N and hydrogen bonds cooperate to the stabilization of 2D layers, while only weak C–H···O hydrogen bonds and dispersion forces are at work between layers. The structure of the related 4-(pyridine-4-yl)phenylboronic acid (**2**) does not show analogous behavior featuring typical B–OH···N(Py) hydrogen bonds.

Liquid-phase sonication was successfully applied to preparation of stable dispersions and, as proved by TEM and AFM imaging, single crystals of **1** can be effectively exfoliated into thinner sheets with smooth surfaces. FTIR spectra of the so-obtained materials were fully consistent with that recorded on the bulk sample, indicating thus that chemical identity was preserved. Interestingly, the choice of the solvent used during liquid-phase sonication played a crucial role in the determination of the final morphology of the exfoliated materials, namely, square-like (**1-S**) and hexagon-like (**1-H**) sheets. On the basis of considerations on crystals morphology observed with SEM and SAED measurements, we can assert that **1-S** and **1-H** derive from the cleavage of Miller planes orthogonal among them, namely, the (110) and the (001). To the best of these authors' knowledge, **1** represents the first example of a material assembled via cooperative B–N and O–H···O bonds.

References

- (1) Novoselov, K. S.; Falko, V. I.; Colombo, L.; Gellert, P. R.; Schwab, M. G.; Kim, K. A roadmap for graphene. *Nature* **2012**, 490, 192–200.
- (2) Bhimanapati, G. R.; Lin, Z.; Meunier, V.; Jung, Y.; Cha, J.; Das, S.; Xiao, D.; Son, Y.; Strano, M. S.; Cooper, V. R.; et al. Recent Advances in Two-Dimensional Materials beyond Graphene. *ACS Nano* **2015**, 9, 11509–11539.
- (3) Boott, C. E.; Nazemi, A.; Manners, I. Synthetic Covalent and Non-Covalent 2D Materials. *Angew. Chem., Int. Ed.* **2015**, 54, 13876–13894.
- (4) Ciesielski, A.; Samori, P. Graphene via sonication assisted liquidphase exfoliation. *Chem. Soc. Rev.* **2014**, 43, 381–398.
- (5) Chhowalla, M.; Shin, H. S.; Eda, G.; Li, L. J.; Loh, K. P.; Zhang, H. The chemistry of two-dimensional layered transition metal dichalcogenide nanosheets. *Nat. Chem.* **2013**, 5, 263–275.
- (6) Zhang, K. Da; Tian, J.; Hanifi, D.; Zhang, Y.; Sue, A. C. H.; Zhou, T. Y.; Zhang, L.; Zhao, X.; Liu, Y.; Li, Z. T. Toward a singlelayer two-dimensional honeycomb supramolecular organic framework in water. *J. Am. Chem. Soc.* **2013**, 135, 17913–17918.
- (7) Blunt, M. O.; Russell, J. C.; Gimenez-Lopez, M. d. C.; Garrahan, J. P.; Lin, X.; Schroder, M.; Champness, N. R.; Beton, P. H. Random Tiling and Topological Defects in a Two-Dimensional Molecular Network. *Science* (Washington, DC, U. S.) **2008**, 322, 1077–1081.
- (8) Nishiyabu, R.; Kubo, Y.; James, T. D.; Fossey, J. S. Boronic acid building blocks: tools for self assembly. *Chem. Commun.* **2011**, 47, 1124–1150.
- (9) Severin, K. Boronic acids as building blocks for molecular nanostructures and polymeric materials. *Dalton Trans* **2009**, 9226, 5254–5264.
- (10) Luisier, N.; Bally, K.; Scopelliti, R.; Fadaei, F. T.; Schenk, K.; Pattison, P.; Solari, E.; Severin, K. Crystal Engineering of Polymeric Structures with Dative Boron-Nitrogen Bonds: Design Criteria and Limitations. *Cryst. Growth Des.* **2016**, 16, 6600–6604.
- (11) Sheepwash, E.; Krampl, V.; Scopelliti, R.; Sereda, O.; Neels, A.; Severin, K. Molecular networks based on dative boron-nitrogen bonds. *Angew. Chem., Int. Ed.* **2011**, 50, 3034–3037.
- (12) Salazar-Mendoza, D.; Cruz-Huerta, J.; Höpfl, H.; Hernandez-Ahuactzi, I. F.; Sanchez, M. Macrocycles and coordination polymers derived from self-complementary tectons based on N-containing boronic acids. *Cryst. Growth Des.* **2013**, 13, 2441–2454.

- (13) Sheepwash, E.; Luisier, N.; Krause, M. R.; Noe, S.; Kubik, S.; Severin, K. Supramolecular polymers based on dative boron–nitrogen bonds. *Chem. Commun.* **2012**, 48, 7808.
- (14) Li, L.; Yuan, C.; Dai, L.; Thayumanavan, S. Thermoresponsive polymeric nanoparticles: Nucleation from cooperative polymerization driven by dative bonds. *Macromolecules* **2014**, 47, 5869–5876.
- (15) Herrera-España, A. D.; Campillo-Alvarado, G.; Roman-Bravo, P.; Herrera-Ruiz, D.; Höpfl, H.; Morales-Rojas, H. Selective isolation of polycyclic aromatic hydrocarbons by self-assembly of a tunable N→B clathrate. *Cryst. Growth Des.* **2015**, 15, 1572–1576.
- (16) Icli, B.; Sheepwash, E.; Riis-Johannessen, T.; Schenk, K.; Filinchuk, Y.; Scopelliti, R.; Severin, K. Dative boron–nitrogen bonds in structural supramolecular chemistry: multicomponent assembly of prismatic organic cages. *Chem. Sci.* **2011**, 2, 1719.
- (17) Dhara, A.; Beuerle, F. Reversible Assembly of a Supramolecular Cage Linked by Boron-Nitrogen Dative Bonds. *Chem. - Eur. J.* **2015**, 21, 17391–17396.
- (18) Campillo-Alvarado, G.; Vargas-Olvera, E. C.; Höpfl, H.; Herrera-España, A. D.; Sanchez-Guadarrama, O.; Morales-Rojas, H.; MacGillivray, L. R.; Rodríguez-Molina, B.; Farfan, N. Self-Assembly of Fluorinated Boronic Esters and 4,4'-Bipyridine into 2:1 N→B Adducts and Inclusion of Aromatic Guest Molecules in the Solid State: Application for the Separation of o, m, p -Xylene. *Cryst. Growth Des.* **2018**, 18, 2726–2743.
- (19) Christinat, N.; Scopelliti, R.; Severin, K. A new method for the synthesis of boronate macrocycles. *Chem. Commun.* **2004**, 103, 1158–1159.
- (20) Icli, B.; Solari, E.; Kilbas, B.; Scopelliti, R.; Severin, K. Multicomponent Assembly of Macrocycles and Polymers by Coordination of Pyridyl Ligands to 1,4-Bis(benzodioxaborole)-benzene. *Chem. - Eur. J.* **2012**, 18, 14867–14874.
- (21) Cruz-Huerta, J.; Salazar-Mendoza, D.; Hernandez-Paredes, J.; Hernandez Ahuactzi, I. F.; Höpfl, H. N-containing boronic esters as self-complementary building blocks for the assembly of 2D and 3D molecular networks. *Chem. Commun.* **2012**, 48, 4241.
- (22) Aakeröy, C. B.; Desper, J.; Levin, B. Crystal engineering gone awry and the emergence of the boronic acid–carboxylate synthon. *CrystEngComm* **2005**, 7, 102–107.
- (23) Braga, D.; Grepioni, F.; Maini, L.; D'Agostino, S. Making crystals with a purpose; a journey in crystal engineering at the University of Bologna. *IUCrJ* **2017**, 4, 369–379.
- (24) Braga, D.; Polito, M.; Braccacini, M.; D'Addario, D.; Tagliavini, E.; Sturba, L.; Grepioni, F. Novel organometallic building blocks for molecular crystal engineering. *Organometallics* **2003**, 22, 2142–2150.
- (25) Pedireddi, V. R.; SeethaLekshmi, N. Boronic acids in the design and synthesis of supramolecular assemblies. *Tetrahedron Lett.* **2004**, 45, 1903–1906.
- (26) Spek, A. L. Structure validation in chemical crystallography. *Acta Crystallogr., Sect. D: Biol. Crystallogr.* **2009**, 65, 148–155.
- (27) Larkin, J. D.; Fossey, J. S.; James, T. D.; Brooks, B. R.; Bock, C. W. A computational investigation of the nitrogen-boron interaction in o-(N,N-dialkylaminomethyl)arylboronate systems. *J. Phys. Chem. A* **2010**, 114, 12531–12539.
- (28) Zhu, L.; Shabbir, S. H.; Gray, M.; Lynch, V. M.; Sorey, S.; Anslyn, E. V. A structural investigation of the N-B interaction in an o-(N,N-dialkylaminomethyl)arylboronate system. *J. Am. Chem. Soc.* **2006**, 128, 1222–1232.
- (29) Spackman, M. A.; Jayatilaka, D. Hirshfeld surface analysis. *CrystEngComm* **2009**, 11, 19–32.
- (30) Mackenzie, C. F.; Spackman, P. R.; Jayatilaka, D.; Spackman, M. A. CrystalExplorer model energies and energy frameworks: extension to metal coordination compounds, organic salts, solvates and open-shell systems. *IUCrJ* **2017**, 4, 575–587.
- (31) Turner, M. J.; McKinnon, J. J.; Wolff, S. K.; Grimwood, D. J.; Spackman, P. R.; Jayatilaka, D.; Spackman, M. A. *CrystalExplorer17*; University of Western Australia, **2017**.
- (32) Zhang, N.; Wang, T.; Wu, X.; Jiang, C.; Chen, F.; Bai, W.; Bai, R. Self-exfoliation of 2D covalent organic frameworks: morphology transformation induced by solvent polarity. *RSC Adv.* **2018**, 8, 3803–3808.
- (33) Nguyen, E. P.; Carey, B. J.; Daeneke, T.; Ou, J. Z.; Latham, K.; Zhuiykov, S.; Kalantar-Zadeh, K. Investigation of two-solvent grinding-assisted liquid phase exfoliation of layered MoS₂. *Chem. Mater.* **2015**, 27, 53–59.

2.3 Zwitterionic Systems Obtained by Condensation of Heteroaryl-Boronic Acids and Rhodizonic Acid

Reproduced with permission from [Fornasari, L.; D'Agostino, S.; Braga, D. Zwitterionic Systems Obtained by Condensation of Heteroaryl-Boronic Acids and Rhodizonic Acid. *European J. Org. Chem.* **2019**, 2019 (7), 1574–1582.] Copyright [2019] John Wiley and Sons.

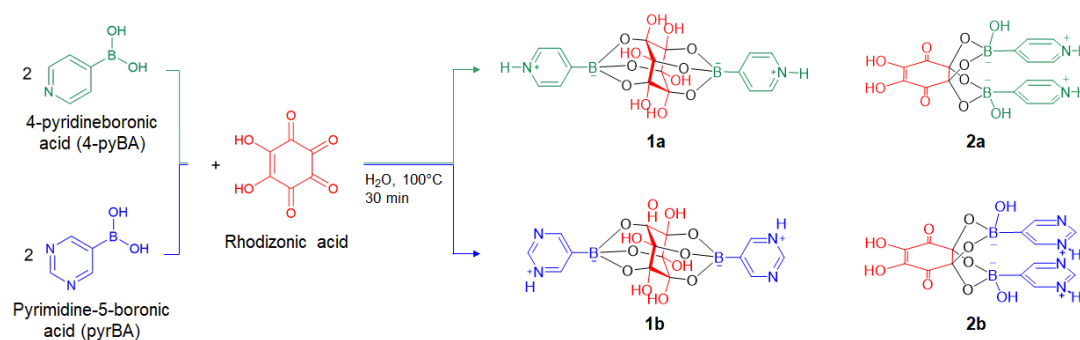
<https://rdcu.be/bVv2r>

2.3.1 Introduction

Boronic acids have been extensively studied for their use as reagents in Suzuki–Miyaura coupling reactions^{1,2} and for their biological activity, for example as protease and arginase inhibitors or as antibacterial agents.³⁻⁵ Furthermore, boronic acids are known to reversibly bind diols and alcohols; such dynamic covalent reactivity has prompted their use as receptors in saccharides sensing,⁶⁻⁹ organocatalysis,¹⁰ as well as building blocks for the synthesis of covalent organic frameworks (COFs), gels and self-healing polymers to name a few.¹¹⁻¹³ The very mechanism of the boronic acid-diol condensation is still being explored. The trigonal $-B(OH)_2$ and the tetragonal $-B(OH)_3^-$ species are in fast equilibrium and both undergo condensation with different kinetic constants, depending on the reaction conditions and on the nature of the reagents, thus potentially allowing fine tuning of the outcome.¹⁴⁻¹⁶ Other notable features of boronic acids are the coordination of Lewis basic species through the empty p_z orbital of the boron atom and their ability to act as both hydrogen-bond donors and acceptors, that found applications in sensing, crystal engineering and assembly of supramolecular 2D and 3D architectures.^{11,12,17-20}

The second compound of interest for this work is the six-membered ring oxocarbon rhodizonic acid. Despite being known for almost two centuries, oxocarbon acids continue to spark the interest of researchers due to their unique chemistry.²¹⁻²⁴ For example, lithium and sodium rhodizonate have been studied for the production of all-organic rechargeable batteries,²⁵⁻²⁷ while sodium rhodizonate is widely employed in the detection of lead and barium in gunpowder residue and seeds.^{28,29} Proton transfer and ferroelectric properties have been studied of single layers of rhodizonic acid assembled on noble metal surfaces.^{30,31}

In this paper, we report the results of our study of the condensation reactions of rhodizonic acid and boronic acid derivatives aimed to prepare new building blocks for crystal engineering studies.³² This is also in keeping with our investigation of the supramolecular assembly and solid-state properties of 4-pyridinylboronic and of 4-(pyridine-4-yl)phenylboronic acid.³³ The initial purpose was the exploration of the possibility of obtaining multi-component crystals with boronic acid derivatives and rhodizonic acid as parent compounds, also in view of the well-established stability and versatility in the formation of heterodimers of the kind boronic acid/carboxylic acid and boronic acid/carboxylate.^{34,35} Unexpectedly, however, the co-crystallization attempts rather than yielding co-crystals opened the door to the preparation of four novel building blocks obtained through a condensation reaction between rhodizonic acid and 4-pyridinylboronic acid (4-pyBA) and pyrimidine-5-boronic acid (pyrBA) acid, respectively. See Scheme 2.3.1.



Scheme 2.3.1 Schematic representation of the products **1a**, **1b**, **2a**, **2b** obtained by reaction of 4-pyridinylboronic acid (4-pyBA) and pyrimidine-5-boronic acid (pyrBA) with rhodizonic acid.

Investigation of this reactivity led us to discover that the different products could be obtained selectively by varying the experimental conditions as it will be discussed in the following. The thermal stability of the four compounds has also been studied, evidencing a single-crystal to single-crystal dehydration process. Besides their potential use as novel building blocks in crystal engineering in view of their zwitterionic nature (*vide infra*) and the possibility of forming hydrogen bonding networks,³⁶⁻³⁸ insight into their formation and stability might prove broadly useful in organic and organoboron chemistry and catalysis.³⁹

2.3.2 Results and Discussion

Synthesis of 1a, 1b, 2a, 2b

4-Pyridineboronic acid (4-pyBA) and pyrimidine-5-boronic acid (5-pyrBA) were reacted in hot water with rhodizonic acid dihydrate to obtain the four species **1a**, **2a**, **1b**, and **2b** (Scheme 2.2.1). The compounds are the product of a condensation reaction involving boronic acid and the diol functions contained in rhodizonic acid dihydrate. 4-pyBA and pyrBA showed similar reactivity, giving rise to analogous molecules.

All products crystallize as hydrates with a different number of water molecules (see below). A typical reaction consisted of heating a suspension of the insoluble boronic acid in an aqueous solution of rhodizonic acid until complete dissolution was achieved. Upon cooling of the solution to room temperature **1a**·2H₂O and **2a**·3H₂O (or **1b**·2.5H₂O and **2b**·3H₂O if pyrimidine-5-boronic acid was employed) concurrently crystallized, with a strong predominance of **2a**·3H₂O over **1a**·2H₂O (Figure 2.3.1). If the cooling rate was slowed down (see experimental section) the ratio between the two species was reversed: **1a**·2H₂O crystallized preferably, along with a small amount of **2a**·3H₂O and of an amorphous phase.

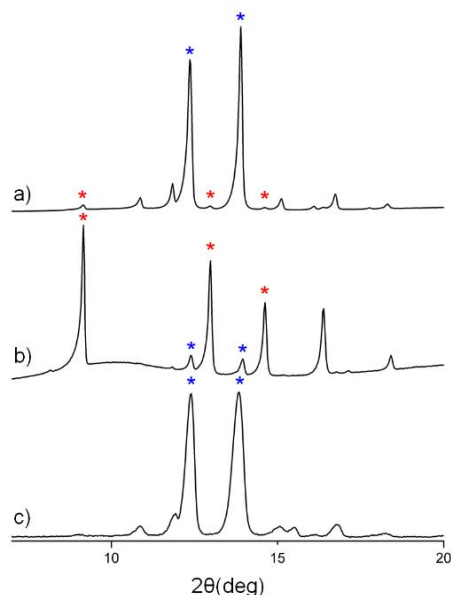


Figure 2.3.1 XRPD patterns ($2\theta = 7^\circ\text{-}20^\circ$) of the bulk products of the reaction of 4-pyBA with rhodizonic acid using: a) normal cooling conditions, b) slow cooling conditions and c) synthesis by kneading; blue asterisks denote diagnostic peaks of the species **2a**·3H₂O and red asterisks denote diagnostic peaks of the species **1a**·2H₂O. In the pattern b) it is possible to see the diffuse scattering produced by the amorphous fraction centered at $2\theta = 10^\circ$.

The ratio of the two compounds was evaluated for both the former and latter (slow cooling) procedure through a Rietveld refinement performed on the XRPD pattern of the bulk samples. It was found that in the case of normal cooling **1a**·2H₂O constitutes about 2 % of the bulk while applying the slow cooling procedure **1a**·2H₂O represents about 75 % of the crystalline product, though we were not able to assess a total yield, given the impossibility of separating the crystalline phases from the amorphous product. Nevertheless, **2a**·3H₂O and **2b**·3H₂O could be obtained in a quantitative amount also by kneading of the solid reagents with few drops of water, suggesting that these species might be metastable products afforded by kinetic limitations.

Since in **1a** and **1b** the enediol group of rhodizonic acid is oxidized and hydrated to yield a dodecahydroxycyclohexane-like moiety, it is safe to assume that some kind of equilibrium is present in the solution that involves rhodizonic acid. As it was reported by Gelb et al.⁴⁰ rhodizonic acid is stable in water at room temperature in its ortho-dihydrate form, and only after a long time (> 50 hours) starts to isomerize to a para-dihydrate form. A solution of rhodizonic acid was thus heated at reflux for 1–2 hours before reacting it with the boronic acid, in order to explore the possibility that the oxidation of rhodizonic acid was due to the temperature; the results, though, were identical to the previous syntheses. Similarly, reacting rhodizonic acid and boronic acid for longer times led to no significant differences, thus suggesting the presence of a fast redox equilibrium of aqueous rhodizonic acid dihydrate, possibly promoted by the heteroaromatic-substituted boronic acid.

Interestingly, in **2a** and **2b** boronic acid is condensed on the germinal diols site of the o-dihydrate form rather than on the enediol function. Different stoichiometric ratios were also tested (BA/RA 1:1 and 3:1), yielding invariably the four species **1a**, **2a** and **1b**, **2b**; therefore, it appears that the enediols are almost non-reactive compared to the germinal diols sites which, on the other hand, are fully complexed by boronic acid even when the latter is in defect amount. It has been observed that the binding of mono-deprotonated diols is significantly faster than their neutral counterparts, with the highest rate between the pK_a of the diol and the pK_a of the boronic acid, the reason being attributed to the enhanced nucleophilicity of the oxyanion that favorably attacks the Lewis acidic boron site.^{16, 41} Such observation apparently contrasts with the behavior of rhodizonic acid in which the most acidic diol, the enediol, does not show any binding to the boronic acid in the solid. This could be

related to the steric hindrance of the boronic ester formed in **2a** and **2b**: if the rate of hydrolysis is sufficiently low, it is possible that the products precipitate out shifting the equilibrium due to Le Châtelier's principle.

It is also noteworthy that both **1a** and **2a** contain the sp^3 boronate ion, which upon protonation of the pyridine N-terminus, gives the compounds their zwitterionic character. In the case of **1a** (and **1b**) the tetrahedral geometry of the boronate ion is convenient for the condensation with the dodecahydroxycyclohexane moiety, while in the case of **2a** (and **2b**) the transition from sp^2 to sp^3 is achieved through a solvent insertion, a frequent case in protic solvents that is promoted by the binding of a diol;⁴² the product of the solvent insertion in the present case is then further stabilized by the pyridinyl substituent, that can be protonated to balance the overall charge. Structures of tridentate organoboronate esters similarly to **1a**·2H₂O and **1b**·2.5H₂O were reported in the last decade,⁴³⁻⁴⁵ but in those cases the compounds were produced through the condensation of a boronic acid with a preformed reactant, like a triol or hexaol, while in the present case the other component is generated in situ from the oxocarbon acid.

The same synthesis was performed with sodium rhodizonate and 4-pyBA to see how the rhodizonate dianion would behave towards boronic acid. A new crystal phase, **1a**·4H₂O, was produced in this case, that is, in fact, the same zwitterionic boronate ester **1a**, only in a structure with a different hydration stoichiometry. It is thus possible that the formation of the “axle” species **1a** and **1b** involves the equilibrium between rhodizonic acid dihydrate and the anhydrous rhodizonate dianion.

The reaction between 4-pyBA and sodium rhodizonate yielded **1a** only when a stoichiometry 1:1 was employed, with the excess sodium rhodizonate undergoing decomposition to $C_5O_5^{2-}(Na^+)_2(H_2O)_2$ (and small quantity of other unassigned by-products, as determined by XRD analyses on the bulk product after desiccation; see Figure S7). Aqueous solutions of the rhodizonate dianion are known to be unstable towards ring contraction to croconate dianion, the process being faster in alkaline solution;⁴⁶ this explains why **1a** could not be formed with a 4-pyBA/Na rhodizonate 2:1 stoichiometry but required a lower concentration of the pyridine-substituted boronic acid.

*The molecular and crystal structure of the "axle" compounds
1a·2H₂O, 1a·4H₂O, and 1b·2.5H₂O*

1a and **1b** are characterized by the same molecular unit, that is an adduct of a pyridine- (or pyrimidine-) boronic acid moiety and a dodecahydroxycyclohexane-like moiety in a 2:1 stoichiometry. The compound is a boronate ester, formed from the condensation of the acidic functions and the hydroxyls groups belonging to the cyclohexane. The C₆ ring represents the center of mass of the molecule carrying the two boronic moieties on opposite sides; the mean plane of the C₆ ring is perpendicular to the axis passing through the two aromatic rings and the boron atoms. The boron atoms are connected to three oxygen atoms and one carbon atom in a tetrahedral geometry. The tetrahedral boron atom bears a formal negative charge, which is balanced by the positively charged N-H found on the aromatic rings. H atoms of the protonated heterocycles were located from the Fourier maps, so the molecule is overall neutral, containing two zwitterionic couples. In **1a** the aromatic moiety is a pyridinium ring while in **1b** is a pyrimidinium.

1a crystallized in the monoclinic space group P2₁/c as a dihydrate. See Figure 2.3.2a for a representation of the packing and of the hydrogen bond network involving the water molecules. An inversion center sits in the mean plane of the C₆ ring, therefore Z' = 0.5. The boron atom has a slightly distorted tetrahedral geometry: the smallest angle is 107.9(2)° while the largest is 111.2(2)°. The aromatic C- and N-atoms are disordered over 2 positions: not only the pyridine ring is rotated on the C₂ axis in the second conformation, but it is also slightly bent on one side. This deviation can be attributed to the different interactions of the pyridinium hydrogen in the two conformations (Figure 2.3.2b): in one case the H-atom interacts with one dangling OH group and one bridging B–O–C oxygen of the neighboring molecule, namely O5 and O3, with N···O distances 2.86(1) Å and 3.01(2) Å respectively; in the other case the interactions are with O5 and a different bridging oxygen, O1, with distances 2.75(1) Å and 3.27(2) Å respectively.

Occupancies for the different positions were refined to 50%. A data collection was repeated at 200 K in order to assess the static or dynamic type of the disorder. Disordered positions could be refined in the low-temperature structure as well with the same relative occupancies, thus suggesting a static disorder.

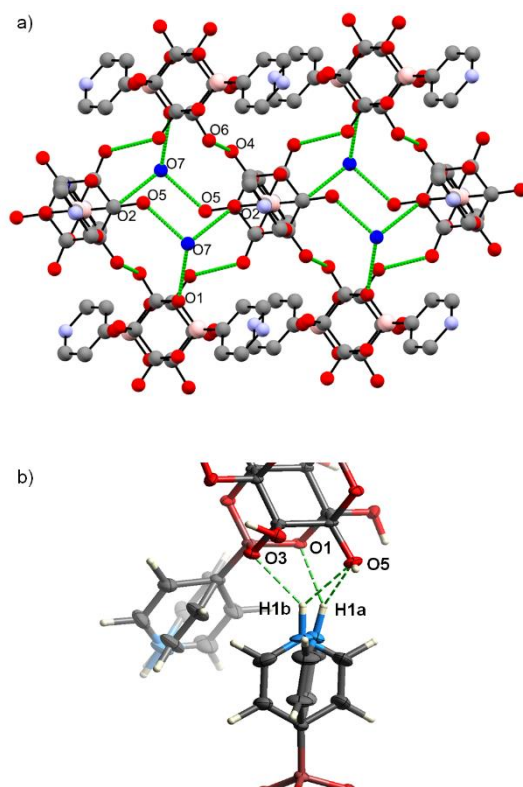


Figure 2.3.2 a) Hydrogen bonding network in the crystal structure of **1a**·2H₂O (water molecules are depicted in blue for clarity); b) a detail of the two different conformations of the pyridinium moiety and their respective hydrogen bonds (thermal ellipsoids drawn at 50 % of probability).

The packing of **1a**·2H₂O is mainly directed by intermolecular hydrogen bonds, with water of crystallization playing a primary role. Each water molecule is bonded to one hydroxyl group and two bridging B–O–C, the three oxygen atoms belonging to three different molecules. The remaining hydroxyls (O4 and O6) are employed in H-bonds with the hydroxyls of an adjacent molecule. Summarizing, each molecule has 6 hydroxyls on the central C₆ ring and 6 bridging O-atoms, 3 for each boron atom. Of the six hydroxyls, two are bonded to water molecules and the other four are employed in intermolecular O–H···O–H contacts. Four of the B–O–C oxygens are bonded to water molecules, while two of them interact with the pyridinium proton.

1b crystallized in the monoclinic space group P2₁/c as a 2.5 hydrate. As in the case of **1a** an inversion center coincides with the center of gravity of the molecule so that the asymmetric unit comprises one boron atom, one aromatic ring and half of the central C₆ ring. The aromatic moiety consists of a pyrimidine ring, possessing one protonated nitrogen atom. The molecule is found to be 2.5 hydrated: one water molecule sits near an inversion center and

was therefore refined as a disordered O-atom with half occupancy. As in the case of **1a**·2H₂O, the packing of **1b**·2.5H₂O is directed by hydrogen bonds and water of crystallization is fundamental in this regard. Unlike in **1a**·2H₂O, though, the different position of the N-H moiety contributes to form infinite chains of charge-assisted hydrogen bonds, that run along a-axis (Figure 2.3.3a). Small channels are formed by 4 adjacent chains and are filled by water molecules. All oxygen atoms in this crystal structure are involved in hydrogen bonds; similarly to the case of **1a**·2H₂O, the crystal packing maximizes the extent of hydrogen bonding.

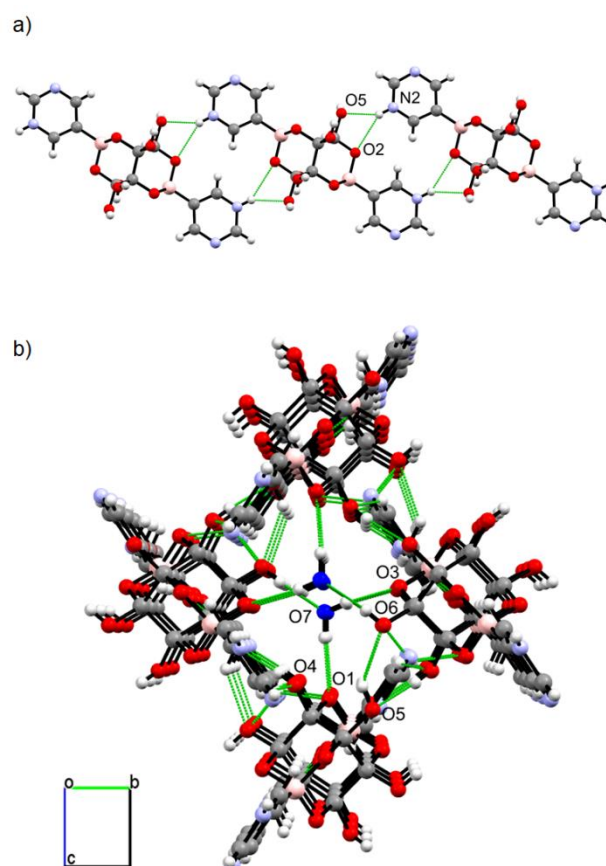


Figure 2.3.3 a) Representation of the infinite chains of hydrogen bonds in the crystal structure of **1b**·2.5H₂O; b) view of the packing of the chains along an axis; water of crystallization was pictured in blue for clarity.

1a·4H₂O crystallizes in the triclinic P-1 space group. At variance with **1a**·2H₂O disorder is observed in the central C₆ moiety rather than in the aromatic rings. The C₆ ring adopts the two inverted chair conformations characterized by an opposite axial/equatorial topology of the substituents. This

disorder is coherent with the different symmetry of the structure: the two pyridinic rings are not equivalent due to the interactions with the water of crystallization; hence the two boron atoms, and the related ester linkages are not equivalent, giving rise to two non-equivalent conformations for the cyclohexane ring. As expected, the higher amount of crystallization water produces a rather crowded network of hydrogen bonds. The structure, though, can be ideally divided into layers characterized by a different number of H-bonds. Hydroxyl groups and ester oxygens are employed in H-bonds that are directed mainly along the radial direction (with respect to the N–B–B–N axis) and are connected to homologue groups of the surrounding molecules (red stripe in Figure 2.3.4), while the aromatic rings are spatially close without showing any kind of stacking interaction (blue stripe in Figure 2.3.4).

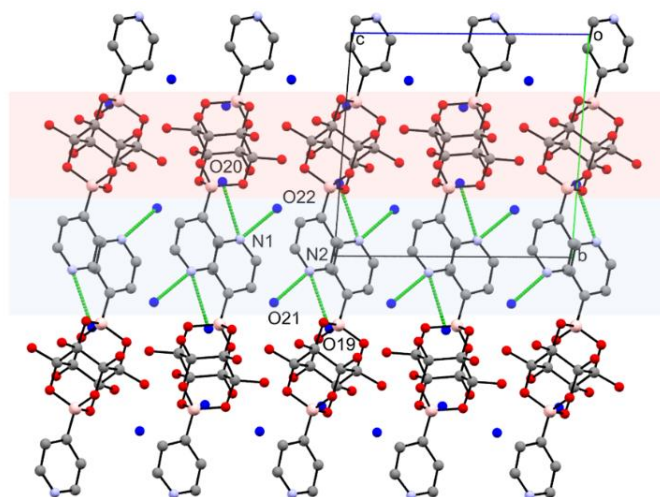


Figure 2.3.4 Representation of the crystal packing of $1a \cdot 4H_2O$ on the bc plane; the red stripe represents the preferential direction of the $OH \cdots O$ bonds, while the blue one is characterized by only a few H-bonds; the different environment of the two $N-H^+$ groups is also shown, due to non-equivalent water molecules (depicted in blue).

The molecular and crystal structures of the “tweezer” compounds $2a \cdot 3H_2O$ and $2b \cdot 3H_2O$

2a and **2b** are products of the esterification of 4-pyridine boronic acid and pyrimidine-5-boronic acid with rhodizonic acid dihydrate, with the same stoichiometry 2:1. Here, though, rhodizonic acid retains the structure of its dihydrate form $C_6H_8O_8$ (2,3,5,5,6,6-hexahydroxycyclohex-2-ene-1,4-dione), that has been shown to be the stable form at room temperature, pressure, and

humidity.⁴⁷ The ring is indeed planar and undergoes condensation with the boronic acids at the two germinal diols.

In **2a**·3H₂O the rhodizonic acid moiety is planar and the carboxylic C–O bonds have distances of 1.22(1) Å and 1.23(1) Å, that are consistent with a double bond. The coordination of the two boron atoms is a distorted tetrahedral geometry: the O–B–O angles involving the ester oxygens are 103.4(6)° and 104.2(6)°. The two pyridinic rings lay on parallel planes, at a distance of 3.603 Å (centroid–mean plane), so it is possible that stacking interactions further stabilize the structure. The most recognizable motif in the crystal packing of **2a**·3H₂O is the formation of a ladder through NH··O and OH··O bonds involving two water molecules, as shown in Figure 2.3.5a. The ladders are disposed on planes that are stacked with water molecules in between.

In **2b**·3H₂O the rhodizonic ring is planar, the carboxylic C–O bonds are consistent with double bonds [1.213(4) Å and 1.216(4) Å] and the two O–B–O angles are 104.7(2)° and 104.2(2)°. One of the two arms of the tweezer is more unfolded than the other: the dihedral angles C_{rhodizonic}–O–B–C_{pyrimidine} in the two cases are 132.0(2)° and 115.8(3)°. Moreover, the two aromatic rings are rotated with respect to the mean plane of the rhodizonic acid moiety by 47.10° and 45.88° respectively. Thanks to this rotation a pile is formed, with adjacent molecules interacting through displaced π–π stacking (centroid–mean plane distance: 3.355 Å) and OH··O bonds involving two hydroxyls and two B–O–C oxygen atoms (O2, O6, O3, O4 in Figure 2.3.5d). Also, a ladder motif is formed with similar H-bonds topology to that of **2a**·3H₂O (Figure 2.3.5c), only in this case the tweezer units are piled in ABAB sequence with an inversion center between each molecule. Finally, it is noteworthy that the water molecules do not take part in the main packing motif but are rather clustered into interstitial space; this feature is relevant in the thermal behavior of the compound, that will be discussed in the following. Although it is known that boronic acids are capable in the stabilization of water clusters,^{48, 49} it appears in this case that the formation of trimers of water molecules is dictated by the optimization of the crystal packing rather than some peculiar water–water interactions.

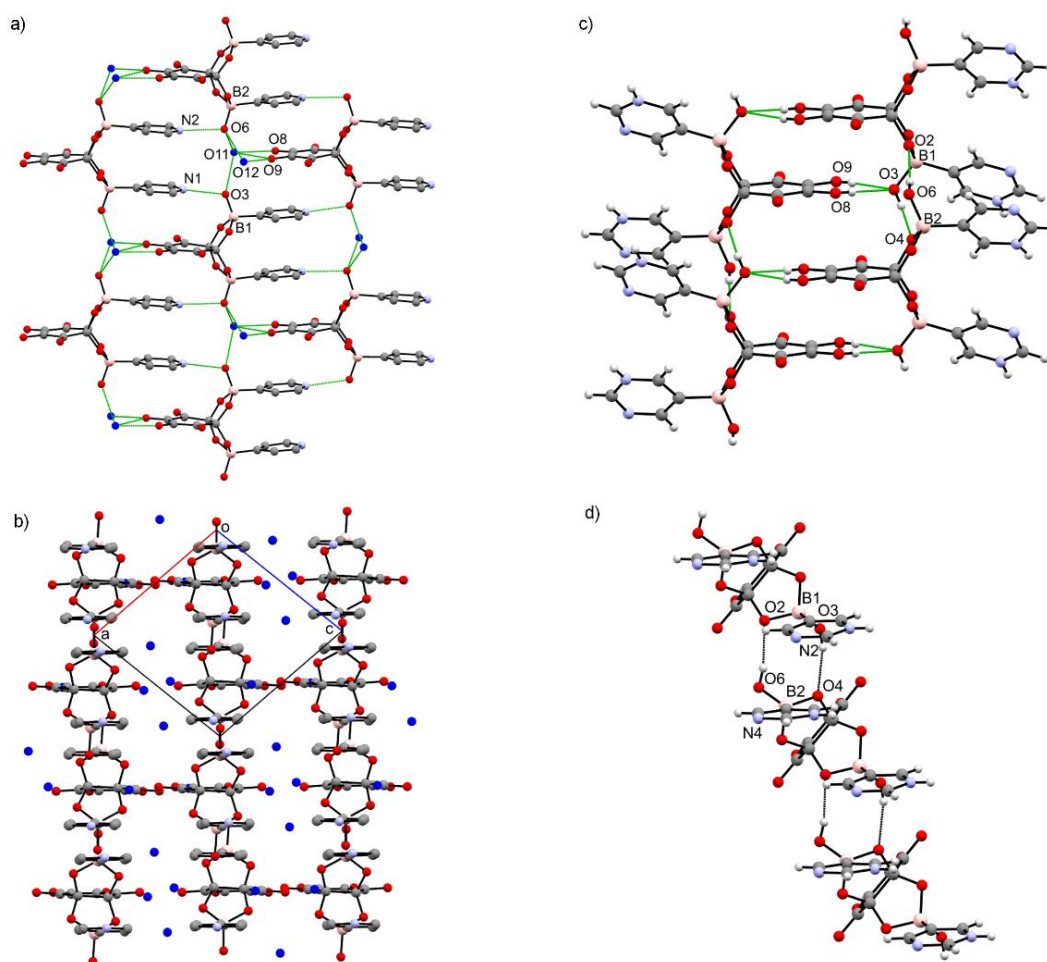


Figure 2.3.5 a) Representation of the ladder disposition of **2a**·3H₂O and the corresponding hydrogen bonding motif; b) view of the crystal structure of **2a**·3H₂O along *b* axis: the ladders' planes are stacked with water molecules in between them (represented in blue); view of the packing motif of **2b**·3H₂O c) along the plane of the rhodizonic acid moiety and d) along the planes containing the pyrimidine rings.

Thermal stability of 2a·3H₂O and 2b·3H₂O

The thermal behavior of **2a**·3H₂O and **2b**·3H₂O was investigated by means of TGA and variable temperature XRD measurements. The TGA trace of **2a**·3H₂O shows a first loss of water with a broad transition in the temperature range 35–100 °C, corresponding to the loss of approximately 1.5 molecules of water, followed by a second larger loss with onset at 115 °C and offset at 180 °C, that presumably corresponds to degradation of the boronate ester. The TGA of **2b**·3H₂O shows again a broad loss of water that stops at 120 °C, corresponding to the loss of 2.5 molecules of water, followed by degradation. In both cases, it is difficult to quantify precisely the amount of water lost since

the weight loss appears to be happening already at 35 °C, at the start of the measurement (Figure S1 and S2).

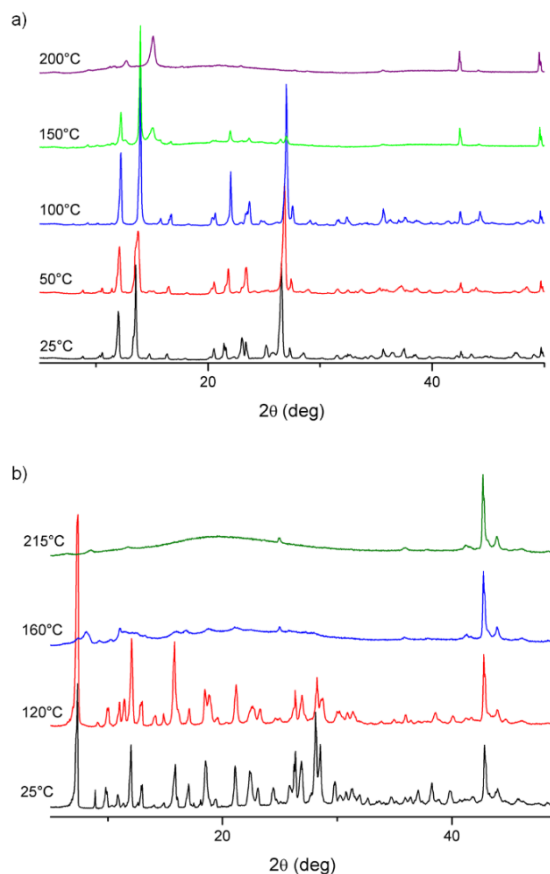


Figure 2.3.6 Variable temperature XRPD patterns of **2a**·3H₂O (a) and **2b**·3H₂O (b); the peaks at $2\theta = 43^\circ$ and 50° are due to the sample holder; all the patterns in a column have the same scale.

X-ray powder patterns of the two compounds were collected at high temperature to probe the dehydration. It is shown that both **2a**·3H₂O and **2b**·3H₂O, at 100 °C and 120 °C respectively, maintain their crystallinity upon the partial dehydration occurring in agreement with the thermal analyses. The loss of water coincides with a slight structural change: for example, in the case of **2a**·3H₂O, it is possible to see the presence of both hydrate and dehydrate forms at 50 °C (Figure 2.3.6). At 150 °C, corresponding to the second weight loss in the TGA curve, amorphization of the compound is observed. **2b**·3H₂O exhibit similar behavior, displaying a slight structural rearrangement at 120 °C and, above that temperature, progressive

amorphization of the sample. It is noteworthy that in both cases the intensity of the most prominent peaks seems to be increased after the dehydration.

It was also observed that in the case of **2b**·3H₂O the dehydration proceeds in a single-crystal to single-crystal fashion. Optical microscope pictures of Figure 2.3.7 show that the crystal becomes darker after water removal. It was found that the process is slower in this case with respect to a microcrystalline sample, indeed the dehydration was complete after roughly 6 hours. The process is also reversible, with rehydration taking as long as 48 hours. Single crystal data were then collected for **2b**·3H₂O after 3 hours of heating at 120 °C and after more than 6 hours. From the data collected after 3 hours, a structure was successfully determined that is characterized by three independent water molecules, whose occupancies were refined to roughly 65 %, 63 %, and 35 %, respectively. Notably, those water molecules do not occupy the same crystallographic sites as in the starting phase, as the structure is overall different: a structural rearrangement occurs upon partial dehydration without loss of symmetry, since the space group remains *P2₁/n*, and with only a slight change of the cell parameters (see Table 2.3.1).

Table 2.3.1 Comparison of the cell parameters of the differently hydrated forms of **2b**

compound	2b ·3H ₂ O	2b ·xH ₂ O (0.5 < x < 3)	2b ·0.5H ₂ O
s. g.	<i>P2₁/n</i>	<i>P2₁/n</i>	<i>P2₁/n</i>
<i>a</i> [Å]	6.8473(2)	6.8191(7)	6.7965(1)
<i>b</i> [Å]	15.8091(5)	15.836(2)	15.970(1)
<i>c</i> [Å]	17.6326(6)	17.562(2)	17.530 (2)
β [°]	100.422(3)	100.47 (1)	99.475(1)
vol. [Å ³]	1877.2(1)	1865.0(3)	1876.8(4)
<i>T</i>	r.t.	270 K	270 K

The main feature of this partially dehydrated structure is that the pyrimidinium rings are rotated at roughly 90° with respect to the starting structure. Moreover the two N-H groups both point inward, that is in opposite directions, rather than pointing in the same direction as in the tri-hydrate form (Figure 2.3.8a). The data collected after 6 hours of heating show instead a structure defined by the same structural motif as the tri-hydrate form (the two structures are almost superimposable), but the positions of the three water molecules are no longer identifiable from the Fourier maps.

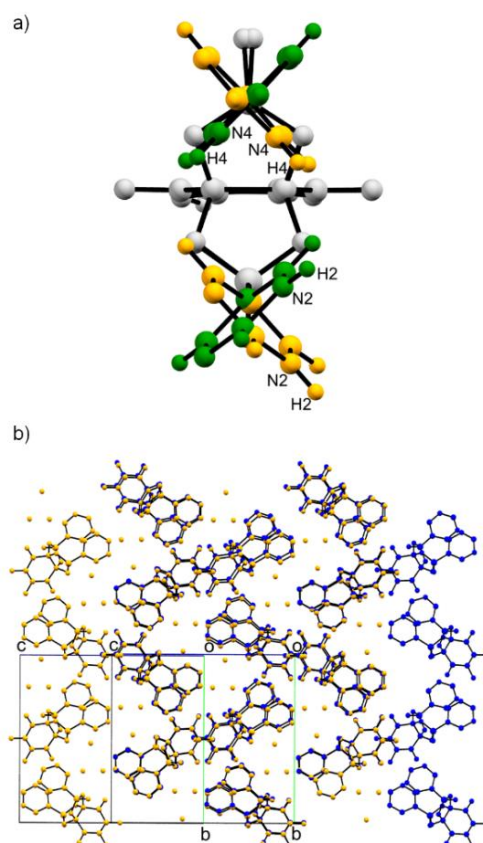


Figure 2.3.7 a) Comparison of the different conformations of the tri-hydrate form of **2b** (yellow) and the partially dehydrated form (green); b) superimposition of the packing motifs of the tri-hydrate form of **2b** (yellow) and the 0.5-hydrate form (blue): the unit cell of the latter is shifted by $1/2c$ along the direction of the c axis.

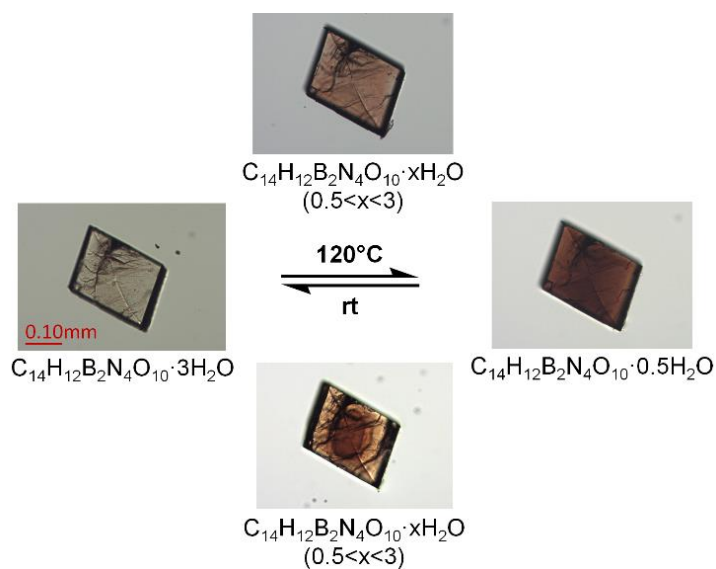


Figure 2.3.8 Optical microscope images of the tri-hydrate form (left), the 0.5 hydrate form (right) and the partially dehydrated forms of **2b** obtained from the dehydration and re-hydration processes (top and bottom respectively).

What is observed instead is a disordered electron density that has the same shape as the voids created by the removal of the solvent. It appears, thus, that the remaining water of crystallization is disordered inside the cavities created by the dehydration process (see Figure S17 and Figure S18). The residual Fourier peaks of the refined model account for a total of $5.12 e/\text{\AA}^3$, which seems compatible with the 0.5 water molecules left after dehydration, as assessed by the TGA measurements. Interestingly in this 0.5-hydrated structure, the heteroaromatic rings exhibit the same orientation as in the trihydrate structure, with the two N-H pointing in the same direction. So, it is possible to assume that the dehydration process is achieved through a rotation of the pyrimidinium rings on the B–C bond, and concomitantly a structural rearrangement to a metastable structure that permits the expulsion of water, otherwise impossible since the voids of the 0.5-hydrated form are not connected to each other. It is remarkable that such a complex phenomenon, that in a way is similar to a plastic behavior, occurs without compromising the integrity of the crystal.

2.3.3 Conclusions

In this work, we have reported the preparation and full structural characterization by X-ray single crystal and powder diffraction as well as the investigation of the thermal stability and behavior upon dehydration of four novel adducts of boronic acid derivatives with the oxocarbon acid rhodizonic acid. We have shown that 4-pyridinylboronic acid and pyrimidine-5-boronic acid react with rhodizonic acid in a similar way producing two distinct products, that we have called, respectively, “axle” (**1**) and “tweezer” (**2**) based on the structural features. The two types of architectures are obtained as a function of the experimental conditions. Both compounds are in the zwitterionic form with the boronate ion being neutralized via protonation on the pyridinyl and pyrimidine N-terminus.

The “tweezer” and “axle” compounds are obtained concomitantly in solution preparations, although the ratio between “axle” and “tweezer” can be varied by changing the crystallization conditions. From solution, slow cooling of the liquid leads predominantly to retrieve crystals of the “axle” compound while mechanochemical reaction between boronic acid and rhodizonic acid affords exclusively the tweezer-type compounds. On the basis of these

observations, it seems reasonable to hypothesize that “axles” and “tweezers” in solution are related by a chemical equilibrium, which is shifted towards the “axle” compound as this latter, less soluble, precipitates out upon cooling of the solution. In this respect, the “axle” compound appears to be the thermodynamic product of the reaction while the “tweezer” is kinetically favored. It is interesting to note that these compounds were obtained in a “failed” attempt to grow co-crystals of rhodizonic acid and of the boronic acids, although these latter compounds are known to form co-crystals with a number of cofomers.⁵⁰⁻⁵² The outcome has been, admittedly, unexpected affording an entirely new class of adducts, which, for their zwitterionic nature may well prove useful in the construction of frameworks or supramolecular aggregates. The exploration of these possibilities is ongoing.

2.3.4 Experimental Section

All reagents were purchased from Sigma-Aldrich and used as received. Rhodizonic acid dihydrate was alternatively prepared in the laboratory following the procedure described below. All experiments and syntheses were conducted in air.

Synthesis of rhodizonic acid. In a typical procedure, sodium rhodizonate dibasic is dissolved in deionized water and 2 eq. of hydrochloric acid are added dropwise under vigorous stirring. Upon addition of the acid, the color of the solution changes from dark brown to yellow. The solution is then dried with a rotating evaporator. The resulting brown solid is washed with THF and vacuum filtered to separate insoluble NaCl. This step is repeated three times. Finally, the collected organic phases are mixed and dried with a rotating evaporator to yield a brown solid. The purity of rhodizonic acid was confirmed by powders XRD and FT-IR analyses (see Figure S3 and Figure S5).

Synthesis of 1a–2a (in solution). Rhodizonic acid dihydrate (85 mg, 0.40 mmol) and 4-pyridinylboronic acid (99 mg, 0.80 mmol) were mixed in 10 mL of deionized water. The suspension was heated at 100 °C under vigorous stirring until complete dissolution of the boronic acid was achieved, and a yellowish-grayish solution was formed. The solution was then filtered through a 0.45 µm PTFE filter and cooled to room temperature. After 1 day orange block crystals

of **2a**·3H₂O were observed in the mother liquors along smaller plate crystals of **1a**·2H₂O. In another experiment, the cooling rate was diminished by filtering the solution in a sealed vial which was then inserted in a dewar container filled with boiling water and left to slowly cool down to room temperature overnight. In this case, bigger crystals of **1a**·2H₂O were observed along traces of **2a**·3H₂O. It is also noteworthy that the solution retained a more intense color, suggesting an overall lower degree of precipitation. Alternatively, if sodium rhodizonate dibasic (34.7 mg, 0.16 mmol) was used instead of rhodizonic acid, this was dissolved in 5 mL of water and 4-pyridineboronic acid was added (20 mg, 0.16 mmol) and the mixture heated until a red solution was formed; colorless crystals of **1a**·4H₂O were obtained after 1 day on cooling to room temperature.

Synthesis of 1b–2b (in solution). **1b** and **2b** were prepared following the same procedure described for **1a–2a** except using pyrimidine-5-boronic acid instead of 4-pyridineboronic acid. Upon cooling of the hot solution orange prismatic crystals of **2b**·3H₂O crystallized along with colorless plates (**1b**·2.5H₂O). Each synthesis was repeated three times and afforded always the same ratio of **1** and **2**. The ratio of the two types of compounds was evaluated via Rietveld refinement performed on the XRPD pattern of the bulk polycrystalline samples (see below for details).

Mechanochemical synthesis of 2a–2b. In a typical experiment, rhodizonic acid dihydrate was placed in an 8 mL steel jar with 2 equivalents of the appropriate boronic acid. 3–4 drops of water were then added and the mixture was ball-milled for 90 minutes at 20 Hz using a Retsch MM120 ball-mill.

Structures determination. Single crystal X-ray diffraction data were collected at room temperature with an Oxford Diffraction X'Calibur diffractometer equipped with a graphite monochromator and a CCD detector. Mo-*K*_α radiation ($\lambda = 0.71073 \text{ \AA}$) was used. The unit cell parameters were determined by means of a 15 frames pre-experiment. The measured intensities were reduced to F^2 and corrected for absorption, Lorentz and polarization effects with CrysAlisPro. The structures were solved with SHELXT⁵³ and refined on full-matrix F^2 by means of SHELXL package, implemented in Olex2 software.^{54, 55} In all the structures except for **1a**·4H₂O non-hydrogen atoms

were refined anisotropically, while hydrogen atoms were placed in calculated positions using a riding model. O–H hydrogen atoms were located in the Fourier maps. In the structure of **1a**·4H₂O atoms C1a, C1b, C2a, C2b, C3a, C3b, C9a, C9b, C10a, C10b, C11a, C11b are disordered having very close positions; any attempt to refine anisotropically such atoms were unsuccessful, so they were refined isotropically. In compound **1b**·2.5H₂O a disordered water molecule sits near a crystallographic inversion center creating an artefact O–O bond. In this case, only the oxygen atom was refined with half occupancy, while the hydrogen atoms were not placed. Data collection and refinement details are listed in Table S1 and Table S2.

[CCDC](#) 1866521 (for **1a**·2H₂O), 1866522 (for **1a**·4H₂O), 1866523 (for **2a**·3H₂O), 1866524 (for **1b**·2.5H₂O), 1866525 (for **2b**·3H₂O), 1866526 (for **2b**·1.5H₂O), and 1866527 (for **2b**·0.5H₂O) contain the supplementary crystallographic data for this paper. These data can be obtained free of charge from [The Cambridge Crystallographic Data Centre](#)

Powder Diffraction. XRPD routine analyses were performed on a PANalytical X'Pert Pro automated diffractometer equipped with an X'Celerator detector in Bragg–Brentano geometry, using Cu-*K*_α radiation ($\lambda = 1.5418 \text{ \AA}$) without monochromator in the 2θ range between 3° and 50° (continuous scan mode, step size 0.0167°, counting time 19.685 s, Soller slit 0.04 rad, antiscatter slit 1/2, divergence slit 1/4, 40 mA*40 kV). XRPD analyses for Rietveld refinement purposes were instead performed on a PANalytical X'Pert Pro automated diffractometer equipped with a PIXcel detector in transmission geometry, using Cu-*K*_α radiation ($\lambda = 1.5418 \text{ \AA}$) without monochromator in the 2θ range between 3° and 70°s (continuous scan mode, step size 0.0260°, counting time 889.70 s, Soller slit 0.02, antiscatter slit 1/2, divergence slit 1/2, 40 mA*40 kV). Powder diffraction data were analyzed with the software TOPAS 5.⁵⁶ Difference patterns and figure of merits of the Rietveld refinements are reported in the supporting information.

Infrared Spectroscopy. FTIR spectra were acquired in the 400–4000 cm⁻¹ range on a Bruker APLHA platinum ATR spectrometer, equipped with a diamond attenuated total reflectance (ATR) module.

Thermogravimetry. TGA measurements were performed with a PerkinElmer TGA7 in the temperature range 40–300 °C under nitrogen gas flow at a heating rate of 10.00 °C min⁻¹.

Cross-polarized Hot Stage Optical Microscopy. CPHSM were carried out using a Linkam TMS94 device connected to a Linkam LTS350 platinum plate and equipped with polarizing filters. Images and movies were collected with the imaging software VisiCam Analyzer, from an Olympus BX41 stereomicroscope.

References

- (1) N. Miyaoura, A. Suzuki, *Chem. Rev.* **1995**, 95, 2457–2483.
- (2) P. R. Parry, C. Wang, A. S. Batsanov, M. R. Bryce, B. Tarbit, *J. Org. Chem.* **2002**, 67, 7541–7543.
- (3) W. Yang, X. Gao, B. Wang, *Med. Res. Rev.* **2003**, 23, 346–368.
- (4) P. G. Richardson, B. Barlogie, J. Berenson, S. Singhal, S. Jagannath, D. Irwin, S. V. Rajkumar, G. Srkalovic, M. Alsina, R. Alexanian, et al., *N. Engl. J. Med.* **2003**, 348, 2609–2617.
- (5) S. J. Baker, T. Akama, Y. K. Zhang, V. Sauro, C. Pandit, R. Singh, M. Kully, J. Khan, J. Plattner, S. J. Benkovic, et al., *Bioorg. Med. Chem. Lett.* **2006**, 16, 5963–5967.
- (6) R. Nishiyabu, Y. Kubo, T. D. James, J. S. Fossey, *Chem. Commun.* **2011**, 47, 1106.
- (7) X. Sun, T. D. James, *Chem. Rev.* **2015**, 115, 8001–8037.
- (8) W. L. A. Brooks, B. S. Sumerlin, *Chem. Rev.* **2016**, 116, 1375–1397.
- (9) Y. Kubo, R. Nishiyabu, D. James, *Chem. Commun.* **2015**, 51, 2005–2020.
- (10) H. Zheng, D. G. Hall, *Aldrichim. Acta* **2014**, 47, 41–51.
- (11) R. Nishiyabu, Y. Kubo, T. D. James, J. S. Fossey, *Chem. Commun.* **2011**, 47, 1124–1150.
- (12) K. Severin, *Dalton Trans.* **2009**, 5254–5264.
- (13) H. Furukawa, O. M. Yaghi, *J. Am. Chem. Soc.* **2009**, 131, 8875–8883.
- (14) G. Springsteen, B. Wang, *Tetrahedron* **2002**, 58, 5291–5300.
- (15) S. D. Bull, M. G. Davidson, J. M. H. Van Den Elsen, J. S. Fossey, A. T. A. Jenkins, Y. B. Jiang, Y. Kubo, F. Marken, K. Sakurai, J. Zhao, et al., *Acc. Chem. Res.* **2013**, 46, 312–326.
- (16) J. Yan, G. Springsteen, S. Deeter, B. Wang, *Tetrahedron* **2004**, 60, 11205–11209.
- (17) Ref. (6).
- (18) J. H. Fournier, T. Maris, J. D. Wuest, W. Guo, E. Galoppini, *J. Am. Chem. Soc.* **2003**, 125, 1002–1006.
- (19) N. Luisier, K. Bally, R. Scopelliti, F. T. Fadaei, K. Schenk, P. Pattison, E. Solari, K. Severin, *Cryst. Growth Des.* **2016**, 16, 6600–6604.
- (20) G. Campillo-Alvarado, E. C. Vargas-Olvera, H. Höpfl, A. D. Herrera-España, O. Sánchez-Guadarrama, H. Morales-Rojas, L. R. MacGillivray, B. Rodríguez-Molina, N. Farfán, *Cryst. Growth Des.* **2018**, 18, 2726–2743.
- (21) J. F. Heller, *Ann. Pharm.* **1837**, 24, 1–16.
- (22) R. West, *Isr. J. Chem.* **1980**, 20, 300–307.
- (23) G. Seitz, P. Imming, *Chem. Rev.* **1992**, 92, 1227–1260.
- (24) D. Braga, L. Maini, F. Grepioni, *Chem. Eur. J.* **2002**, 8, 1804–12.
- (25) H. Chen, M. Armand, M. Courty, M. Jiang, C. P. Grey, F. Dolhem, J.-M. Tarascon, P. Poizot, *J. Am. Chem. Soc.* **2009**, 131, 8984–8988.
- (26) M. Lee, J. Hong, J. Lopez, Y. Sun, D. Feng, K. Lim, W. C. Chueh, M. F. Toney, Y. Cui, Z. Bao, *Nat. Energy* **2017**, 2, 861–868.

- (27) J. Tian, D. Cao, X. Zhou, J. Hu, M. Huang, C. Li, *ACS Nano* **2018**, <https://doi.org/acs.nano.7b09177>.
- (28) O. Dalby, D. Butler, J. W. Birkett, *J. Forensic Sci.* **2010**, *55*, 924–943.
- (29) M. Wierzbicka, J. Obidzińska, *Plant Sci.* **1998**, *137*, 155–171.
- (30) D. A. Kunkel, J. Hooper, S. Simpson, S. Beniwal, K. L. Morrow, D. C. Smith, K. Cousins, S. Ducharme, E. Zurek, A. Enders, *J. Phys. Chem. Lett.* **2013**, *4*, 3413–3419.
- (31) S. Chen, A. Enders, X. C. Zeng, *Chem. Mater.* **2015**, *27*, 4839–4847.
- (32) D. Braga, F. Grepioni, L. Maini, S. D'Agostino, *IUCrJ* **2017**, *4*, 369–379.
- (33) L. Fornasari, R. Mazzaro, E. Boanini, S. d'Agostino, G. Bergamini, F. Grepioni, D. Braga, *Cryst. Growth Des.* **2018**, *18*, 7259–7263.
- (34) C. B. Aakeröy, J. Desper, B. Levin, *CrystEngComm* **2005**, *7*, 102–107.
- (35) P. Rodríguez-Cuamatzi, O. I. Arillo-Flores, M. I. Bernal-Uruchurtu, H. Höpfl, *Cryst. Growth Des.* **2005**, *5*, 167–175.
- (36) H. Kara, C. J. Adams, A. G. Orpen, T. J. Podesta, *New J. Chem.* **2006**, *30*, 1461.
- (37) Y. Yahsi, E. Gungor, H. Kara, *Cryst. Growth Des.* **2015**, *15*, 2652–2660.
- (38) J. J. Campos-Gaxiola, A. Vega-Paz, P. Román-Bravo, H. Höpfl, M. SánchezVázquez, *Cryst. Growth Des.* **2010**, *10*, 3182–3190.
- (39) D. G. Hall, in *Boronic Acids Prep. Appl. Org. Synth. Med. Mater. 1&2, Second Ed.* Wiley-VCH Verlag GmbH & Co. KGaA, Weinheim, Germany, **2011**, pp. 1–133.
- (40) R. I. Gelb, L. M. Schwartz, D. A. Laufer, *J. Phys. Chem.* **1978**, *82*, 1985–1988.
- (41) J. W. Tomsho, S. J. Benkovic, *J. Org. Chem.* **2012**, *77*, 2098–2106.
- (42) L. Zhu, S. H. Shabbir, M. Gray, V. M. Lynch, S. Sorey, E. V. Anslyn, *J. Am. Chem. Soc.* **2006**, *128*, 1222–1232.
- (43) Y. Yamamoto, M. Takizawa, X.-Q. Yu, N. Miyaura, *Angew. Chem. Int. Ed.* **2008**, *47*, 928–931; *Angew. Chem.* **2008**, *120*, 942.
- (44) S. Kuno, T. Kimura, M. Yamaguchi, *Tetrahedron Lett.* **2014**, *55*, 720–724.
- (45) I. S. Golovanov, A. Y. Sukhorukov, Y. V. Nelyubina, Y. A. Khomutova, S. L. Ioffe, V. A. Tartakovskiy, *J. Org. Chem.* **2015**, *80*, 6728–6736.
- (46) B. Zhao, M. H. Back, *Can. J. Chem.* **1991**, *69*, 528–532.
- (47) D. Braga, G. Cojazzi, L. Maini, F. Grepioni, *New J. Chem.* **2001**, *25*, 1221–1223.
- (48) P. Rodríguez-Cuamatzi, G. Vargas-Díaz, H. Höpfl, *Angew. Chem. Int. Ed.* **2004**, *43*, 3041–3044; *Angew. Chem.* **2004**, *116*, 3103.
- (49) K. Durka, K. N. Jarzemska, R. Kamiński, S. Luliński, J. Serwatowski, K. Woźniak, *Cryst. Growth Des.* **2013**, *13*, 4181–4185.
- (50) V. R. Pedireddi, N. SeethaLekshmi, *Tetrahedron Lett.* **2004**, *45*, 1903–1906.
- (51) S. Varughese, S. B. Sinha, G. R. Desiraju, *Sci. China Chem.* **2011**, *54*, 1909–1919.
- (52) M. Petroselli, S. Mosca, J. Martí-Rujas, D. Comelli, M. Cametti, *Eur. J. Org. Chem.* **2017**, 7190–7194.
- (53) G. M. Sheldrick, *Acta Crystallogr. Sect. A Found. Crystallogr.* **2015**, *71*, 3–8.
- (54) G. M. Sheldrick, *Acta Crystallogr. Sect. C Struct. Chem.* **2015**, *71*, 3–8.
- (55) O. V. Dolomanov, L. J. Bourhis, R. J. Gildea, J. A. K. Howard, H. Puschmann, *J. Appl. Crystallogr.* **2009**, *42*, 339–341.
- (56) A. Coelho, *TOPAS-Academic V5*, Coelho Software, Brisbane, Australia, **2012**

2.4 Supramolecular Zwitterions Based on a Novel Boronic Acid–Squarate Dianion Synthron

Reproduced from Ref. [Fornasari, L.; D'Agostino, S.; Braga, D. *CrystEngComm* **2019**, *21* (20), 3186–3191.] with permission from the Royal Society of Chemistry.
<http://xlink.rsc.org/?DOI=C9CE00367C>

2.4.1 Introduction

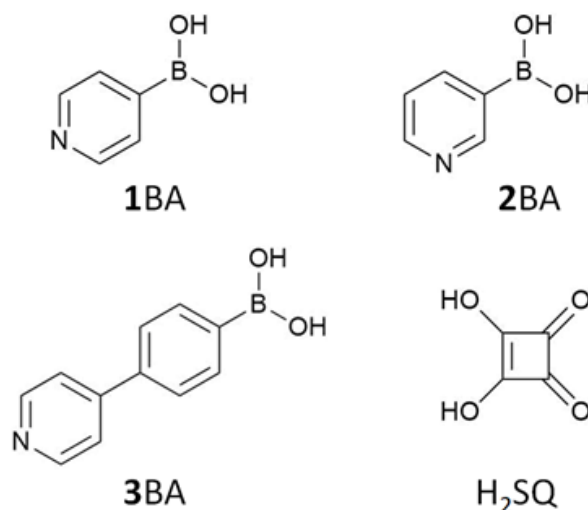
In supramolecular chemistry and crystal engineering,¹ the understanding of the recognition patterns between complementary functional groups is of vital importance to design novel materials with desired physical and chemical properties.^{2,3} Hydrogen bonding, in particular, is one of the most employed tools to this end, as the modulation of its strength, directionality and selectivity enables the construction of a plethora of different architectures.^{4,5}

Boronic acids have been widely employed in organic and medicinal chemistry.^{6,7} Besides, in recent years, they have also been the object of intensive study in the fields of sensing⁸ and organic catalysis,⁹ as well as in supramolecular chemistry.^{10,11} Their unique ability to reversibly bind diols has been employed, for example, in the preparation of glucose sensors and of highly-porous covalent organic frameworks (COFs).^{12,13}

Even though most of the mentioned applications are based on the peculiar covalent chemistry of boronic acids, they possess a versatile toolbox of non-covalent interactions that can prove useful in engineering of supramolecular architectures.^{14,15} We were recently drawn to study some heteroaromatic-substituted boronic acids as building blocks for single- and multi-component crystals.^{16,17} Such molecules are sometimes referred to as self-complementary tectons,¹⁸ in that they can produce polymeric and macrocyclic structures based on weak B–N bonds. At the same time, pyridine-appended boronic acids, owing to their amphoteric character, are useful in the stabilization of ionic species through hydrogen bonds.^{17,19–21} The $-B(OH)_2$ function exists in three different conformations: the energetically favoured *syn,anti*, the *anti,anti* and the *syn,syn*-conformation.²² Notably, the stabilization of the unfavourable *syn,syn*-conformer by co-crystallization with aza-aromatic compounds was recently exploited for the synthesis of polymeric H-bonded structures and to direct a [2 + 2] photocyclization reaction in the solid state.^{23,24} Moreover, the design of hydrogen-bonded multicomponent crystals of boronic acids is emerging as a

promising tool for the modification of the chemical and physical properties of these solids.^{25,26}

With this in mind, we explored the co-crystallization of three heteroaryl boronic acids, namely 4-pyridinylboronic acid (**1BA**), 3-pyridinylboronic acid (**2BA**), and (4-(pyridin-4-yl)phenyl)boronic acid (**3BA**) with squaric acid (H_2SQ), see Scheme 2.4.1. Squaric acid belongs to the family of oxocarbons and is a strong diprotic acid ($\text{p}K_{\text{a}1} = 0.55$, $\text{p}K_{\text{a}2} = 3.78$) thanks to the aromatic character of its dianion.^{27–29} We considered H_2SQ and its anions, HSQ^- and SQ^{2-} , as promising candidates for co-crystallization with heteroaryl boronic acids in view of several factors: (i) they are planar molecules due to the π -conjugation of the C–C and C–O bonds, (ii) they can act both as hydrogen bond acceptors and donors^{30–33} (with the exception of SQ^{2-}) and (iii) they establish strong charge-assisted or resonance-assisted H-bonds confined to the molecular plane, showing a notable preference for anisotropic molecular assemblies.^{34–37} Co-crystals of the above-mentioned boronic acids with squaric acid were thus obtained, showing the emergence of the boronic acid-squarate dianion synthon. Besides, they possess a zwitterionic character, which was conveniently exploited for the construction of a polymeric ternary co-crystal with 4,4'-bipyridine (bpy).



Scheme 2.4.1 Molecular structure of the chosen building blocks: 4-Pyridinylboronic acid (**1BA**), 3-pyridinylboronic acid (**2BA**), (4-(pyridin-4-yl)phenyl)boronic acid (**3BA**), and squaric acid (H_2SQ).

2.4.2 Experimental

All the reagents were obtained from commercial sources and used as received. All the syntheses were repeated at least two times in order to verify the reproducibility.

Synthesis of [SQ(1BAH)₂]·2H₂O. In a typical procedure, 1 equivalent of squaric acid and 2 equivalents of 4-pyridinylboronic acid were mixed in deionized water. The so-obtained suspension was heated until the dissolution of the insoluble boronic acid was achieved. Upon cooling to room temperature, colourless needle crystals precipitated. Decomposition occurred without melting. For the IR spectrum, see the ESI.

Synthesis of [SQ(2BAH)₂]·H₂O. 3-Pyridinylboronic acid (2 eq.) and squaric acid (1 eq.) were mixed in deionized water, and the suspension was heated until a clear solution was obtained. 4,4'-Bipyridine (1 eq.) was then added and the solution was cooled to room temperature. Upon cooling, yellow crystals precipitated. Decomposition occurred without melting. For the IR spectrum, see the ESI.

Synthesis of [SQ(3BAH)₂]·2H₂O. A suspension of 4-pyridin-4-yl-phenylboronic acid (2 eq.) and squaric acid (1 eq.) in deionized water was heated at reflux temperature. The white precipitate slowly turned yellow. After 30 minutes, the solid was filtered and washed with fresh water. Decomposition occurred without melting. For the IR spectrum, see the ESI.

Crystals of [SQ(3BAH)₂]·2H₂O suitable for SC-XRD analysis were obtained in the presence of 4,4'-bipyridine according to the following procedure: polycrystalline [SQ(3BAH)₂]·2H₂O was suspended in deionized water and 1 equivalent of 4,4'-bipyridine was added. The suspension was heated until a clear solution was obtained. Upon cooling to room temperature, yellow crystals formed. Decomposition occurred without melting. For the IR spectrum, see the ESI.

Synthesis of [SQ(1BAH)₂]·bpy. A suspension of [SQ(1BAH)₂]·2H₂O in deionized water was heated until complete dissolution was achieved. 4,4'-Bipyridine (1 eq.) was then added and the solution was cooled to room

temperature. Yellow crystals precipitated on cooling. Alternatively, [SQ(1BAH)₂]·bpy was obtained by a direct reaction in solution, *i.e.*, weighing the three reactants in a suitable stoichiometric ratio and boiling them to obtain a clear solution that is then left to cool down slowly. M.p. > 350 °C. For the IR spectrum, see the ESI.

Infrared spectroscopy. IR spectra were acquired in the 400–4000 cm⁻¹ range on a Bruker APLHA platinum ATR spectrometer, equipped with a diamond attenuated total reflectance module. See the ESI for the spectra.

X-ray diffraction. Single crystal X-ray diffraction data for [SQ(1BAH)₂]·2H₂O, [SQ(2BAH)₂]·H₂O, [SQ(3BAH)₂]·2H₂O, and [SQ(1BAH)₂]·bpy were collected at room temperature with an Oxford Diffraction X'Calibur diffractometer equipped with a graphite monochromator and a CCD detector. Mo-K α radiation ($\lambda = 0.71073 \text{ \AA}$) was used. The unit cell parameters were determined by means of a 15 frame pre-experiment. The measured intensities were reduced to F^2 and corrected for absorption, Lorentz and polarization effects with CrysAlisPro. The structures were solved with SHELXT³⁸ and refined on full-matrix F^2 by means of the SHELXL package, implemented in the Olex2 software.³⁹ Non-hydrogen atoms were refined anisotropically, while hydrogen atoms were placed in calculated positions using a riding model. O–H and N–H hydrogen atoms were located in the Fourier maps. For [SQ(1BAH)₂]·bpy, a positive residue on the bpy N-atom suggested the presence of a partial hydrogen atom, though both the refinement of the model with the (bpyH₂)²⁺ isomer and with a two-fold partitioning at 0.5 occupancy led to an increase of the R factor; on the other hand, refinement with occupancy fixed at 0.2 for bpy N–H produced a lower R factor (4.63%). Refinement of the occupancies was attempted but led to unacceptable results, probably because the N–H groups sit on a reflection plane. It was thus concluded that proton transfer from [SQ(1BAH)₂] to the bpy moiety is present to a small extent, which roughly equals 20% of the population. The program Mercury⁴⁰ was used to calculate intermolecular interactions and for molecular graphics. Data collection and refinement details are listed in Table ESI-1.

X-ray powder diffraction routine analyses were performed on a PANalytical X'Pert Pro automated diffractometer equipped with an X'Celerator detector in the Bragg–Brentano geometry, using Cu-K α radiation

($\lambda = 1.5418 \text{ \AA}$) without a monochromator in the 2θ range between 3° and 50° (continuous scan mode, step size 0.0167° , counting time 19.685 s, Soller slit 0.04 rad, anti-scatter slit $\frac{1}{2}$, divergence slit $\frac{1}{4}$, 40 mA \times 40 kV). The program Mercury⁴⁰ was used for the calculation of X-ray powder patterns on the basis of single crystal data or retrieved from the CSD. The chemical and structural identity between bulk materials and single crystals was always verified by comparing experimental and calculated powder diffraction patterns. See the ESI for XRPD pattern comparison.

2.4.3 Results and discussion

Boronic acid–squaric acid salt co-crystals

The reaction of squaric acid (H_2SQ) with the three pyridine-appended boronic acid derivatives shown in Scheme 2.4.1 leads to the formation of supramolecular zwitterions of the general formula $[\text{SQ}(\text{BAH})_2] \cdot x\text{H}_2\text{O}$ generated by proton transfer from squaric acid to the pyridine sites and by the formation of strong charge-assisted hydrogen bonds between the B-bound $-\text{OH}$ groups and the squarate oxygen atoms; see Fig. 2.4.1.

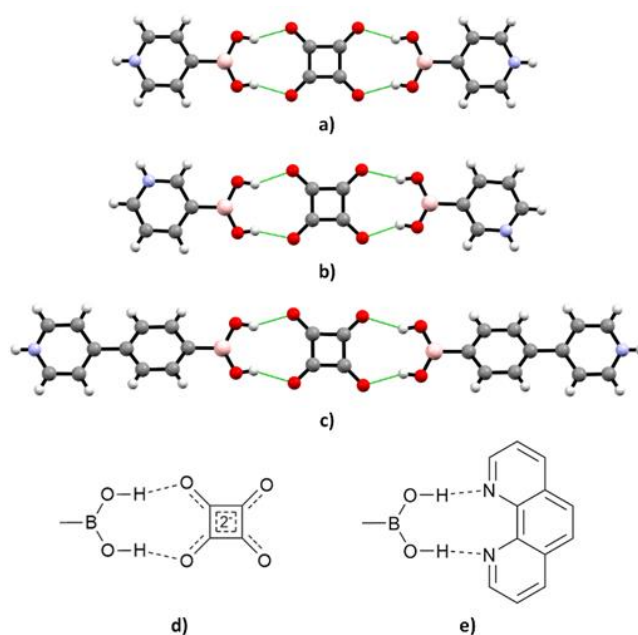


Figure 2.4.1 Recognition pattern of $[\text{SQ}(\text{1BAH})_2] \cdot 2\text{H}_2\text{O}$ (a), $[\text{SQ}(\text{2BAH})_2] \cdot \text{H}_2\text{O}$ (b), and $[\text{SQ}(\text{3BAH})_2] \cdot 2\text{H}_2\text{O}$ (c); schematic comparison of the boronic acid–squarate dianion (d) and boronic acid–phenanthroline (e) synthons.

The C–O distances within the squarate anions [1.251(2)–1.257(2) Å] and the stoichiometry of the products are consistent with the complete deprotonation of squaric acid, so the supramolecular [SQ(BAH)₂] unit is overall neutral, containing two zwitterionic pairs.

In all the products so far characterized, the supramolecular zwitterions are held together by C–O⋯H(O) bonds between the squarate anion and the boronic acid (see Fig. 2.4.1). The H-bond distances are summarized in Table 2.4.1.

Table 2.4.1 Comparison between the H-bond distances of the boronic acid–squarate dianion synthon detected in [SQ(1BAH)₂]·2H₂O, [SQ(2BAH)₂]·H₂O, and [SQ(3BAH)₂]·2H₂O and the mean value of neutral and charge-assisted C–O⋯H, N⋯H and homo-dimeric B–O⋯H bonds extracted from the CSD.

Compound	A⋯O(B) distance (Å)
[SQ(1BAH) ₂]·2H ₂ O	2.673(1)
[SQ(2BAH) ₂]·H ₂ O	2.648(2)
	2.654(2)
	2.680(2)
	2.632(2)
[SQ(3BAH) ₂]·2H ₂ O	2.688(2)
	2.722(2)
O⋯O ^a	2.743(1)
O⋯O ^b	2.667(9)
N⋯O	2.822(78)
Homo-dimeric O⋯O	2.762(47)

^a Neutral hydrogen bond. ^b Charge-assisted hydrogen bond.

The hydrogen atoms of the boronic moiety adopt the *syn,syn*-conformation, which is convenient for the formation of a pair of charge-assisted hydrogen bonds with the squarate O-atoms.

The topology of the nine-membered ring thus formed is equivalent to the boronic acid–phenanthroline synthon,^{22,23,41} except that in the present case, the acceptors are negatively charged O-atoms rather than neutral N-atoms. It is worth stressing that all four C=O groups on the squarate anions are employed in charge-assisted hydrogen bonds; this is possible due to the aromatic character of the squarate dianion and the resulting delocalization of its negative charges.⁴² The H-bond distances are indeed in agreement with the

expected value for a charge-assisted C–O⋯H bond, based on the average values extrapolated from the CSD (see Table 2.4.1).

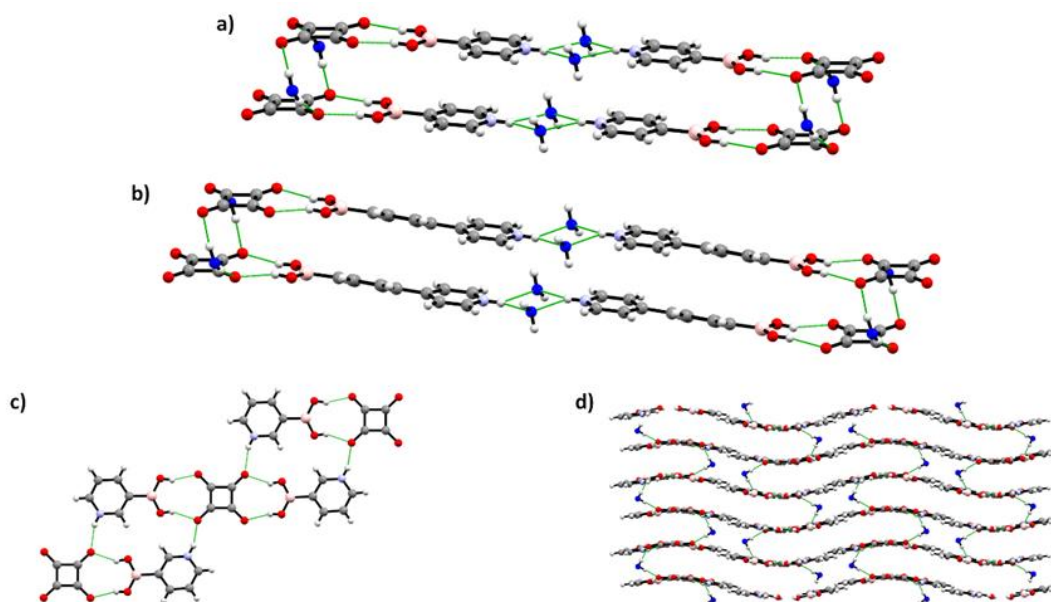


Figure 2.4.2 Packing motifs of [SQ(1BAH)₂]·2H₂O (a), [SQ(3BAH)₂]·2H₂O (b) and [SQ(2BAH)₂]·H₂O (c); three-dimensional arrangement of [SQ(2BAH)₂]·H₂O in a layered structure (d); water molecules depicted in blue for clarity.

Although the zwitterions are essentially linear, they are not entirely flat: in [SQ(1BAH)₂]·2H₂O, the plane containing the squarate dianion is tilted by 5.95° with respect to the plane of the boronic acid. In [SQ(3BAH)₂]·2H₂O, the two planes are tilted by 11.24°. Understandably, the motif is not replicated in the crystal packing of [SQ(2BAH)₂]·H₂O, since the N–H group in the *meta*-position is involved in an H-bond with an adjacent squarate dianion, giving rise to a ladder-like disposition of the [SQ(2BAH)₂] units (see Fig. 2.4.2c). Nevertheless, as was observed by Karle and coworkers,³⁵ the preference of the squaric acid for layered structures irrespective of the hydrogen bond pattern established is confirmed here, in that [SQ(2BAH)₂]·H₂O assembles into wavy layers connected with each other by water molecules (see Fig. 2.4.2d). Indeed, every O-atom of the squarate dianion in [SQ(2BAH)₂]·H₂O is also involved in lateral H-bonds: two are in the O⋯H–N in-layer bonds mentioned above, while the other two are in the out-of-layer O⋯H–O bonds bridging adjacent layers along the glide plane direction. Meanwhile, the role of the water bridges in [SQ(1BAH)₂]·2H₂O and [SQ(3BAH)₂]·2H₂O is two-fold: on the one hand, the O-atoms can link together the protonated pyridine moieties by forming

bifurcated N–H···O bonds, $d_{N...o} = 2.927 \text{ \AA}$ in $[\text{SQ}(\mathbf{3BAH})_2] \cdot 2\text{H}_2\text{O}$, and $2.866(2)$ and $2.941(2) \text{ \AA}$ in $[\text{SQ}(\mathbf{1BAH})_2] \cdot 2\text{H}_2\text{O}$. On the other hand, they provide interstacked hydrogen bonds with the water hydrogens lying above and below the squarate anions (see Fig. 2.4.2a and b).

Co-crystal of the supramolecular zwitterions with bipyridine

Intrigued by the role played by the bridging water molecules, we wondered whether other hydrogen bonding acceptor species could have replaced them. Moreover, in spite of the different lengths of the aromatic moiety, $[\text{SQ}(\mathbf{1BAH})_2] \cdot 2\text{H}_2\text{O}$ and $[\text{SQ}(\mathbf{2BAH})_2] \cdot 2\text{H}_2\text{O}$ replicate the same motif, with the water of crystallization promoting the linear arrangement of the $[\text{SQ}(\mathbf{BAH})_2]$ units.

Prompted by these observations, we explored the possibility of substituting water molecules with a linear bifunctional H-bond acceptor. An N-donor molecule such as 4,4'-bipyridine (bpy) was selected for this purpose, in consideration of its affinity for N–H hydrogen bond donors. Moreover, the competition with the squarate dianion as the H-bond acceptor would prove useful in the evaluation of the robustness of the boronic acid–squarate synthon.

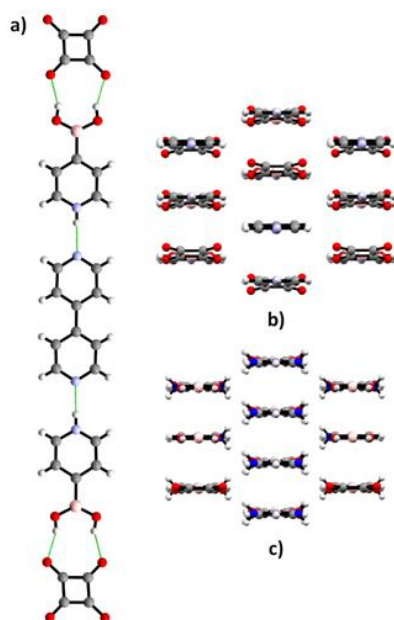


Figure 2.4.3 (a) Hydrogen bond pattern of the ternary co-crystal $[\text{SQ}(\mathbf{1BAH})_2] \cdot \text{bpy}$, and packing diagrams of $[\text{SQ}(\mathbf{1BAH})_2] \cdot \text{bpy}$ (b) and $[\text{SQ}(\mathbf{1BAH})_2] \cdot 2\text{H}_2\text{O}$ (c) showing the direction of the charge assisted-hydrogen bonded chains and columnar stacking, respectively.

The reaction of [SQ(1BAH)₂] · 2H₂O with bpy yielded a co-crystal with the stoichiometry 1 : 1, *i.e.* [SQ(1BAH)₂] · bpy. Therefore, a three-component crystal is formed where the bipyridine establishes N–H···N bonds with the pyridinium termini [$d_{N...N} = 2.748(3)$ Å]. No water of crystallization is present, whereas the preference for a linear assembly is maintained. Infinite chains are formed by virtue of hydrogen bonds, which display a similar columnar packing to that of the precursor, [SQ(1BAH)₂] · 2H₂O, see Fig. 2.4.3.

On the other hand, our attempts to co-crystallize [SQ(3BAH)₂] · 2H₂O and bpy resulted invariably in the concomitant crystallization of the two components. Similarly, the crystals of [SQ(2BAH)₂] · H₂O were afforded by the reaction of squaric acid and 3-pyridinylboronic acid in the presence of a stoichiometric amount of bpy, where they could not be obtained by the direct reaction of the two components (see the Experimental section). Therefore, it seems that in those cases the 4,4'-bipyridine acts as a solubility-enhancer of the rather insoluble boronic acids and their salts with squaric acid. The reason could be the competition between bpy and water molecules in the interaction with the pyridinium functions, though apparently, the lateral N–H···O bonds in [SQ(2BAH)₂] · H₂O are much stronger than those in [SQ(1BAH)₂] · 2H₂O, so they are not replaced by bpy. It is noteworthy that direct interaction between the bpy N-donor and squaric acid has never been observed before. The reported pK_a of 4-pyridinylboronic acid is 3.6 (ref. 43) so, in principle, it should be replaced by the stronger base bpy ($pK_a = 4.8$).⁴⁴ Moreover, in [SQ(1BAH)₂] · bpy, the Fourier maps suggest that the positively charged protons are localized mainly on the [SQ(1BAH)₂] N-atoms, with a smaller population on the bpy N-atoms (see the ESI). These observations suggest that the boronic acid–squarate synthon is quite robust, probably owing to the strength of the cooperative O–H···O bonds, and might be transferable to other boronic acids with proton acceptor substituents.

2.4.4 Conclusions

In this work, we have reported the preparation and full structural characterization by X-ray diffraction methods of three novel salt co-crystals obtained by the reaction of the oxocarbon acid squaric acid (H₂SQ) with a series of boronic acid derivatives, namely 4-pyridinylboronic acid (1BA), 3-pyridinylboronic acid (2BA), and (4-(pyridin-4-yl)phenyl)boronic acid (3BA).

We have found that all the boronic acid derivatives react with squaric acid in a similar way producing the following crystalline materials: [SQ(1BAH)₂] · 2H₂O, [SQ(2BAH)₂] · H₂O, and [SQ(3BAH)₂] · 2H₂O.

A common feature is the presence of the same structural unit [SQ(BAH)₂], which is held by four pairs of charge-assisted hydrogen bonds between the squarate O-atoms and boronic acid generating a nine-membered ring equivalent to the known boronic acid–phenanthroline synthon.^{22,23,41} Although the three systems can be adequately described as salts formed between the squarate dianion and the boronic acid cations, it is stimulating to regard these systems as supramolecular zwitterions whereby the squaric acid protons are transferred to the two pyridinyl N-termini yielding a neutral supramolecular aggregate.

Additionally, we have explored the possibility of obtaining ternary crystal phases by replacing the water molecules with a linear bifunctional H-bond acceptor such as 4,4'-bipyridine (bpy).

All the attempts to co-crystallize [SQ(2BAH)₂] · H₂O or [SQ(3BAH)₂] · 2H₂O with bpy were fruitless and led to a mixture of the starting reactants.

It is useful to point out that in no case were direct interactions between the N-donor (bpy) and squaric acid observed, providing indirect evidence about the robustness of the boronic acid–squarate synthon and suggesting that it might be extended to other boronic acids bearing proton acceptor groups.

Finally, we succeeded in growing a three-component crystal upon the reaction of bpy with [SQ(1BAH)₂] · 2H₂O, or by a direct reaction with suitable stoichiometric amounts of H₂SQ and 1BA. In the ternary co-crystal, the same supramolecular unit [SQ(BAH)₂] is still present with the bipyridine molecule establishing N–H···N bonds with the pyridinium termini.

Work is in progress to further investigate the robustness of the boronic acid–squarate synthon and to design novel ternary co-crystals.

References

- (1) D. Braga, F. Grepioni, L. Maini and S. D'Agostino, *Eur. J. Inorg. Chem.*, **2018**, 2018, 3597–3605.
- (2) G. R. Desiraju, *Angew. Chemie Int. Ed. English*, **1995**, 34, 2311–2327.
- (3) D. Braga, F. Grepioni, L. Maini and S. D'Agostino, *IUCrJ*, **2017**, 4, 369–379.
- (4) M. C. Etter, *Acc. Chem. Res.*, **1990**, 23, 120–126.
- (5) D. Braga, S. d'Agostino and F. Grepioni, *Organometallics*, **2012**, 31, 1688–1695.
- (6) N. Miyaura and A. Suzuki, *Chem. Rev.*, **1995**, 95, 2457–2483.

- (7) D. G. Hall, in *Boronic Acids: Preparation and Applications in Organic Synthesis, Medicine and Materials, 1&2, Second Edition*, Wiley-VCH Verlag GmbH & Co. KGaA, Weinheim, Germany, **2011**, pp. 1–133.
- (8) R. Nishiyabu, Y. Kubo, T. D. James and J. S. Fossey, *Chem. Commun.*, **2011**, 47, 1106.
- (9) H. Zheng and D. G. Hall, *Aldrichimica Acta*, **2014**, 47, 41–51.
- (10) R. Nishiyabu, Y. Kubo, T. D. James and J. S. Fossey, *Chem. Commun.*, **2011**, 47, 1124–1150.
- (11) Y. Kanekiyo and S. Shinkai, in *Supramolecular Chemistry of Boronic Acids*, The Royal Society of Chemistry, **2015**, pp. 1–43.
- (12) X. Sun and T. D. James, *Chem. Rev.*, **2015**, 115, 8001–8037.
- (13) H. Furukawa and O. M. Yaghi, *J. Am. Chem. Soc.*, **2009**, 131, 8875–8883.
- (14) J. H. Fournier, T. Maris, J. D. Wuest, W. Guo and E. Galoppini, *J. Am. Chem. Soc.*, **2003**, 125, 1002–1006.
- (15) N. Luisier, K. Bally, R. Scopelliti, F. T. Fadaei, K. Schenk, P. Pattison, E. Solari and K. Severin, *Cryst. Growth Des.*, **2016**, 16, 6600–6604.
- (16) L. Fornasari, R. Mazzaro, E. Boanini, S. D'Agostino, G. Bergamini, F. Grepioni and D. Braga, *Cryst. Growth Des.*, **2018**, 18, 7259–7263.
- (17) L. Fornasari, S. D'Agostino and D. Braga, *European J. Org. Chem.*, **2019**, 2019, 1574–1582.
- (18) D. Salazar-Mendoza, J. Cruz-Huerta, H. Höpfl, I. F. Hernández-Ahuactzi and M. Sanchez, *Cryst. Growth Des.*, **2013**, 13, 2441–2454.
- (19) J. J. Campos-Gaxiola, A. Vega-Paz, P. Román-Bravo, H. Höpfl and M. Sánchez-Vázquez, *Cryst. Growth Des.*, **2010**, 10, 3182–3190.
- (20) Y. Yahsi, E. Gungor and H. Kara, *Cryst. Growth Des.*, **2015**, 15, 2652–2660.
- (21) H. Kara, C. J. Adams, A. G. Orpen and T. J. Podesta, *New J. Chem.*, **2006**, 30, 1461.
- (22) S. Varughese, S. B. Sinha and G. R. Desiraju, *Sci. China Chem.*, **2011**, 54, 1909–1919.
- (23) I. Georgiou, S. Kervyn, A. Rossignon, F. De Leo, J. Wouters, G. Bruylants and D. Bonifazi, *J. Am. Chem. Soc.*, **2017**, 139, 2710–2727.
- (24) G. Campillo-Alvarado, A. D. Brannan, D. C. Swenson and L. R. MacGillivray, *Org. Lett.*, **2018**, 20, 5490–5492.
- (25) G. Campillo-Alvarado, C. A. Staudt, M. J. Bak and L. R. MacGillivray, *CrystEngComm*, **2017**, 19, 2983–2986.
- (26) J. J. Campos-Gaxiola, B. A. García-Grajeda, I. F. Hernández-Ahuactzi, J. A. Guerrero-Álvarez, H. Höpfl and A. Cruz-Enríquez, *CrystEngComm*, **2017**, 19, 3760–3775.
- (27) S. Cohen, J. R. Lacher and J. D. Park, *J. Am. Chem. Soc.*, **1959**, 81, 3480–3480.
- (28) R. West, *Isr. J. Chem.*, **1980**, 20, 300–307.
- (29) G. Seitz and P. Imming, *Chem. Rev.*, **1992**, 92, 1227–1260.
- (30) V. Bertolasi, P. Gilli, V. Ferretti and G. Gilli, *Acta Crystallogr. Sect. B Struct. Sci.*, **2001**, 57, 591–598.
- (31) G. Gilli, V. Bertolasi, P. Gilli and V. Ferretti, *Acta Crystallogr. Sect. B Struct. Sci.*, **2001**, 57, 859–865.
- (32) M. Aniola, Z. Dega-Szafran, A. Katrusiak and M. Szafran, *New J. Chem.*, **2014**, 38, 3556–3568.
- (33) M.-D. Şerb, I. Kalf and U. Englert, *CrystEngComm*, **2014**, 16, 10631–10639.
- (34) G. Gilli, V. Bertolasi, V. Ferretti and P. Gilli, *Acta Crystallogr. Sect. B*, **1993**, 49, 564–576.
- (35) I. L. Karle, D. Ranganathan and V. Haridas, *J. Am. Chem. Soc.*, **1996**, 118, 7128–7133.
- (36) D. Braga and F. Grepioni, *Chem. Commun.*, **1998**, 0, 911–912.
- (37) A. Caneschi, L. Maini, L. Prodi, D. Braga, R. Sessoli and F. Grepioni, *Chem. - A Eur. J.*, **2005**, 6, 1310–1317.
- (38) G. M. Sheldrick, *Acta Crystallogr. Sect. A Found. Crystallogr.*, **2015**, 71, 3–8.
- (39) O. V Dolomanov, L. J. Bourhis, R. J. Gildea, J. A. K. Howard and H. Puschmann, *J. Appl. Crystallogr.*, **2009**, 42, 339–341.
- (40) C. R. Groom, I. J. Bruno, M. P. Lightfoot, S. C. Ward and IUCr, *Acta Crystallogr. Sect. B Struct. Sci. Cryst. Eng. Mater.*, **2016**, 72, 171–179.
- (41) M. Talwelkar and V. R. Pedireddi, *Tetrahedron Lett.*, **2010**, 51, 6901–6905.
- (42) R. West and D. L. Powell, *J. Am. Chem. Soc.*, **1963**, 85, 2577–2579.
- (43) F. C. Fischer and E. Havinga, *Recl. des Trav. Chim. des Pays-Bas*, **2010**, 93, 21–24.

(44) P. Krumholz, *J. Am. Chem. Soc.*, **1951**, 73, 3487–3492.

Chapter 3

Crystal Engineering and Solid-State Molecular Motion

3.1 Overview

Solid state chemistry has greatly evolved in the last decades: it was long established that crystals, for example, possess translational and librational mobility and are reactive,¹⁻⁵ exactly like the liquid and gaseous states of matter. Topochemical reactions,^{6,7} mechanochemical phenomena^{8,9} and polymorphism (*vide supra*), just to name a few, are proofs that crystals are not “*chemical cemeteries*”.⁵ Nevertheless, it is still a widespread misconception that crystals are static entities and atomic and molecular motion is a nuisance that complicates their characterisation, rather than a valuable source of chemical information and a tool for imparting specific functions.

An emblematic case is provided by plastic crystals. They have been known for almost a century, the term “plastic crystal” was first introduced by Timmermans in 1938 in view of the malleable quality of the solids,¹⁰ a consequence of the high degree of orientational motion that hampers the close packing of molecules. However, it was not until recently that it was demonstrated that plastic crystals have unique properties of ion conduction,^{11,12} ferroelectricity^{13,14} and caloric effect,^{15,16} that could potentially result in technological breakthroughs in the development of solid-state batteries, refrigerators and organic electronics.

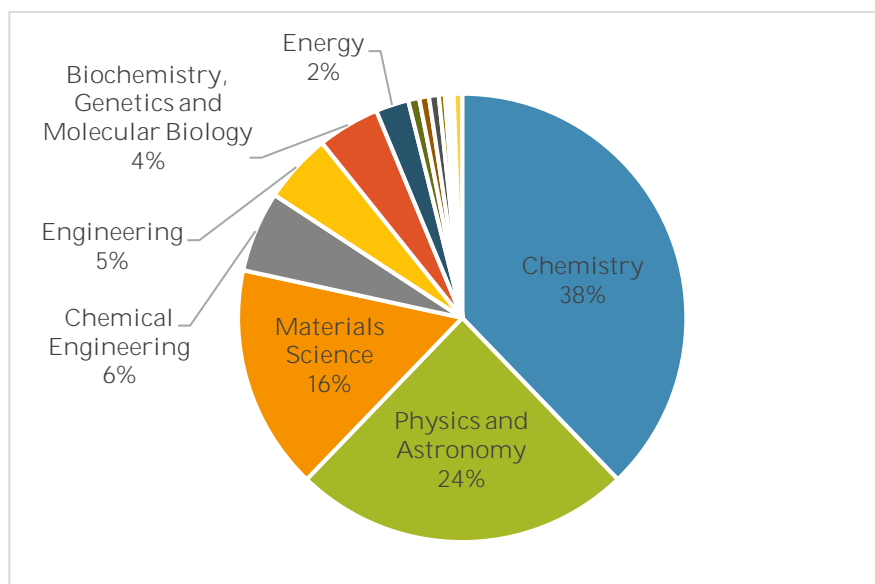


Figure 3.1.1 Number of citations of ref. 17 by subject; source www.scopus.com

Figure 3.1.1 shows that the citations of the paper “Plastic crystals: A historical review” written by Timmermans in 1961¹⁷ are well distributed between chemistry, physics and materials science; furthermore, they touch the fields of engineering, energy and biology. The study of dynamic phenomena in the solid state is an interdisciplinary area of research that covers a vast range of theoretical and applicative topics. As it is stimulating from an intellectual perspective, this could also generate ambiguities and oversights: it is a field of research that escapes strict categorisations (with the notable exception of the efforts made by Garcia-Garibay in defining the field of *amphidynamic crystals*^{18,19}) and the terminology can be used in a confusing manner or not used at all. The words “rotor”, “rotator” and “rotary” are used for referring to the motion of phenylene substituents as well as whole molecules undergoing spherical reorientations around multiple axes. On the other hand, terms like “molecular rotation”, “molecular motion”, “molecular process”, “molecular dynamic”, “dynamical process”, “dynamical disorder” are often alternatively employed to describe systems that are, as a matter of fact, very similar.

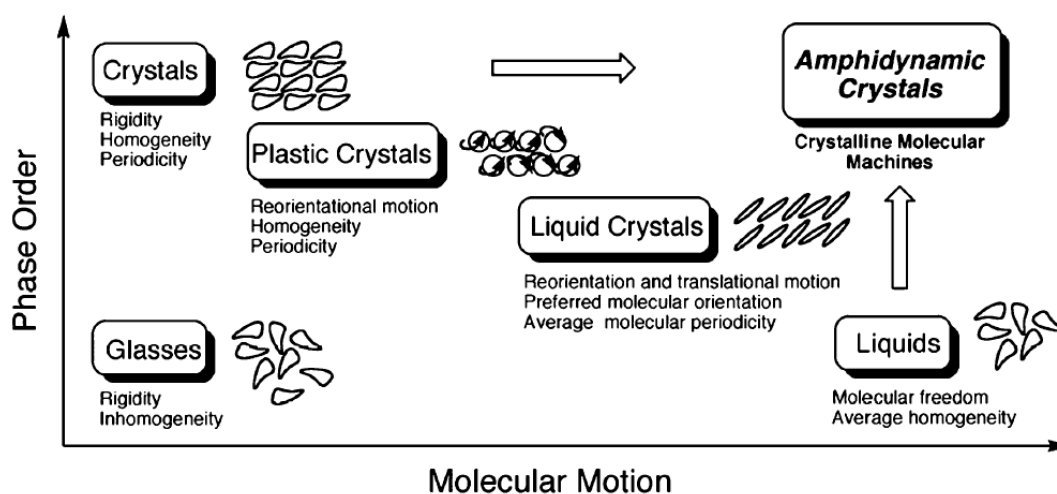


Figure 3.1.2 Phase order vs. molecular motion (reproduced from ref. 18)

In qualitative terms, it is useful to schematise an inverse relationship between phase order and molecular motion, that is effectively illustrated in the diagram proposed by Garcia-Garibay¹⁸ (Figure 3.1.2). Liquids are in the bottom right, having high mobility and no long-range order, while a typical crystal is in the top left since it has long-range order but limited degrees of freedom. Liquid crystals and plastic crystals are on the top left/bottom right diagonal, as they represent a compromise between the phase order of crystals

and the mobility of liquids; for this reason, they are usually categorised as *soft matter*.²⁰ Finally, glasses are in the bottom left, since they can be seen as “frozen” liquids, and amphidynamic crystals are in the top right, conserving both long-range order and fast motion.

The present work focuses on the study of orientational motion in crystalline solids and the possibility of “engineer” it by means of the principles of crystal engineering (*vide supra*).

3.1.1 Orientational motion in crystals

Molecules in crystals can undergo different types of orientational motion. In the simplest case, the motion is a rotation around a fixed axis: some examples are the rotation of a substituent around a covalent single bond, such as a phenylene or a methyl,²¹⁻²⁵ or a symmetry axis, such as the rotation of benzene around its six-fold axis.²⁶⁻²⁸ The rotation is otherwise around a fixed point if it is the composition of multiple rotations around different axes; this is the case, for example, of the isotropic rotations in crystals of fullerene²⁹⁻³¹ or the pedal motion.³²

The general equation to describe a one-dimensional system has the form:³³

$$I \frac{d^2\theta}{dt^2} = -\frac{\partial V_{net}}{\partial \theta} - \eta \frac{d\theta}{dt} + \xi(T, t)$$

where a rigid body (*rotator*) performs a rotation around an axle with torsional angle θ and moment of inertia I . The V_{net} potential of the first term in the right-hand side accounts for all the static or time-dependent interactions of the rotator with the external world. It comprises an internal rotational potential (W), that is the potential energy *versus* angle for turning the rotator around the axis, the interaction energy between rotators and the interaction between rotators and an external driving field U . In molecular solids the distinction between W and the rotator-rotator interaction is often blurred, the two contributions can be thought of as a generalised crystal potential. In most cases U is zero, as only random thermal motions are present, however, it is useful to introduce the notion of driven motion. One of the main challenges in the engineering of motion at the molecular scale is the design of systems where the moving parts possess a permanent dipole; in such cases, the motion could be ideally harnessed by an external electric field, in order to extract work from the system.

The second term represents frictional forces. The main contribution to friction is the loss of energy of the rotator to other modes within the crystal such as vibrations. It should be noted that the first two terms have negative sign, indicating that in general the effect is that of reducing the angular velocity; nevertheless, there are cases in which the frequency of rotation exhibited in solids is higher than in solution.³⁰ Finally, ξ represent the stochastic torque induced by thermal fluctuations of the system.

The motion observed in molecular solids is almost always ascribable to hindered random thermal motion (or Brownian). The system can be described by a simple thermodynamic model consisting of multiple-minima potential energy function: the rotation consists of librations within one well with occasional hops between different minima activated by thermal energy, with equal probability on each side. This behaviour agrees well with an Arrhenius-type model in the form:

$$k_{rot} = k_0 \exp(-E_a/kT)$$

where k_{rot} and k_0 are the frequency of rotation and oscillation respectively and E_a is the potential energy barrier.¹⁹

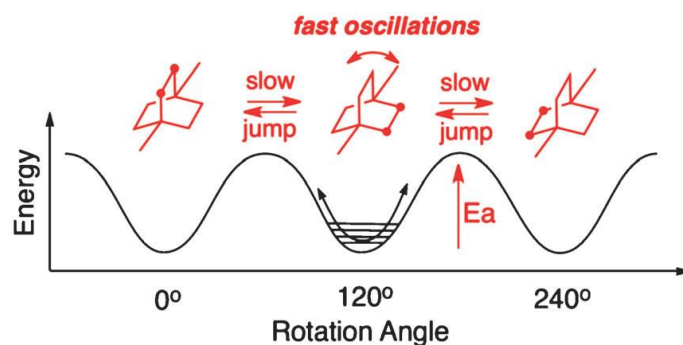


Figure 3.1.3. Scheme of the potential energy for a three-fold symmetric hindered random thermal rotation (reproduced from ref. 19).

The number of minima usually reflects the symmetry of the system;³⁴ for example, a phenyl ring performing 180° hops around the C1-C4 axis is expected to have two minima in the potential energy. However, crystal symmetry must be taken into account: the number and magnitude of the minima depend on the position of the molecules within the lattice and, if two or more symmetrically independent components are present, also on how the point symmetries are related to the space group.³⁵ As a rule of thumb, though, the higher the order of the rotation, the lower the internal potential W , *i.e.* the lower the potential barrier for the rotation.

As the system approaches the plastically crystalline state, the degrees of freedom increase and W decreases. In this limit the thermal content of the system, kT , is much higher than the potential barriers; the motion becomes almost unhindered and, if a snapshot could be taken at a given time, the rotators would display random orientation.

Finally, NMR and XRD are most commonly employed to study rotational dynamics in crystals by virtue of their complementarity. A solid-state NMR experiment gives information on the local structure and the dynamic changes it undergoes within the timescale of the technique.³⁶ On the other hand, crystallographic techniques give information on the extended structure, the atomic positions and their average displacement from the mean.^{2,5} Citing Dunitz: “In a sense, one can say that spectroscopy sees the rate at which molecules cross the barrier, while diffraction sees the bottom of the potential well”.¹

3.1.2 Design principles

The strategies for the design of molecular crystals possessing components in rapid orientational motion can be summarised as follows:

1. The creation of free space around the rotator
2. The use of volume-conserving shapes
3. The “use” of geared motion

The most relevant contribution to the V_{net} potential introduced in the previous paragraph comes from steric hindrance. Steric repulsion is intrinsically local (see paragraph 1.1.1), therefore it is often insufficient to describe free space in terms of the Kitaigorodskii packing coefficient,³⁷ as the space proximal to the rotator must be considered. The design of strictly low-density structures works well in the case of porous solids,³⁸ however it somewhat limits the scope of action, since in general rigid frameworks with linear spacers are required, as well as small rotators such as phenylene rings.

A common strategy is the use of bulky groups coupled to smaller units so that a sort of steric shield is created around the envisioned rotator.¹⁹ Moreover, it has been observed that flexibility plays a central role: the internal motion in

densely-packed solids depends on the ability of the crystal structure to distort and accommodate the rotation through the creation of transient voids.³⁹

Point 2 is connected to the dependence of the potential barrier for the rotation from the symmetry of the system. In very general terms, molecules possessing high-order rotation axes are expected to have lower activation energy. For example, a large number of plastic crystals are formed by molecules of globular shape.

Correlated motion is a mechanism observed in closed-packed crystals that allows the effective minimisation of the steric hindrance without reducing the entropy of the system. It represents the main contribution to the rotator-rotator interaction and is in fact connected to the concept of crystal flexibility discussed for point 1. It should be noted, however, that limited control can be exerted *a priori* over this feature since the intermeshing of moving parts is often a consequence of subtle optimisations occurring in the self-assembly process.

References

- (1) Dunitz, J. D.; Maverick, E. F.; Trueblood, K. N. Atomic Motions in Molecular Crystals from Diffraction Measurements. *Angewandte Chemie International Edition in English*. John Wiley & Sons, Ltd July 1, **1988**, pp 880–895.
- (2) Bürgi, H. B. Motion and Disorder in Crystal Structure Analysis: Measuring and Distinguishing Them. *Annu. Rev. Phys. Chem.* **2000**, *51* (1), 275–296.
- (3) Gavezzotti, A.; Simonetta, M. Crystal Chemistry in Organic Solids. *Chem. Rev.* **1982**, *82* (1), 1–13.
- (4) Braga, D. Dynamical Processes in Crystalline Organometallic Complexes. *Chem. Rev.* **1992**, *92* (4), 633–665.
- (5) Dunitz, J. D.; Schomaker, V.; Trueblood, K. N. Interpretation of Atomic Displacement Parameters from Diffraction Studies of Crystals. *Journal of Physical Chemistry*. American Chemical Society February **1988**, pp 856–867.
- (6) Ramamurthy, V.; Venkatesan, K. Photochemical Reactions of Organic Crystals. *Chem. Rev.* **1987**, *87* (2), 433–481.
- (7) Schmidt, G. M. J. Photodimerization in the Solid State. *Pure Appl. Chem.* **1971**, *27* (4), 647–678.
- (8) James, S. L.; Adams, C. J.; Bolm, C.; Braga, D.; Collier, P.; Friščić, T.; Grepioni, F.; Harris, K. D. M.; Hyett, G.; Jones, W.; et al. Mechanochemistry: Opportunities for New and Cleaner Synthesis. *Chem. Soc. Rev.* **2012**, *41* (1), 413–447.
- (9) Takacs, L. The Historical Development of Mechanochemistry. *Chem. Soc. Rev.* **2013**, *42* (18), 7649.
- (10) Timmermans, J. Un Nouvel État Mésomorphe Les Cristaux Organiques Plastiques. *J. Chim. Phys.* **1938**, *35*, 331–344.
- (11) MacFarlane, D. R.; Huang, J.; Forsyth, M. Lithium-Doped Plastic Crystal Electrolytes Exhibiting Fast Ion Conduction for Secondary Batteries. *Nature* **1999**, *402* (6763), 792–794.
- (12) Pringle, J. M.; Howlett, P. C.; MacFarlane, D. R.; Forsyth, M. Organic Ionic Plastic Crystals: Recent Advances. *J. Mater. Chem.* **2010**, *20* (11), 2056.

- (13) Harada, J.; Shimojo, T.; Oyamaguchi, H.; Hasegawa, H.; Takahashi, Y.; Satomi, K.; Suzuki, Y.; Kawamata, J.; Inabe, T. Directionally Tunable and Mechanically Deformable Ferroelectric Crystals from Rotating Polar Globular Ionic Molecules. *Nat. Chem.* **2016**, *8* (10), 946–952.
- (14) Li, P. F.; Tang, Y. Y.; Wang, Z. X.; Ye, H. Y.; You, Y. M.; Xiong, R. G. Anomalously Rotary Polarization Discovered in Homochiral Organic Ferroelectrics. *Nat. Commun.* **2016**, *7*, 1–9.
- (15) Li, B.; Kawakita, Y.; Ohira-Kawamura, S.; Sugahara, T.; Wang, H.; Wang, J.; Chen, Y.; Kawaguchi, S. I.; Kawaguchi, S.; Ohara, K.; et al. Colossal Barocaloric Effects in Plastic Crystals. *Nature* **2019**, *567* (7749), 506–510.
- (16) Lloveras, P.; Aznar, A.; Barrio, M.; Negrier, P.; Popescu, C.; Planes, A.; Mañosa, L.; Stern-Taulats, E.; Avramenko, A.; Mathur, N. D.; et al. Colossal Barocaloric Effects near Room Temperature in Plastic Crystals of Neopentylglycol. *Nat. Commun.* **2019**, *10* (1), 1803.
- (17) Timmermans, J. Plastic Crystals: A Historical Review. *J. Phys. Chem. Solids* **1961**, *18* (1), 1–8.
- (18) Karlen, S. D.; Garcia-Garibay, M. A. Amphidynamic Crystals: Structural Blueprints for Molecular Machines. In *Molecular Machines*; Springer-Verlag: Berlin/Heidelberg, 2005; Vol. 262, pp 179–227.
- (19) Vogelsberg, C. S.; Garcia-Garibay, M. A. Crystalline Molecular Machines: Function, Phase Order, Dimensionality, and Composition. *Chem. Soc. Rev.* **2012**, *41* (5), 1892–1910.
- (20) *Soft Matter Physics: An Introduction*; Kleman, M., Lavrentovich, O. D., Eds.; Partially Ordered Systems; Springer New York: New York, NY, 2004.
- (21) Durig, J. R.; Craven, S. M.; Mulligan, J. H.; Hawley, C. W.; Bragin, J. Low Frequency Modes in Molecular Crystals. XIX.* Methyl Torsions and Barriers to Internal Rotation of Some Three Top Molecules with C₃ Symmetry. *J. Chem. Phys.* **1973**, *58* (4), 1281–1291.
- (22) Riddell, F. G.; Arumugam, S.; Anderson, J. E. Restricted C-C Bond Rotation in a Solid Measured by Solid State NMR Spectroscopy. *J. Chem. Soc. Chem. Commun.* **1991**, *0* (21), 1525–1527.
- (23) Riddell, F. G.; Rogerson, M. Intramolecular Motions in a Series of Crystalline Benzylammonium Bromides and Dibenzylamines Studied by CP/MAS NMR. *J. Chem. Soc. Perkin Trans. 2* **1996**, *4* (4), 493–504.
- (24) Hiyaama, Y.; Silvertson, J. V.; Torchia, D. A.; Gerig, J. T.; Hammond, S. J. Molecular Structure and Dynamics of Crystalline P-Fluoro-D,L-Phenylalanine. A Combined X-Ray/NMR Investigation. *J. Am. Chem. Soc.* **1986**, *108* (10), 2715–2723.
- (25) Twyman, J. M.; Dobson, C. M. Aromatic Ring Dynamics in Crystalline Penicillins from Variable Temperature ¹³C Cross-Polarisation Magic-Angle-Spinning n.m.R. *J. Chem. Soc. Chem. Commun.* **1988**, No. 12, 786–788.
- (26) Andrew, E. R. Molecular Motion in Certain Solid Hydrocarbons. *J. Chem. Phys.* **1950**, *18* (5), 607–618.
- (27) Andrew, E. R. A Nuclear Magnetic Resonance Investigation of Three Solid Benzenes. *Proc. R. Soc. London. Ser. A. Math. Phys. Sci.* **1953**, *218* (1135), 537–552.
- (28) Anderson, J. E. NMR Spin—Lattice Relaxation in Solid Solutions of C₆H₆ and C₆D₆: Evidence for Concerted Motions by Adjacent Molecules. *J. Chem. Phys.* **1965**, *43* (10), 3575–3579.
- (29) Yannoni, C. S.; Johnson, R. D.; Meijer, G.; Bethune, D. S.; Salem, J. R. ¹³C NMR Study of the C₆₀ Cluster in the Solid State: Molecular Motion and Carbon Chemical Shift Anisotropy. *J. Phys. Chem.* **1991**, *95* (1), 9–10.
- (30) JOHNSON, R. D.; YANNONI, C. S.; DORN, H. C.; SALEM, J. R.; BETHUNE, D. S. C₆₀ Rotation in the Solid State: Dynamics of a Faceted Spherical Top. *Science* (80-.). **1992**, *255* (5049), 1235–1238.
- (31) Tycko, R.; Dabbagh, G.; Fleming, R. M.; Haddon, R. C.; Makhija, A. V.; Zahurak, S. M. Molecular Dynamics and the Phase Transition in Solid C₆₀. *Phys. Rev. Lett.* **1991**, *67* (14), 1886–1889.
- (32) Harada, J.; Ogawa, K. Pedal Motion in Crystals. *Chemical Society Reviews.* 2009, pp 2244–2252.
- (33) Kottas, G. S.; Clarke, L. I.; Horinek, D.; Michl, J. Artificial Molecular Rotors. *Chem. Rev.* **2005**, *105* (4), 1281–1376.

- (34) Karlen, S. D.; Reyes, H.; Taylor, R. E.; Khan, S. I.; Hawthorne, M. F.; Garcia-Garibay, M. A. Symmetry and Dynamics of Molecular Rotors in Amphidynamic Molecular Crystals. *Proc. Natl. Acad. Sci.* **2010**, *107* (34), 14973–14977.
- (35) Islamov, D. R.; Shtyrlin, V. G.; Serov, N. Y.; Fedyanin, I. V.; Lyssenko, K. A. Symmetry Influence on the Rotation of Molecules in Crystals. *Cryst. Growth Des.* **2017**, *17* (9), 4703–4709.
- (36) Böhmer, R.; Diezemann, G.; Hinze, G.; Rössler, E. Dynamics of Supercooled Liquids and Glassy Solids. *Prog. Nucl. Magn. Reson. Spectrosc.* **2001**, *39* (3), 191–267.
- (37) Kitaigorodskii, A. I. *Organic Chemical Crystallography*; Consultants Bureau: New York, 1961.
- (38) Comotti, A.; Bracco, S.; Sozzani, P. Molecular Rotors Built in Porous Materials. *Acc. Chem. Res.* **2016**, *49* (9), 1701–1710.
- (39) Howe, M. E.; Garcia-Garibay, M. A. The Roles of Intrinsic Barriers and Crystal Fluidity in Determining the Dynamics of Crystalline Molecular Rotors and Molecular Machines. *J. Org. Chem.* **2019**, *84* (16), 9835–9849.

3.2 Precessional Motion in Crystalline Solid Solutions of Ionic Rotors

Reproduced with permission from [d'Agostino, S.; Fornasari, L.; Grepioni, F.; Braga, D.; Rossi, F.; Chierotti, M. R.; Gobetto, R. Precessional Motion in Crystalline Solid Solutions of Ionic Rotors. *Chem. - A Eur. J.* **2018**, *24* (56), 15059–15066.] Copyright [2019] John Wiley and Sons. <https://rdcu.be/bVy5v>

3.2.1 Introduction

Dynamic processes, such as rotation and vibration of molecules within crystals, have long attracted the attention of researchers. Partly because dynamical processes taking place in the crystalline state undermine the popular “static” perception of a crystal, and partly, and more importantly, because the understanding, control, and exploitation of such movements can give access to new properties in functional materials. For example, rotation of molecules in crystals has been recently investigated for thermal modulation of birefringence,¹ nonlinear optic properties,² switchable ferroelectrics,^{3,4} gas and vapour sensors,^{5,6} and dielectric constant modulation.³

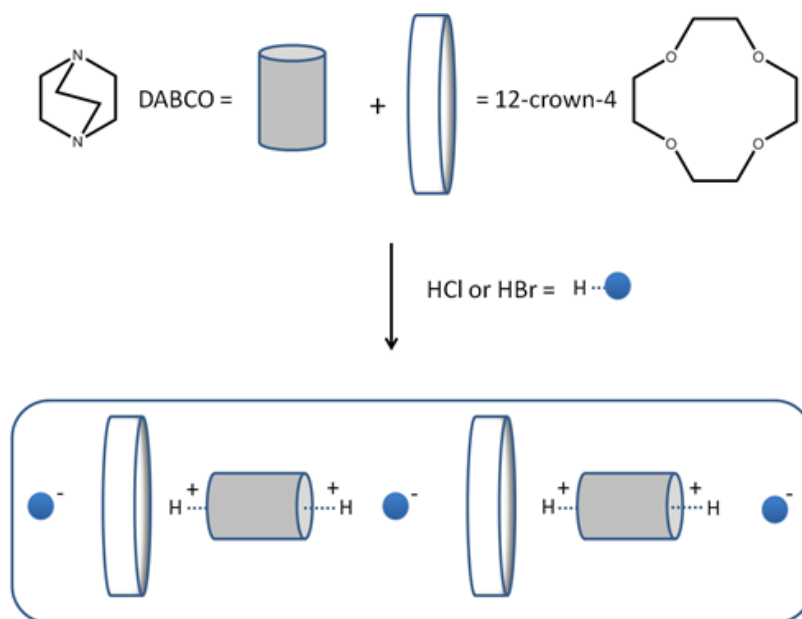
Important factors responsible for dynamic processes of a given fragment (or molecule) within a crystalline material are molecular shape, and nature of the functional groups on the surface. Molecules with protruding and/or “interacting” groups (e.g., hydrogen bonding) tend to be more easily “locked in place” by the surrounding molecules than molecules with approximate flat, spherical or cylindrical shape.⁷ These factors also dictate the potential energy profile associated with the motion, which, in the case of flat and cylindrical molecules, will show minima every $(2\pi/n)$, corresponding to the periodicity n of the idealized symmetry axis of the fragment.^{8,9} Other factors will be the strength and type of bond used to anchor the rotating unit to the stator,¹⁰ and the steric hindrance around the fragment involved; namely the constraints deriving from close packing, which can forbid, or limit significantly, the motional freedom. Temperature however, can play a fundamental role, as constraints imposed by the packing can be loosened by an increase in temperature.⁸ Therefore the ability to combine type and strength of the interactions around the chosen molecular fragment is crucial for a successful design of materials with “tunable” dynamic processes. To this scope several approaches have been proposed: covalent modification of the fragment with

bulky substituents,^{7,11-13} trapping within molecular macrocages¹⁴⁻¹⁶ or porous frameworks,^{5,17,18} and synthesis of co-crystals based on halogen bonding interactions.^{19,20,21}

Recently, solid solutions of molecular materials have also become an attractive target in the design of functional materials. Crystalline solid solutions can be defined as non-stoichiometric multi-component crystals in which two, or even more, components combine homogeneously in a single crystalline phase. According to Kitaigorodsky,²² formation of a solid solution, that is, components miscibility in the solid state, depends on the similarity of the components in terms of size and shape. The pure components should, ideally, be isomorphous, or at least isostructural or quasi-isostructural.^{22,23} [The IUCr Online Dictionary of Crystallography reports the following definitions of isomorphism and isostructural crystals: Two crystals are said to be isomorphous if (a) both have the same space group and unit-cell dimensions and (b) the types and the positions of atoms in both are the same except for a replacement of one or more atoms in one structure with different types of atoms in the other (isomorphous replacement), such as heavy atoms, or the presence of one or more additional atoms in one of them (isomorphous addition). Two crystals are said to be isostructural if they have the same structure, but not necessarily the same cell dimensions nor the same chemical composition, and with a “comparable” variability in the atomic coordinates to that of the cell dimensions and chemical composition. The term isotypic is synonymous with isostructural]. The importance of solid solutions as a tool for modifying the physicochemical properties of materials has been recently emphasized in a series of studies on mixed crystals, where features such as melting point,^{24,25} polymorphic phase transition,^{26,27} enantioselectivity,^{28,29} mechanical,³⁰ optical,³¹ magnetic,³² and thermosalient effects,³³ among others, can be studied and finely “tuned” by controlling the composition. This approach has also been successfully applied to control the rotational frequency of 4,4'-bipyridine rotators in porous coordination polymers.³⁴ Notwithstanding the extensive research in this field, two aspects have not yet been explored, namely 1) the possibility of obtaining dynamic crystalline materials through mechanochemistry,³⁵ and 2) the effect of the solid-solution composition on the transition temperature at which molecular motion stops.

In this work we have made use of crystal engineering^{36,37} design principles for the preparation of supramolecular salts with general formula

$[1 \cdot (\text{DABCOH}_2)]\text{X}_2$, (where $1=12\text{-crown-4}$, $\text{X}=\text{Cl}^-$ or Br^-), see Scheme 3.2.1, in order to study the thermally-activated dynamic processes occurring in their crystalline state. Moreover, by taking advantage of interchangeability between halides,^{33,38} we have explored the preparation of binary solid solutions with general formula $[1 \cdot (\text{DABCOH}_2)]\text{Cl}_{2x}\text{Br}_{2(1-x)}$ ($0 < x < 1$), to investigate the effect of composition on the disorder–order transition temperature and dynamic processes of the mixed systems with respect to the pure parent materials.



Scheme 3.2.1 Building blocks used in the present study and pathway to assemble the supramolecular salts.

The mixed crystals have been investigated by a combination of solid-state techniques including variable-temperature single-crystal and powder X-ray diffraction (XRD), differential scanning calorimetry (DSC), hot stage microscopy (HSM) and solid-state NMR spectroscopy (SSNMR). The combined use of these methods has made possible not only rationalization of the correlation between the dynamic processes taking place within the crystalline materials and the solid-solution composition, but also to describe an uncommon molecular motion based on a precession of the $(\text{DABCOH}_2)^{2+}$ unit within the cavity delimited in the crystal structure by the crown ether and the halide packing.

3.2.2 Results and discussion

Crystal structures description

At room temperature, crystalline $[1 \cdot (\text{DABCOH}_2)]\text{Cl}_2$ and $[1 \cdot (\text{DABCOH}_2)]\text{Br}_2$ are isomorphous; they crystallize in the tetragonal space group $P4/n$ and form colourless square-like crystals (Figure SI-1 in Supporting Information). Both crystals feature infinite chains held by directional charge-assisted hydrogen bonds and running along the c -axis direction, in which each 12-crown-4 ether molecule is sandwiched between a $(\text{DABCOH}_2)^{2+}$ cationic unit and one halide anion, as shown in Figure 3.1.1. Each $(\text{DABCOH}_2)^{2+}$ cation, in turn, is surrounded by four extra-chain halide anions, also interacting through weak $\text{C-H} \cdots \text{X}^-$ hydrogen bonds (see Figure 3.1.1 and Table SI-1 for a list of distances).

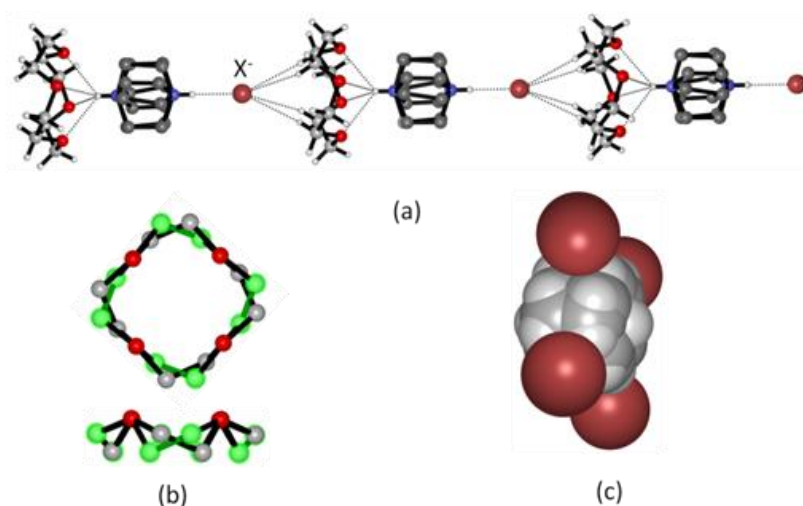


Figure 3.2.1 (a) The infinite hydrogen bonded chain in crystalline $[1 \cdot (\text{DABCOH}_2)]\text{Br}_2$, (b) top and side views of the disordered 12-crown-4 molecule (C atoms of the second image of disorder in green), and (c) the $(\text{DABCOH}_2)^{2+}$ dication surrounded by four bromide anions.

Both crystals feature disorder of the $(\text{DABCOH}_2)^{2+}$ cation, likely due to the fast rotation about its pseudo-three-fold axis,^{4,19} and disorder of the 12-crown-4 molecule. According to the literature,³⁹⁻⁴¹ disorder in crown ethers is caused by the up-down flips of the $-\text{CH}_2-\text{CH}_2-$ bridges ($E_a=0.85 \text{ kJ mol}^{-1}$) and by the pseudo-four-fold rotational jumps of the ring ($E_a=40-50 \text{ kJ mol}^{-1}$).

On decreasing the temperature both $[1 \cdot (\text{DABCOH}_2)]\text{Cl}_2$ and $[1 \cdot (\text{DABCOH}_2)]\text{Br}_2$ undergo a phase transition from tetragonal $P4/n$ to

monoclinic $P2_1/n$ (see data at 200 K in Table SI-2). It is possible to observe the ordering of the $(\text{DABCOH}_2)^{2+}$ cationic unit associated with this change in crystal symmetry. This behaviour indicates that one of the partially occupied sites at room temperature becomes more stable and fully occupied at low temperature, thus supporting a dynamic disorder model. The crown ether, in contrast, is still disordered at low temperature. The disorder of $(\text{DABCOH}_2)^{2+}$ is perfectly restored when the crystalline samples are heated back to RT (see Figure 3.2.2). DSC measurements (see below) also reveal that the two compounds undergo a reversible phase change at 292 and 290 K, respectively. Further evidence comes from the observation of birefringence variation under the cross-polarized hot-stage microscope (see Figure 3.2.3).

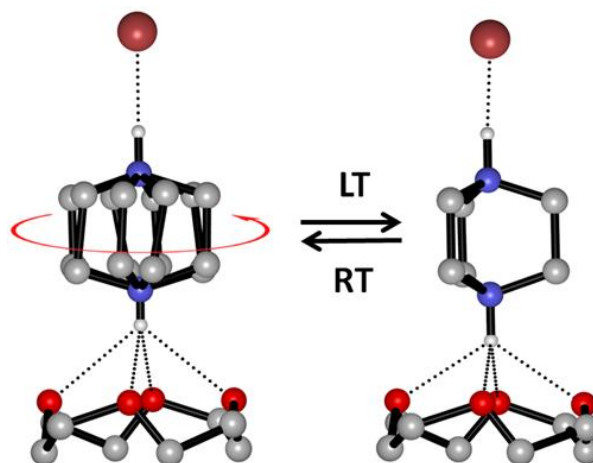


Figure 3.2.2 Representation of the fully reversible interconversion between the RT and LT phases for $[1 \cdot (\text{DABCOH}_2)]\text{Br}_2$. HCH and disorder over the 12-crown-4 omitted for clarity.

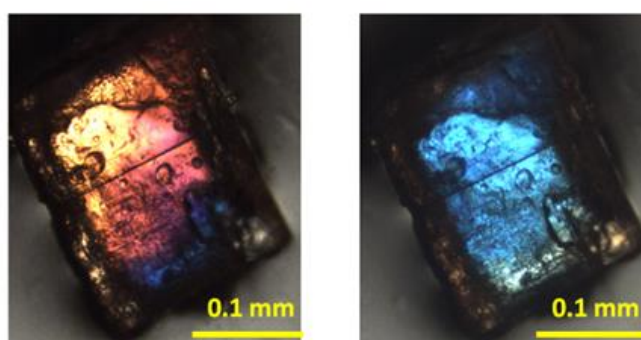


Figure 3.2.3 Cross-polarized HSM pictures showing the change in birefringence in a crystal of $[1 \cdot (\text{DABCOH}_2)]\text{Br}_2$ before (left) and after (right) the disorder-to-order/tetragonal-to-monoclinic phase transition.

Single crystals of the two salts were also subjected to an additional cooling cycle down to 100 K on the diffractometer. Only slight shrinking in the values of the unit cell parameters was observed for both solids, but no further phase transition was detected.

Solid solutions

The observed dynamic behaviour as a response to temperature variation, and the isomorphism of $[\mathbf{1}\cdot(\text{DABCOH}_2)]\text{Cl}_2$ and $[\mathbf{1}\cdot(\text{DABCOH}_2)]\text{Br}_2$ in both their room temperature and low temperature phases, prompted us to investigate the possibility of obtaining mixed-crystal phases. More specifically, we set to address the following questions:

1. Would the two salts form a solid solution or separate out in crystals of the two salts?
2. If a solid solution is formed from solution crystallization would it be possible to obtain the same result via mechanochemistry?
3. How could alloy formation affect the phase transition behaviour depending on the Cl^-/Br^- molar ratio, that is, would the phase transition temperature vary linearly as a function of the molar ratio, between the two extremes defined by the homo-anionic crystals, or not?

Mixed crystalline phases were successfully obtained from slow evaporation of water solutions containing $[\mathbf{1}\cdot(\text{DABCOH}_2)]\text{Cl}_2$ and $[\mathbf{1}\cdot(\text{DABCOH}_2)]\text{Br}_2$ in the molar ratios: 90:10, 75:25, 50:50, 25:75, 10:90. Alternatively they can be obtained by kneading (few drops of water) of the reactants in the same molar ratio. Dry grinding afforded a simple mixture of the two starting phases.

Powder diffraction patterns, recorded on materials obtained by kneading, showed a clear-cut proof of solid phase formation, isomorphous with those of pure $[\mathbf{1}\cdot(\text{DABCOH}_2)]\text{Cl}_2$ and $[\mathbf{1}\cdot(\text{DABCOH}_2)]\text{Br}_2$ in all cases. Figure 3.1.4 shows a detail of the comparison between experimental PXRD patterns of the parent materials and that of the mixed phase with a 50: 50 ratio, $[\mathbf{1}\cdot(\text{DABCOH}_2)]\text{ClBr}$, as an example.

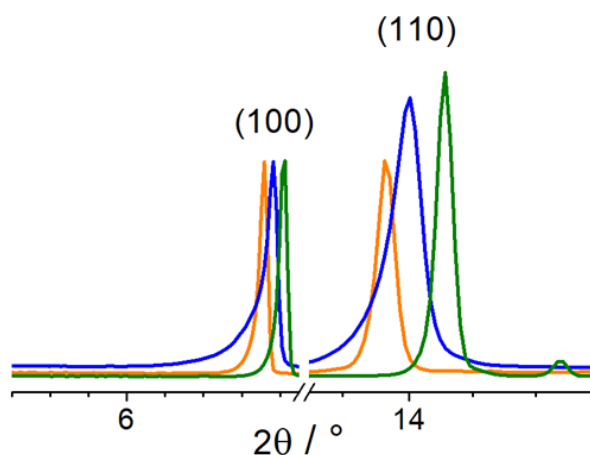


Figure 3.2.4 Details of the PXR D patterns showing the shifts of the (1 0 0) and (1 1 0) peaks towards higher angles upon increasing the molar fraction of Cl⁻. [1·(DABCOH₂)]Br₂ orange line, [1·(DABCOH₂)]ClBr blue line, and [1·(DABCOH₂)]Cl₂ green line.

Based on a comparison of the unit cell volumes extracted from Pawley refinements, the two supramolecular salts are indeed miscible, affording crystalline phases that follow Vegard's rule⁴² in the whole composition range (see Figure 3.2.5) and can indeed be formulated as [1·(DABCOH₂)]Cl_{2x}Br_{2(1-x)} (with 0 < x < 1).

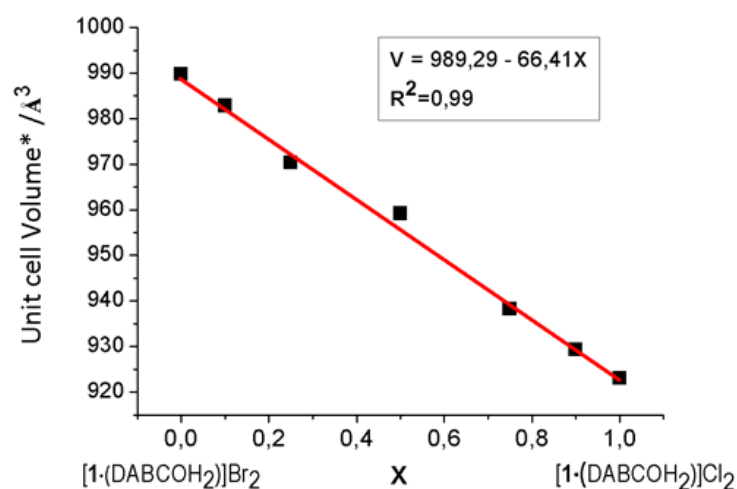


Figure 3.2.5 Linear dependence of unit cell volume (data from Pawley refinements) on the molar fraction of Cl⁻ in [1·(DABCOH₂)]Cl_{2x}Br_{2(1-x)}.

To determine the temperatures associated with the disorder–order phase transitions, each [1·(DABCOH₂)]Cl_{2x}Br_{2(1-x)} crystalline powder was subjected to a full cycle (cooling–heating–cooling) of differential scanning calorimetry (DSC) measurements. The measurements were carried out below the thermal

decomposition corresponding to the crown ether loss (see Figure SI-3 in Supporting Information). Figure 3.2.6 shows the plot of transition temperatures versus composition.

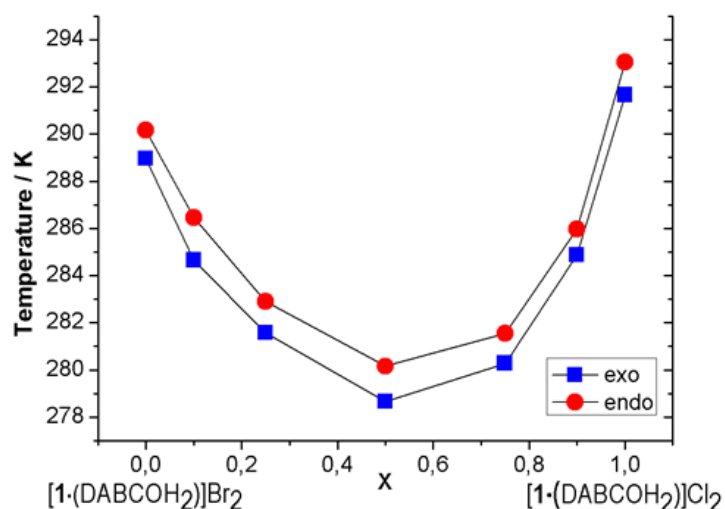


Figure 3.2.6 Temperature variations (from DSC, peak temperatures) of the disorder–order transition for $[1\cdot(\text{DABCOH}_2)]\text{Cl}_{2x}\text{Br}_{2(1-x)}$ with $x=0, 0.1, 0.25, 0.5, 0.75, 0.90,$ and 1 .

As in the cases of the pure materials, the transitions are fully reversible, with some hysteresis. Moreover, the DSC traces showed how the phase transition behaviour does not vary linearly with the composition, and how the peak corresponding to the disorder–order transition “drops” as the molar fraction of Cl^- is changed, reaching a minimum for $x=0.5$.

To dispel any doubt concerning the disorder–order transition we also carried out single-crystal analyses at temperatures corresponding to before and after the DSC peak for $[1\cdot(\text{DABCOH}_2)]\text{Cl}_{2x}\text{Br}_{2(1-x)}$ with $x=0, 1,$ and 0.5 (see Figure 3.2.7). This experiment confirms what formerly observed at RT and LT for each phase. Transition enthalpies (ΔH) for the disorder–order transition were estimated to be of ca. -1.0 kJ mol^{-1} for all crystalline phases. This might imply that reorientation of the $(\text{DABCOH}_2)^{2+}$ cationic unit is substantially unaffected by the type of the surrounding halide anion.

Further evidence of the reversible phase transition comes from variable-temperature X-ray powder diffraction. Figure 3.2.8 shows the changes in the XRD pattern for $[1\cdot(\text{DABCOH}_2)]\text{Br}_2$ observed upon cooling a polycrystalline sample below the transition temperature. $[1\cdot(\text{DABCOH}_2)]\text{Cl}_2$ and $[1\cdot(\text{DABCOH}_2)]\text{ClBr}$ behave similarly; see Figure SI-5.

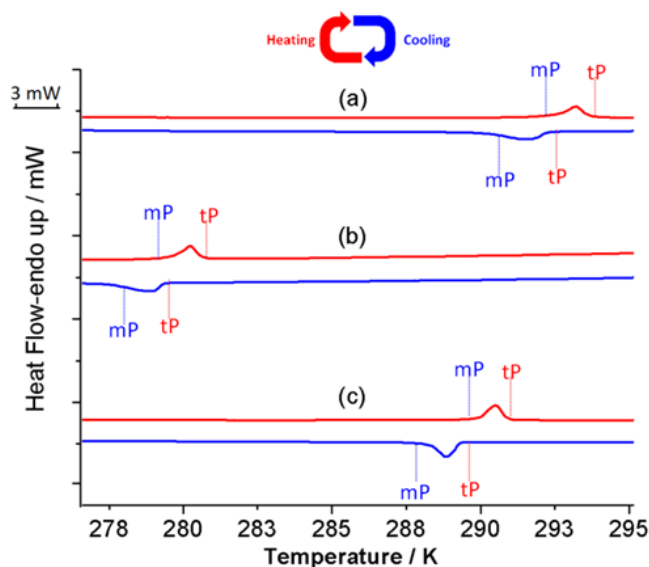


Figure 3.2.7 DSC traces measured on $[1 \cdot (\text{DABCOH}_2)]\text{Cl}_{2x}\text{Br}_{2(1-x)}$: (a) $x=1$, (b) $x=0.5$, and (c) $x=0$. tP and mP stand for the disordered (tetragonal P) and ordered (monoclinic P) crystal phases, respectively.

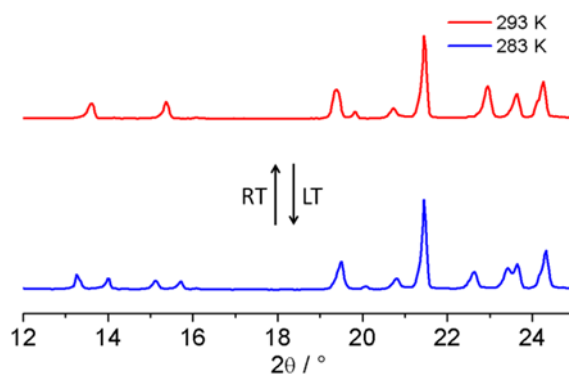


Figure 3.2.8 Details of the variable temperature PXRD patterns of $[1 \cdot (\text{DABCOH}_2)]\text{Br}_2$; the phase transition occurring upon lowering the temperature is visible from the marked change of the peaks at ca. 13, 15 and 24°.

Solid-state NMR-dynamics

The SSNMR measurements were instrumental to the elucidation of the dynamic processes. Interestingly, ^{13}C cross-polarised magic-angle spinning (CPMAS) spectra of $[1 \cdot (\text{DABCOH}_2)]\text{Cl}_2$, $[1 \cdot (\text{DABCOH}_2)]\text{Br}_2$ and $[1 \cdot (\text{DABCOH}_2)]\text{ClBr}$ at room temperature afforded only the DABCO- CH_2 peak (around 45 ppm), thus ^{13}C MAS spectra were acquired. Figure 3.1.9 shows ^{13}C MAS SSNMR spectra of $[1 \cdot (\text{DABCOH}_2)]\text{Cl}_2$, $[1 \cdot (\text{DABCOH}_2)]\text{Br}_2$ and $[1 \cdot (\text{DABCOH}_2)]\text{ClBr}$ at room temperature. For the three samples, two different signals were observed at 45.2 and 66.4 ppm, assigned to the $-\text{CH}_2$ groups of

(DABCOH₂)²⁺ and 12-crown-4, respectively. The lack of the crown ether CH₂ signals in the ¹³C CPMAS spectra, together with short ¹³C relaxation delays, the large line width of the 12-crown-4 signal (FWHM=200–340 Hz), as well as the need of acquiring MAS experiments on solid samples, confirm the presence of dynamic processes. This prompted us to perform variable temperature (VT) NMR measurements. The ¹³C MAS spectra of [1·(DABCOH₂)]Cl₂ recorded at different temperature values, from 253 to 323 K, are reported in Figure 3.1.10.

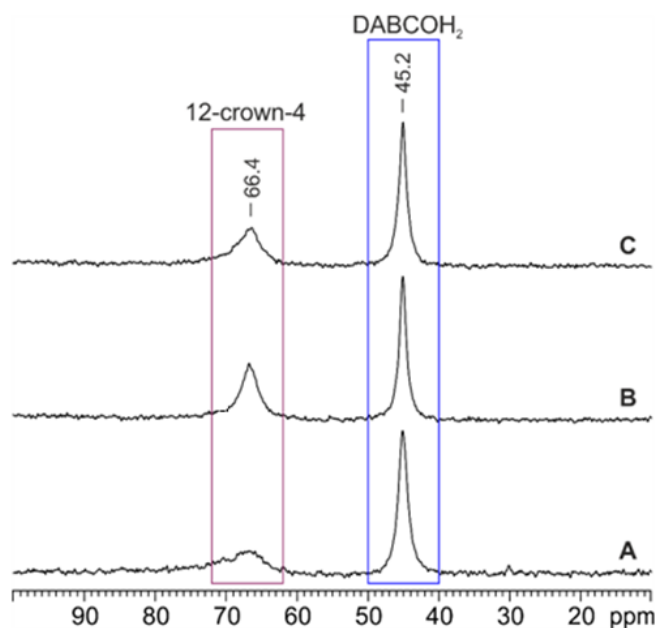


Figure 3.2.10 Room temperature ¹³C (150.9 MHz) MAS SSNMR spectra of A) [1·(DABCOH₂)]Cl₂, B) [(1·(DABCOH₂)]Br₂ and C) [1·(DABCOH₂)]ClBr acquired at a spinning speed of 20 kHz.

By changing the temperature, the crown ether signal does not change significantly as it is disordered at all temperatures in agreement with the X-ray data (see above). On the other hand, the resonance at lower ppm undergoes a significant change: Two distinct resonances are observed at low temperatures (44.0 and 46.2 ppm); as the temperature is increased, the two signals coalesce and merge as a single signal centred at 45.3 ppm, whereas no significant change is observed for the high-frequency CH₂ resonance. The coalescence temperature is around 278 K. From the VT spectra it is clear that RT and LT structures are very similar from the NMR point of view. The differences stem on the features related to the dynamic process, rather than the phase transition.

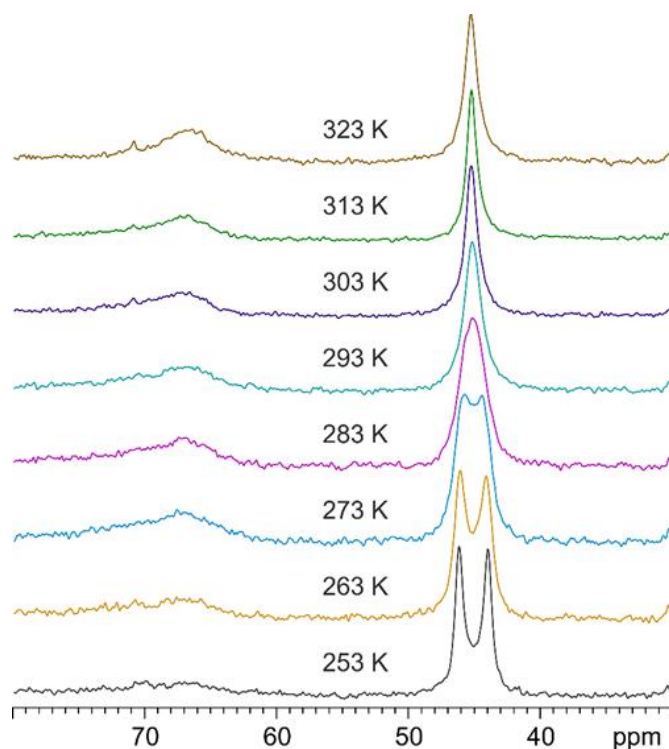


Figure 3.2.11 VT ^{13}C (150.9 MHz) MAS SSNMR spectra of $[(1\text{-}(\text{DABCOH}_2))\text{Cl}_2]_2$, acquired at a spinning speed of 20 kHz.

Similar response is observed for both $[1\text{-}(\text{DABCOH}_2)]\text{Br}_2$ and $[1\text{-}(\text{DABCOH}_2)]\text{ClBr}$, (see Figures SI-6 and SI-7 in Supporting Information). In these cases, however, the coalescent temperature is around 268 K, suggesting a lower activation energy.

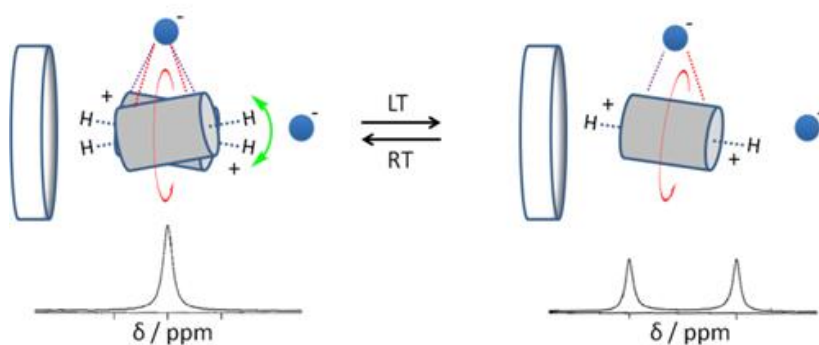
The activation energies for the dynamic processes can be evaluated by lineshape analysis and values of 52.7, 50.6 and 50.6 kJ mol^{-1} are obtained for $[1\text{-}(\text{DABCOH}_2)]\text{Cl}_2$, $[1\text{-}(\text{DABCOH}_2)]\text{Br}_2$ and $[1\text{-}(\text{DABCOH}_2)]\text{ClBr}$, respectively.

In order to evaluate if the hydrogen atom is involved in the dynamic, the deuterium analogue of $[1\text{-}(\text{DABCOH}_2)]\text{Cl}_2$ was synthesized (see Experimental Section). Figure SI-8 shows the comparison between the VT ^{13}C MAS spectra of $[1\text{-}(\text{DABCOH}_2)]\text{Cl}_2$ and $[1\text{-}(\text{DABCOD}_2)]\text{Cl}_2$ in the 193–313 K range. We found a different coalescence temperature: 278 K for the hydrogen derivative and 293 K for the deuterium analogue, suggesting the presence of a kinetic isotopic effect. The corresponding calculated activation energy for $[1\text{-}(\text{DABCOH}_2)]\text{Cl}_2$ is 58.5 kJ mol^{-1} . The kinetic isotope effect, $K_{\text{H}}/K_{\text{D}}$, measured at 293 K is 5.3. It is well known that deuterium substitution will lead to lower vibration frequencies or, viewed quantum-mechanically, will have lower zero-point energy. With a lower zero-point energy, more energy must be supplied to break

the bond, resulting in a higher activation energy for bond cleavage, which in turn lowers the measured exchange rate.⁴³ This relevant kinetic isotope effect confirms that the hydrogen atom bound to the nitrogen plays a role on the dynamic under investigation.

The rotation of DABCO unit along its pseudo-three-fold axis has been already reported in several cases in the literature,^{4, 19} and accounts for the short ¹³C relaxation delays (<5 s). Such motion is expected to have a very low activation energy and cannot be frozen at the lowest achievable NMR temperature. Thus, the reported behaviour upon varying the temperature suggests the presence of a second dynamic process which accounts for the loss of symmetry of the DABCO-CH₂ which, at low temperature, gives rise to two distinct peaks. Such large chemical shift difference of the CH₂ resonances cannot be related to the presence of the halide and the crown ether along the (DABCOH₂)²⁺ axis. For example, no chemical shift difference has been found in the case of the ¹³C CPMAS spectrum of the adduct between DABCO and malonic acid, where one of the nitrogen forms a strong hydrogen bond with the carboxylic acid, whereas the other is a free nitrogen.⁴⁴ Thus, the difference in the CH₂ resonances at low temperature is probably due to the presence of the surrounding four halides. Beside the rotation of the (DABCOH₂)²⁺, we surmise an additional precession motion of the cationic unit around its principal axis at room temperature (see Scheme 3.2.2), during which the N⁺-H moiety interacts in turn with each oxygen atom of the crown ether. This would explain also the presence of the kinetic isotope effect that is related to the breaking and forming of the N⁺-H...O_{crown} or N⁺-D...O_{crown} interactions in [1·(DABCOH₂)]Cl₂ and [1·(DABCOD₂)]Cl₂. This agrees with the slight (DABCOH₂)²⁺ misalignment (ca 1–2°) between the (DABCOH₂)²⁺ pseudo-threefold axis and the crown ether pseudo-fourfold axis, which leads to slightly shorter N⁺-H...O_{crown} distances as observed in the low temperature X-ray structure (see Table SI-1).

By performing such motion, the two different -CH₂- groups of the rotating (DABCOH₂)²⁺ change their position with respect to the surrounding four halides, averaging their relative environment in the RT range and leading to the single peak observed on the VT ¹³C MAS spectra.



Scheme 3.2.2 Representation of the dynamic model inferred from VT ^{13}C MAS SSNMR experiments showing the precession motion that accompanies the rotation of the $(\text{DABCOH}_2)^{2+}$ around its pseudo-three-fold axis, and the slight misalignment which causes signal coalescence loss following the phase transition.

3.2.3 Conclusions

In this paper we have reported our findings on the solid-state dynamic behaviour and phase transition of the supramolecular salts of general formula $[\mathbf{1} \cdot (\text{DABCOH}_2)]\text{X}_2$ (where $\mathbf{1}$ =12-crown-4; $\text{X}=\text{Cl}^-$ or Br^-) and of their solid solutions, namely $[\mathbf{1} \cdot (\text{DABCOH}_2)]\text{Cl}_{2x}\text{Br}_{2(1-x)}$. These latter compounds were prepared mechanochemically by mixing the parent compounds in different stoichiometric ratios.

Our findings can be summarized as follows: 1) the salts $[\mathbf{1} \cdot (\text{DABCOH}_2)]\text{X}_2$ are isostructural and their crystals are isomorphous; 2) both compounds undergo a reversible order–disorder enantiotropic transition from a higher to a lower symmetry phase at temperatures close to RT (292 and 290 K, for $x=1$ and 0, respectively); 3) their solid solutions also undergo the same kind of phase transition and show a coherent decrease of the transition temperatures with a minimum at 278 K corresponding to the composition Cl:Br 1:1; 4) the order–disorder phase transitions, investigated by a combination of X-ray diffraction and solid-state NMR spectroscopy, are associated with the uprising of reorientational motion of the $(\text{DABCOH}_2)^{2+}$ dications within a “cage”, formed by one 12-crown-4 molecule on one side, a halide ion on the other side, and by four surrounding halide ions; 5) the solid solutions behave exactly in the same way, confirming that the dynamic process involves the mobile $(\text{DABCOH}_2)^{2+}$ dication; 6) activation energies of ca. 50 kJ mol^{-1} , associated in all cases to the dynamic processes, have been evaluated by VT ^{13}C MAS SSNMR spectroscopy and line-shape analysis.

We have argued that a simple rotation of the DABCO core around the molecular threefold axis, as observed in many other DABCO containing crystals, cannot account for the spectroscopic evidence, whereas a more complex precessional motion could explain the differences between high and low temperature solid-state structures, the small enthalpy involved in the fully reversible processes, and the intriguing spectroscopic features discussed above.

The compound 1,4-diazabicyclo[2.2.2]octane, DABCO, is most certainly a very popular, and extensively investigated mobile molecular fragment. However, to the best of the authors' knowledge, this is the first observation of a room temperature precessional motion that is frozen as the hosting cage is made tighter by decreasing the temperature.

3.2.4 Experimental Section

All reactants and reagents were purchased from Sigma–Aldrich and used without further purification, double distilled water was used.

Synthesis. 1,4-diazabicyclo[2.2.2]octane (DABCO) and 12-crown-4 were mixed together in stoichiometric ratio 1: 1. Hydrochloric or hydrobromic acid were added dropwise to reach pH 5. The resulting solution was boiled for a few minutes and left to stand in the air at room temperature. After a few days single crystals of $[1 \cdot (\text{DABCOH}_2)]\text{X}_2$ ($\text{X}=\text{Cl}^-$ or Br^-) grew from solution, were collected by filtration and washed with cold ethanol. $[1 \cdot (\text{DABCOd}_2)]\text{Cl}_2$ was obtained by using deuterium chloride (DCl) instead of HCl; the obtained crystals were washed with EtOH-d6.

Solid solutions were prepared by grinding quantities of pure $[1 \cdot (\text{DABCOH}_2)]\text{Cl}_2$ and $[1 \cdot (\text{DABCOH}_2)]\text{Br}_2$, weighed in the proper molar ratio (10:90, 25:75, 50:50, 75:25, 91:10) and in the presence of few drops of water; alternatively, they could be obtained by slow evaporation of an aqueous solution. The amounts of reagents for each synthesis was chosen so that ca. 100–200 mg of solid product could be obtained.

Single-crystal X-ray diffraction. Single-crystal data for all supramolecular salts were collected either at RT (300 K) and LT (200 K) on an Oxford X'Calibur S CCD diffractometer equipped with a graphite monochromator ($\text{MoK}\alpha$ radiation, $\lambda=0.71073 \text{ \AA}$) and with a cryostat Oxford CryoStream800.

Data collection and refinement details are listed in Supporting Information Table S1. All non-hydrogen atoms were refined anisotropically. H_{CH} atoms were added in calculated positions and refined riding on their respective carbon atoms; H_{NH} atoms were either directly located or, when not possible, added in calculated positions. The structures were solved with SHELXT⁴⁵ and refined on full-matrix F^2 by means of the SHELXL package,⁴⁶ implemented in Olex2 software.⁴⁷ The data collected at RT showed disordered positions for the CH₂ atoms belonging to both DABCO and crown ether. Methylene atoms of the crown ether were split over two conformations with occupancies fixed at 0.5; where necessary, their thermal parameters were restrained using ISOR and/or SIMU and DELU instructions. Since the disorder involving DABCO is roughly continuous, a fictitious molecule comprising four methylene bridges is generated by the fourfold symmetry imparted by the crown ether. The CH₂ atoms in the model were then further split over two different conformations fixing their occupancies at $(3/4)/2=0.375$; because of the strong elongation, their thermal parameters were restrained using ISOR and SIMU instructions, while the corresponding hydrogen atoms were omitted.

All the LT data displayed crystal twinning. [(1·(DABCOH₂))]Br₂ and [(1·(DABCOH₂))]BrCl were treated with the default configuration for twinned crystals of CrysAlisPro, and structure solution and refinement were performed on the HKLF4 file containing the non-overlapped reflections; due to the strong overlapping, [(1·(DABCOH₂))]Cl₂ was instead treated as a single crystal and the size of the integration mask was increased by 25 %. In all cases the crown ethers were disordered and they were treated as detailed above for RT data.

In the structures of [(1·(DABCOH₂))]BrCl it was not always possible to unequivocally locate from the Fourier maps the independent positions of the two anions. In this case, the model was approximated by forcing the two anions to the same fixed coordinates, thermal parameters and with half occupancies. Where two independent positions were visible, Cl and Br anions were refined freely with 0.5 occupancy.

The program Mercury 3.1 was used to calculate intermolecular interactions and for molecular graphics. [CCDC 1849206–1849211](#) contain the supplementary crystallographic data for this paper. These data are provided free of charge by [The Cambridge Crystallographic Data Centre](#).

Powder X-ray diffraction. For phase identification and Pawley refinement purposes, X-ray powder diffraction patterns (XRPD) were collected on a PANalytical X'Pert PRO automated diffractometer with transmission geometry, equipped with Focusing Mirror and Pixcel detector, in the 2θ range 3–70° (step size 0.0260°, time/step 200 s, 0.04 rad soller; 40 kV, 40 mA). Powder diffraction data were analysed with the software TOPAS4.1.⁴⁸ A shifted Chebyshev function with 7 parameters was used to fit the background.

Thermogravimetric analysis (TGA). TGA analyses were performed with a PerkinElmer TGA-7. Each sample, contained in a platinum crucible, was heated in a nitrogen flow (20 cm³ min⁻¹) at a rate of 5 °C min⁻¹, up to decomposition. Sample weights were in the range 5–10 mg.

Differential scanning calorimetry (DSC). Calorimetric measurements were performed with a PerkinElmer DSC-7 equipped with a PII intracooler. Temperature and enthalpy calibrations were performed using high-purity standards (n-decane, benzene and indium). Heating of the aluminium open pans containing the samples (3–5 mg) was carried out at 5 °C min⁻¹ in the temperature range 40–300 °C.

Hot-stage and cross-polarized optical microscopy (HSM-CP). Hot-stage experiments were carried out using a Linkam TMS94 device connected to a Linkam LTS350 platinum plate and equipped with polarizing filters. Images and movies were collected with the imaging software VisiCam Analyzer, from an Olympus BX41 stereomicroscope.

Solid-state NMR spectroscopy. 1D ¹³C MAS spectra were acquired on a Jeol ECZR 600 instrument, operating at 600.17 and 150.91 MHz for the ¹H and ¹³C nuclei, respectively. Powder samples were packed in 3.2 mm diameter cylindrical zirconia rotors with a volume of 60 μL. A certain amount of sample was taken and used without further preparation from each batch to fill the rotor. ¹³C MAS spectra were acquired at a spinning speed of 20 kHz with a 90° ¹³C pulse of 2.0 μs, a recycle time of 10 s and 64 scans. The two-pulse phase modulation (TPPM) decoupling scheme with a 119.0 kHz radiofrequency field was used. ¹³C chemical shifts were referenced to glycine (¹³C methylene signal).

Variable-temperature operation was achieved by a triple gas channel MAS probe, in which the stream of VT gas is separated from the MAS bearing and driving gases. The driving gas is used to propel the rotor at high speeds, while the bearing gas provides an air cushion for stability. The low temperatures were achieved by cooling the VT line through a flow of boil-off N₂ gas from an exchange Dewar filled with liquid nitrogen. The VT gas was then directed at the mid-point of the sample rotor. For the high temperature operations, VT and MAS gases were air heated by means of a resistance put inside the probe. A thermocouple was used for temperature measurement and regulation. The temperature was calibrated using the well-established method based on the ²⁰⁷Pb NMR resonance of solid Pb(NO₃)₂.⁴⁹⁻⁵²

References

- (1) W. Setaka, K. Yamaguchi, *Proc. Natl. Acad. Sci.* **2012**, *109*, 9271–9275.
- (2) Z. Sun, J. Luo, S. Zhang, C. Ji, L. Zhou, S. Li, F. Deng, M. Hong, *Adv. Mater.* **2013**, *25*, 4159–4163.
- (3) T. Akutagawa, H. Koshinaka, D. Sato, S. Takeda, S. Noro, H. Takahashi, R. Kumai, Y. Tokura, T. Nakamura, *Nat. Mater.* **2009**, *8*, 342–347.
- (4) A. Katrusiak, M. Szafranski, *Phys. Rev. Lett.* **1999**, *82*, 576–579.
- (5) S. Bracco, M. Beretta, A. Cattaneo, A. Comotti, A. Falqui, K. Zhao, C. Rogers, P. Sozzani, *Angew. Chemie - Int. Ed.* **2015**, *54*, 4773–4777.
- (6) S. Bracco, F. Castiglioni, A. Comotti, S. Galli, M. Negroni, A. Maspero, P. Sozzani, *Chem. - A Eur. J.* **2017**, *23*, 11210–11215.
- (7) S. D. Karlen, R. Ortiz, O. L. Chapman, M. A. Garcia-Garibay, *J. Am. Chem. Soc.* **2005**, *127*, 6554–6555.
- (8) D. Braga, *Chem. Rev.* **1992**, *92*, 633–665.
- (9) C. S. Vogelsberg, M. A. Garcia-Garibay, *Chem. Soc. Rev.* **2012**, *41*, 1892–1910.
- (10) C. S. Vogelsberg, F. J. Uribe-romo, A. S. Lipton, S. Yang, K. N. Houk, S. Brown, **2017**, 2–7.
- (11) Z. J. Obrien, S. D. Karlen, S. Khan, M. A. Garcia-Garibay, *J. Org. Chem.* **2010**, *75*, 2482–2491.
- (12) Z. J. O'Brien, A. Natarajan, S. Khan, M. A. Garcia-Garibay, *Cryst Growth Des.* **2011**, *11*, 2654–2659.
- (13) P. Commins, M. A. Garcia-Garibay, *J. Org. Chem.* **2014**, *79*, 1611–1619.
- (14) A. Fujiwara, Y. Inagaki, H. Momma, E. Kwon, K. Yamaguchi, M. Kanno, H. Kono, W. Setaka, *CrystEngComm* **2017**, *19*, 6049–6056.
- (15) W. Setaka, S. Higa, K. Yamaguchi, *Org. Biomol. Chem.* **2014**, *12*, 3354–3357.
- (16) Y. Nishiyama, Y. Inagaki, K. Yamaguchi, W. Setaka, *J. Org. Chem.* **2015**, *80*, 9959–9966.
- (17) A. Comotti, S. Bracco, P. Sozzani, *Acc. Chem. Res.* **2016**, *49*, 1701–1710.
- (18) S. Devautour-Vinot, G. Maurin, C. Serre, P. Horcajada, D. Paula Da Cunha, V. Guillermin, E. De Souza Costa, F. Taulelle, C. Martineau, *Chem. Mater.* **2012**, *24*, 2168–2177.
- (19) (a) L. Catalano, S. Pérez-Estrada, G. Terraneo, T. Pilati, G. Resnati, P. Metrangolo, M. A. Garcia-Garibay, *J. Am. Chem. Soc.* **2015**, *137*, 15386–15389. (b) L. Catalano, P. Naumov, *CrystEngComm*, **2018**, 10.1039/C8CE00420J
- (20) L. Catalano, S. Perez-Estrada, H. Wang, A. J.-L. Ayitou, S. I. Khan, G. Terraneo, P. Metrangolo, S. Brown, M. A. Garcia-Garibay, *J. Am. Chem. Soc.* **2017**, *139*, 843–848.

- (21) C. Lemouchi, C. S. Vogelsberg, L. Zorina, S. Simonov, P. Batail, S. Brown, M. A. Garcia-Garibay, *J. Am. Chem. Soc.* **2011**, *133*, 6371–6379.
- (22) A. I. Kitaigorodsky, *Mixed Crystals*, Springer Berlin Heidelberg, Berlin, Heidelberg, **1984**.
- (23) M. Lusi, *Cryst. Growth Des.* **2018**, acs.cgd.7b01643.
- (24) A. K. S. Romasanta, D. Braga, M. T. Duarte, F. Grepioni, *CrystEngComm* **2017**, *19*, 653–660.
- (25) E. Schur, E. Nauha, M. Lusi, J. Bernstein, *Chem. - A Eur. J.* **2015**, *21*, 1735–1742.
- (26) D. Braga, D. Paolucci, G. Cojazzi, F. Grepioni, *Chem. Commun.* **2001**, 803–804.
- (27) A. Delori, P. Maclure, R. M. Bhardwaj, A. Johnston, A. J. Florence, O. B. Sutcliffe, I. D. H. Oswald, *CrystEngComm* **2014**, *16*, 5827.
- (28) T. Rekis, S. d'Agostino, D. Braga, F. Grepioni, *Cryst. Growth Des.* **2017**, acs.cgd.7b01146.
- (29) T. Rekis, A. Berziņš, I. Sarceviča, A. Kons, M. Balodis, L. Orola, H. Lorenz, A. Actiņš, *Cryst. Growth Des.* **2018**, *18*, 264–273.
- (30) M. K. Mishra, U. Ramamurty, G. R. Desiraju, *J. Am. Chem. Soc.* **2015**, *137*, 1794–1797.
- (31) L. Kuroki, S. Takami, K. Shibata, M. Irie, *Chem. Commun.* **2005**, 6005.
- (32) R. D. Willett, R. E. Butcher, C. P. Landee, B. Twamley, *Polyhedron* **2006**, *25*, 2093–2100.
- (33) E. Nauha, P. Naumov, M. Lusi, *CrystEngComm* **2016**, *18*, 4699–4703.
- (34) M. Inukai, T. Fukushima, Y. Hijikata, N. Ogiwara, S. Horike, S. Kitagawa, *J. Am. Chem. Soc.* **2015**, *137*, 12183–12186.
- (35) D. Braga, L. Maini, F. Grepioni, *Chem. Soc. Rev.* **2013**, *42*, 7638.
- (36) D. Braga, F. Grepioni, A. G. Orpen, *Crystal Engineering: From Molecules and Crystals to Materials*, Springer Netherlands, Dordrecht, **1999**.
- (37) D. Braga, F. Grepioni, L. Maini, S. D'Agostino, *IUCrJ* **2017**, *4*, 369–379.
- (38) C. J. Adams, M. F. Haddow, M. Lusi, A. G. Orpen, *Proc. Natl. Acad. Sci.* **2010**, *107*, 16033–16038.
- (39) C. I. Ratcliffe, J. A. Ripmeester, G. W. Buchanan, J. K. Denike, *J. Am. Chem. Soc.* **1992**, *114*, 3294–3299.
- (40) C. I. Ratcliffe, G. W. Buchanan, J. K. Denike, *J. Am. Chem. Soc.* **1995**, *117*, 2900–2906.
- (41) G. W. Buchanan, A. Moghimi, C. I. Ratcliffe, *Can. J. Chem.* **1996**, *74*, 1437–1446.
- (42) A. R. Denton, N. W. Ashcroft, *Phys. Rev. A* **1991**, *43*, 3161–3164.
- (43) A. Kohen, *Prog. React. Kinet. Mech.* **2003**, *28*, 119–156.
- (44) D. Braga, L. Maini, G. De Sanctis, K. Rubini, F. Grepioni, M. R. Chierotti, R. Gobetto, *Chem. - A Eur. J.* **2003**, *9*, 5538–5548.
- (45) G. M. Sheldrick, *Acta Crystallogr. Sect. A Found. Crystallogr.* **2015**, *71*, 3–8.
- (46) G. M. Sheldrick, *Acta Crystallogr. Sect. C Struct. Chem.* **2015**, *71*, 3–8.
- (47) O. V. Dolomanov, L. J. Bourhis, R. J. Gildea, J. A. K. Howard, H. Puschmann, *J. Appl. Crystallogr.* **2009**, *42*, 339–341.
- (48) A. Cohelo, *Topas v4.1*, **2007**.
- (49) A. Bielecki, D. P. Burum, *J. Magn. Reson. Ser. A* **1995**, *116*, 215–220.
- (50) L. C. M. van Gorkom, J. M. Hook, M. B. Logan, J. V. Hanna, R. E. Wasylshen, *Magn. Reson. Chem.* **1995**, *33*, 791–795.
- (51) T. Takahashi, H. Kawashima, H. Sugisawa, Toshihide Baba, *Solid State Nucl. Magn. Reson.* **1999**, *15*, 119–123.
- (52) X. Guan, R. E. Stark, *Solid State Nucl. Magn. Reson.* **2010**, *38*, 74–76.

3.3 Solid-state Dynamics and High-pressure Studies of a Supramolecular Spiral Gear

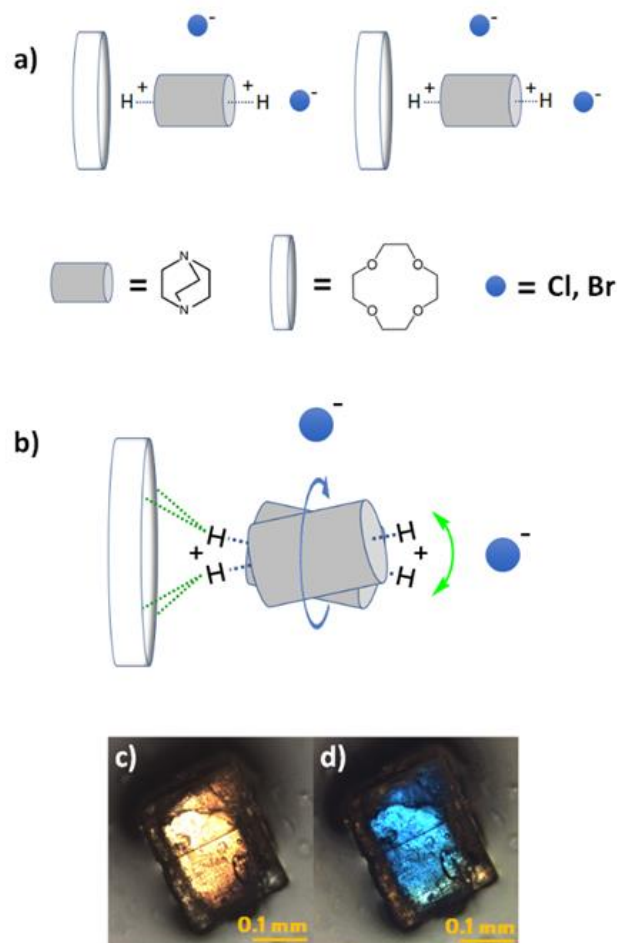
Fornasari L.; d'Agostino S.; Braga, D.; Rossi, F.; Chierotti, M. R.; Gobetto, R.; Olejniczak A.; Katrusiak A. - Manuscript in preparation

3.3.1 Introduction

The study of dynamic reorientational processes in crystals, such as molecular rotations or librations, has challenged scientists for decades in view of the unique nature of those phenomena, subverting the common perception of crystals as static entities.¹⁻⁷ Recently, a renewed interest in the field was driven by the surge of artificial molecular machines. The design of crystalline materials possessing components in rapid motion is considered a promising platform for the development of functional materials ranging from switchable ferroelectrics to gas and vapor sensors, dielectric constant modulators, birefringence and thermal expansion modulators.⁸⁻¹³ The study of molecular rotations has been performed on a variety of solids: molecular crystals, co-crystals and salts, Metal-Organic Frameworks (MOFs), inclusion compounds, porous organic frameworks and dendritic structures.¹⁴⁻¹⁷

The common approach in designing such materials relies on the control of the free volume, *i.e.* granting the rotary component sufficient void volume in the local environment for the rotation to be allowed. Indeed, it is generally assumed that the motions are of a biased-Brownian type, the bias being an interplay of steric hindrance and electronic barrier in the case the rotating molecule is connected to a stationary component via covalent bonds.^{15,18} So, a loosely packed structure is desirable to lower the activation energy for the rotation and hence increase its frequency. We recently showed that weak interactions as well can play a significant role (see paragraph 3.2 and ref. 19). We reported the dynamics of a supramolecular complex of DABCOH₂X₂ (X=Cl or Br) and 12-crown-4, in which chains are formed as represented in scheme 3.3.1, consisting of the repetition of one molecule of crown ether, one of doubly protonated DABCO and a counterion. It was observed that labile N-H...O bonds between the DABCOH₂²⁺ molecule and the crown ether are the driving force in the origin of a complex precessional motion, since the DABCOH₂²⁺ unit is forcefully tilted with respect to its rotation axis, causing a fast and

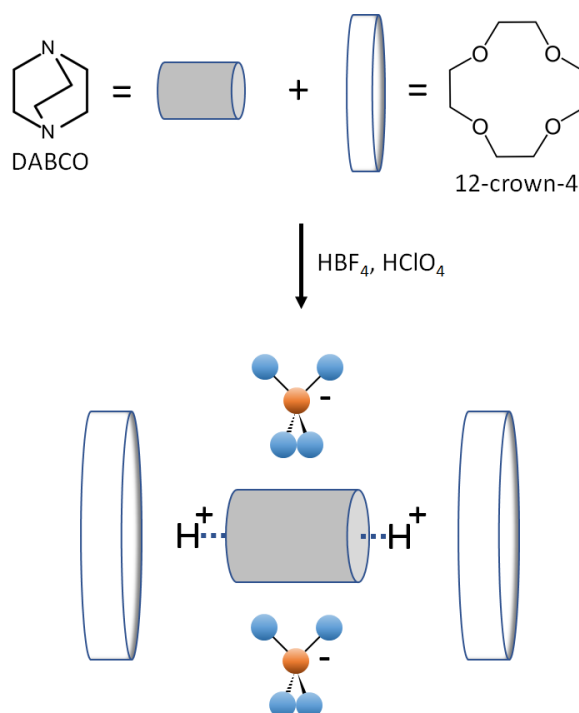
reversible transition from a tetragonal to a monoclinic symmetry that affects the birefringence of the crystals (see Scheme 3.3.1).



Scheme 3.3.1 a) Building blocks composing [(12-crown-4)·DABCOH₂](X)₂ (X=Cl, Br); b) pictorial representation of the precessional motion; c) and d) optical photographs under polarized white light of a crystal of [(12-crown-4)·DABCOH₂](Br)₂ below and above T_c respectively.

In this framework, the rotational dynamics of a typical rotor can be schematized as a multiple-well potential energy curve in which the energy barriers are defined by the interplay of steric repulsion, electronic factors and electrostatic interactions. The motion is therefore activated or deactivated by thermal energy. In this regard, the application of pressure to the system offers a promising approach to the modulation of the potential energy curve, owing to the fact that both the packing density and the weak interactions are profoundly affected by pressure.^{20–23} It is often assumed that pressure and temperature are in inverse relation, *i.e.* the effect of the high pressure is

comparable to that of low temperature, but this does not necessarily hold, especially in crystals possessing anisotropic compressibility.^{24,25}



Scheme 3.3.2 Building blocks composing $[(12\text{-crown-}4)_2\cdot\text{DABCOH}_2](\text{X})_2$ ($\text{X}=\text{BF}_4, \text{ClO}_4$)

In the present work, we describe the dynamics of the supramolecular complexes $[(12\text{-crown-}4)_2\cdot\text{DABCOH}_2](\text{X})_2$ (where $\text{X}=\text{BF}_4, \text{ClO}_4$) (see scheme 3.3.2), that are, in fact, an iteration of the design principles adopted previously (see paragraph 3.2). Here complexity is added to the system using tetragonal instead of spherical anions; as a result, discrete structural units are formed, that self-assemble in a chiral structure. The solids were investigated by a combination of XRD techniques, solid-state NMR and thermal analyses, showing that both the DABCOH_2^{2+} cations and the crown ethers undergo fast rotational motions. Furthermore, the structure determination of $[(12\text{-crown-}4)_2(\text{DABCOH}_2)](\text{BF}_4)_2$ at high pressure was performed through single-crystal XRD experiments in a Diamond Anvil Cell (DAC). The analysis of the high-pressure structural features combined with the ambient-pressure crystallographic and spectroscopic evidences elucidates a geared rotational motion between the 12-crown-4 ethers: the up/down flip motion of the methylene bridges is hampered and the ethers are locked in a chiral conformation, resembling the macroscopic functioning of meshed spiral gears.

Despite the peculiarity of the chosen model compound, we believe that the results are of general interest, pointing out that pressure is a crucial variable in the modulation of the dynamic properties of molecular rotors in the solid state.

3.3.2 Experimental Section

Synthetic procedures

All the reagents and solvents were obtained from commercial sources and used as received.

$[(12\text{-crown-}4)_2(\text{DABCOH}_2)](\text{BF}_4)_2$ and $[(12\text{-crown-}4)_2(\text{DABCOH}_2)](\text{ClO}_4)_2$ were prepared according to the following general procedure: DABCO was dissolved in deionized water along with 2 equivalents of the crown ether. HBF_4 or HClO_4 was added dropwise until neutralization and after few hours a white solid precipitated from the solution. The solid was thus filtered and washed with ethanol. The bulk product was characterized by XRPD, while crystals suitable for single-crystal and high-pressure experiments were obtained by slow evaporation of a DMF solution.

High-pressure experiments

All the experiments were performed in a Merrill-Bassett diamond anvil cell (DAC) modified by supporting the anvils directly on steel discs with a conical window (type 1A diamonds, cutlet size 0.8 mm). Steel gaskets of thickness 0.25 mm were employed for $[(12\text{-crown-}4)_2(\text{DABCOH}_2)](\text{BF}_4)_2$, the diameter of the holes was 0.4 mm. Pressure in the DAC was calibrated by the ruby fluorescence method^{26,27} with a Photon Control spectrometer.

A single crystal of $[(12\text{-crown-}4)_2(\text{DABCOH}_2)](\text{BF}_4)_2$ was stuck on one anvil of the DAC with immersion oil, then the chamber was filled with Daphne oil, sealed and the pressure was increased in steps (see Figure 3.3.1). After every step crystal data were collected.

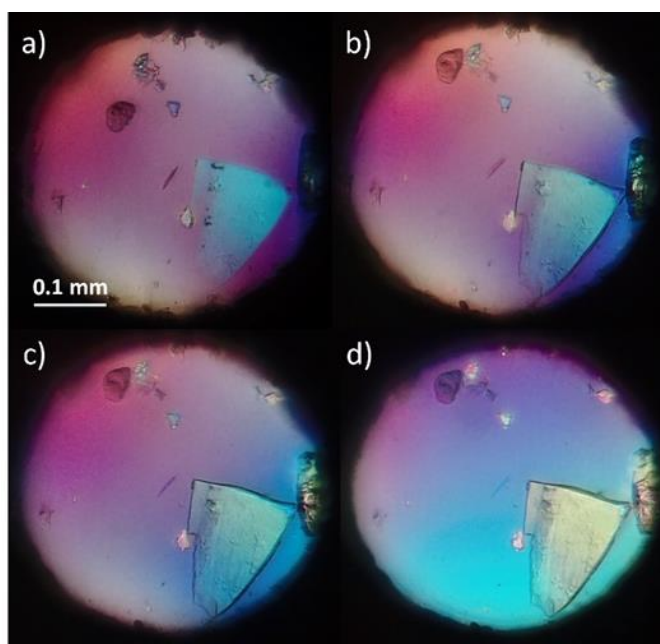


Figure 3.3.1 Stages of the isothermal compression of $[(12\text{-crown-}4)_2(\text{DABCOH}_2)](\text{BF}_4)_2$ in daphne oil (polarized-light optical microscope images): (a) 0.3 GPa, (b) 0.66 GPa, (c) 1.22 GPa and (d) 3 GPa.

Ambient pressure SCXRD

Single-crystal data for $[(12\text{-crown-}4)_2(\text{DABCOH}_2)](\text{BF}_4)_2$ and $[(12\text{-crown-}4)_2(\text{DABCOH}_2)](\text{ClO}_4)_2$ were collected on an Oxford X'Calibur S CCD diffractometer equipped with a graphite monochromator (Mo-K α radiation, $\lambda = 0.71073 \text{ \AA}$), and with a cryostat Oxford CryoStream800. The structures were solved by intrinsic phasing with SHELXT²⁸ and refined on F² by full-matrix least squares refinement with SHELXL implemented in Olex2 software.²⁹ The refinements against the room-temperature data were performed according to the following procedure: the DABCO C-atoms were split into three positions, whereas O and C-atoms of the crown ethers and F-atoms or Cl-atoms of the anions were split into two positions. Occupancies of all the conformations were refined independently for the anisotropic model and fixed upon convergence. Due to the high number of parameters, anisotropic refinements were performed applying EADP constraints to the thermal parameters of DABCO and crown ethers. Finally, H-atoms of the crown ethers and DABCO N-atoms were placed in calculated position and refined with a riding model. For low-temperature data, all non-H atoms were refined anisotropically, while H-atoms were placed in calculated position and refined with a riding model.

The crystal data and refinements details are summarized in Table SI-1 and Table SI-2 in paragraph 3.3.5

High-pressure SCXRD

The diffraction data were collected on a Kuma diffractometer with Mo K α radiation ($\lambda=0.71073$ Å) equipped with a CCD detector. CrysAlisPro 171.37.31 (Rigaku Oxford Diffraction. CrysAlisPro Software System version 171.39.46, Technol. UK Ltd., Yarnton, England.) was used for recording reflections³⁰ and preliminary data reduction. The intensities were corrected for the effects of DAC absorption, diamond diffraction and sample shadowing by the gasket.

The structural model of [(12-crown-4)₂(DABCOH₂)](BF₄)₂ obtained from the ambient-pressure 100K collection was refined against high-pressure data on F² by full-matrix least squares refinement with SHELXL implemented in Olex2 software.²⁹ Two disordered positions were assigned to the F-atoms of the BF₄⁻ anions; their occupancy refined in the anisotropic model and fixed for the anisotropic refinement. All non-H atoms were refined anisotropically. H-atoms were placed in calculated positions and refined with a riding model.

The crystal data and refinements details are summarized in Table SI-3, paragraph 3.3.5.

Powder XRD

For phase identification, X-ray powder diffraction diffractograms were collected on a PANalytical X'Pert Pro automated diffractometer equipped with an X'Celerator detector in Bragg–Brentano geometry, using Cu–K α radiation ($\lambda = 1.5418$ Å) without monochromator in the 2θ range between 3° and 50° (continuous scan mode, step size 0.0167°, counting time 19.685 s, Soller slit 0.04 rad, antiscatter slit ½, divergence slit ¼, 40 mA*40 kV). The program Mercury³¹ was used for simulation of X-ray powder patterns on the basis of single crystal data. In all cases, the identity between polycrystalline samples and single crystals was always verified by comparing experimental and simulated powder diffraction patterns (See Figures SI-4 and SI-5 in paragraph 3.3.5).

Thermal analyses

Calorimetric measurements were performed with a Perkin-Elmer DSC-7 equipped with a PII intracooler. Temperature and enthalpy calibrations were performed using high-purity standards (n-decane, benzene and indium). Heating of the aluminium open pans containing the samples (3–5 mg) was carried out at 5 °C min⁻¹ in the temperature range -30 – 200°C.

TGA analyses were performed with a Perkin-Elmer TGA-7. Each sample, contained in a platinum crucible, was heated in a nitrogen flow (20 cm³·min⁻¹) at a rate of 5°C min⁻¹, up to decomposition. Samples weights were in the range 5–10 mg.

Solid-state NMR

1D ¹³C MAS and ²H static SSNMR spectra were acquired on a Jeol ECZR 600 instrument, operating at 600.2, 150.9 and 92.1 MHz for the ¹H, ¹³C and ²H nuclei, respectively. Powder samples were packed in 3.2 mm diameter cylindrical zirconia rotors with a volume of 60 μL. A certain amount of sample was taken and used without further preparation from each batch to fill the rotor. ¹³C MAS spectra were acquired at a spinning speed of 20 kHz with a 90° ¹³C pulse of 2.15 μs, a recycle time of 20 s and 32 scans. The two-pulse phase modulation (TPPM) decoupling scheme with a 116.0 kHz radiofrequency field was used. ²H wide-line spectra were recorded with a 90° ²H pulse of 3.0 μs and 32 scans. To acquire the ²H wide-line spectra, a quadrupolar-echo pulse sequence with an echo delay of 5 μs and recycle delay of 5 s was employed. ¹³C chemical shifts were referenced to glycine (¹³C methylene signal at 43.5 ppm).

Variable-temperature operation was achieved by a triple gas channel MAS probe, in which the stream of VT gas is separated from the MAS bearing and driving gases. The driving gas is used to propel the rotor at high speeds, while the bearing gas provides an air cushion for stability. The low temperatures were achieved by cooling the VT line through a flow of boil-off N₂ gas from an exchange Dewar filled with liquid nitrogen. The VT gas was then directed at the mid-point of the sample rotor. For the high temperature operations, VT and MAS gases were air heated by means of a resistance put inside the probe.

A thermocouple was used for temperature measurement and regulation. The temperature was calibrated using the well-established method based on the ²⁰⁷Pb NMR resonance of solid Pb(NO₃)₂.^{32–35}

3.3.3 Results and Discussion

Crystal structures

$[(12\text{-crown-}4)_2(\text{DABCOH}_2)](\text{BF}_4)_2$ and $[(12\text{-crown-}4)_2(\text{DABCOH}_2)](\text{ClO}_4)_2$ are isomorphous; they crystallize in the trigonal enantiomeric space groups $P3_121$ or $P3_221$ and form colorless block-like crystals. The crystal packing is defined by the repetition of discrete units comprising a doubly-protonated DABCO molecule coordinating two crown-ethers as represented in Figure 3.3.2. Coordination is achieved through charged-assisted N-H \cdots O hydrogen bonds, additionally, each DABCOH_2^{2+} cation is surrounded by four anions (see Figure 3.3.2 and Table SI-4 for a list of the distances).

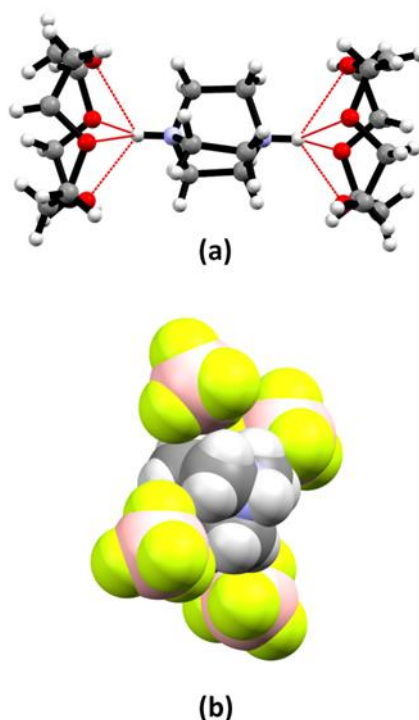


Figure 3.3.2 (a) The discrete unit $(12\text{-crown-}4)_2(\text{DABCOH}_2)$ in the crystals of $[(12\text{-crown-}4)_2(\text{DABCOH}_2)](\text{BF}_4)_2$ and $[(12\text{-crown-}4)_2(\text{DABCOH}_2)](\text{ClO}_4)_2$; (b) representation of the DABCOH_2^{2+} cation surrounded by four BF_4^- anions.

All the components at room temperature are disordered. The anions are characterized by an almost plastic behaviour, making the precise identification of the atomic positions quite difficult. The DABCOH_2^{2+} cations exhibit disorder

of the C-atoms, likely due to the motion of the dication around its pseudo-threefold axis. Three crystallographically non-equivalent positions were refined for each C-atom; in both cases, one of those partitions accounted for a higher occupancy (40-50%). The crown ethers show a conformational disorder that is typical of the up/down CH₂ flip motion³⁶ (Figure 3.3.3b), except here as well the occupancy of the two conformations is not evenly distributed; the ratio is approximately 70/30 in [(12-crown-4)₂(DABCOH₂)](BF₄)₂ and 65/35 in [(12-crown-4)₂(DABCOH₂)](ClO₄)₂.

The adoption of a chiral space group is noteworthy since the building blocks are not intrinsically chiral, furthermore, they are highly disordered, so one would expect the non-centrosymmetric features to be eliminated by the disorder. The 12-crown-4 ether in its pseudo-C₄ conformation possesses a set of C-atoms that are closer to the O-atom plane and another that is farther, the two positions can be termed “up” and “down” (Figure 3.3.3b). The four repeating O-C-C units have a regular u-d-u-d sequence, so the resulting form is chiral being either right-handed or left-handed. Normally, the chirality is removed by the fast up/down CH₂ flip motion that reverse the handedness, creating a centro-symmetric spatial average. Here the different occupancy of the two conformations could account for the crystallization in a chiral structure. The relation between the molecular self-assembly and the symmetry elements, however, is not straightforward; the “spools” defined by a (12-crown-4)₂(DABCOH₂) unit are piled along the 3₁ or 3₂ axis with the pseudo-threefold axis of the DABCOH₂²⁺ transversal to the screw axis, as represented in Figure 3.3.3c.

Low temperature data were collected at 200K and 100K. The space group is conserved throughout the entire temperature range, and no phase transitions were detected in the attainable range from DSC measurements (see Figure SI-8 and SI-9 in paragraph 3.3.5). At 200K and 100K, the DABCOH₂²⁺ cations undergo partial ordering: distinct split positions for the C-atoms were not easily identified from the electron density, even though the ellipsoids still show elongation along the tangential direction, thus suggesting a dynamic process (see Figure SI-2). Similar considerations can be made for the anions, except split positions for the F atoms could be refined at 200K that account for roughly 15-20% of the occupancy.

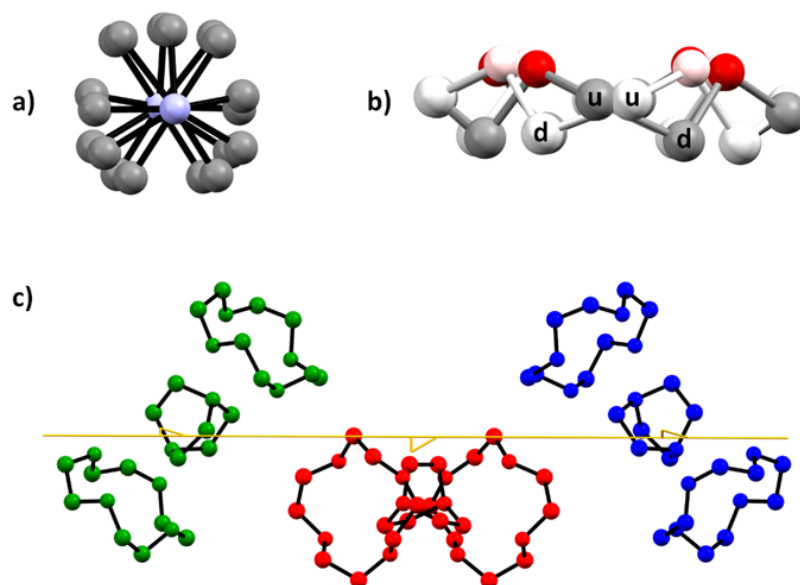


Figure 3.3.3 (a) Ball and stick model of the disordered positions of the DABCOH_2^{2+} cation observed in the RT structure (H-atoms omitted for clarity); (b) the two conformations of the 12-crown-4 ether; (c) disposition of the $(12\text{-crown-4})_2(\text{DABCOH}_2)$ units along the 3_1 axis, each independent unit is depicted in a different color.

The crown ethers at low temperature show traces of disorder, however, the electron density accounting for the enantiomeric conformation is significantly lower (<8% occupancy), so that the refinement of the independent positions was unsuccessful. This observation suggests that the 70/30 ratio in the occupancy for the two conformations obtained at RT is related to the dynamic CH_2 flip motion rather than the intrinsic enantiopurity of the crystal, interestingly the ratio is restored after going back to RT. Buchanan and coworkers estimated the activation energy for this motion at 0.85 kJ/mol;³⁷ in view of this, it is remarkable that the flip motion takes place to such a limited extent even at room temperature.

Solid State NMR – Dynamics

Prompted by these findings, we performed solid state NMR measurements to study the dynamics. ^{13}C MAS spectra of $[(12\text{-crown-4})_2\cdot\text{DABCOH}_2](\text{ClO}_4)_2$ and $[(12\text{-crown-4})_2\cdot\text{DABCOH}_2](\text{BF}_4)_2$ at room temperature (Figure 3.3.4) show two signals at 45.5 and 65.2 ppm assigned to the $-\text{CH}_2$ groups of $(\text{DABCOH}_2)^{2+}$ and 12-crown-4 ether, respectively.

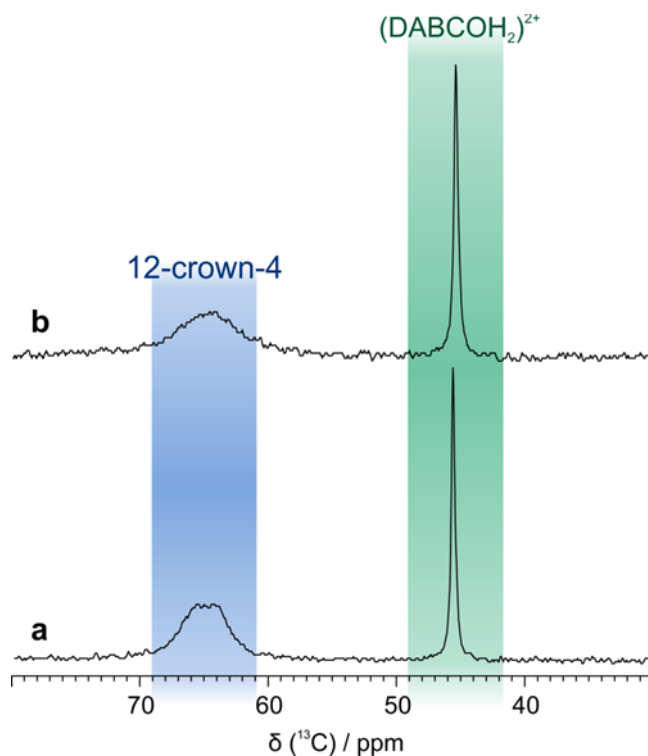


Figure 3.3.4 Room temperature ^{13}C (150.9 MHz) MAS SSNMR spectra of (a) [(12-crown-4) $_2$ ·DABCOH $_2$](ClO $_4$) $_2$ and (b) [(12-crown-4) $_2$ ·DABCOH $_2$](BF $_4$) $_2$, acquired at a spinning speed of 20 kHz.

To understand the dynamic processes present in the supramolecular salts, variable temperature (VT) NMR measurements were performed. ^{13}C MAS spectra of [(12-crown-4) $_2$ ·DABCOH $_2$](ClO $_4$) $_2$ obtained at different temperature values, from 213 to 353 K, are reported in Figure 3.3.5.

By changing the temperature, the (DABCOH $_2$) $^{2+}$ signal does not show any difference. This is due to the well-known rotation of DABCO unit along its *pseudo*-three-fold axis, which is associated with very low activation energy.^{38,39} Such motion cannot be frozen at the lowest achievable NMR temperature and thus its effect is not observed in the ^{13}C MAS spectra. On the other hand, the signal at higher ppm shows two different resonances (64.3 and 65.8 ppm) at high temperatures, which then coalesce and merge into one as the temperature is lowered. The coalescence temperature is around 293 K and an activation energy of 58.4 kJ/mol evaluated by lineshape analysis is obtained.

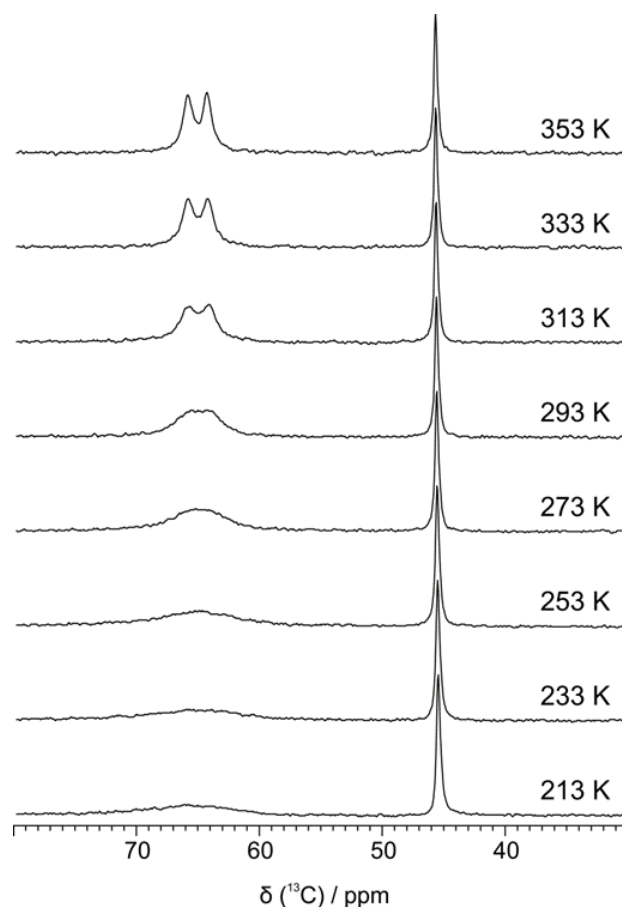


Figure 3.3.5 VT ^{13}C (150.9 MHz) MAS SSNMR spectra of $[(12\text{-crown-}4)_2\cdot\text{DABCOH}_2](\text{ClO}_4)_2$ acquired at a spinning speed of 20 kHz.

We surmise that the difference in the CH_2 resonances at high temperature is probably due to the *pseudo*-four-fold rotational jumps of the ether ring. In agreement with the X-ray data, at high temperature the proton atoms of some CH_2 groups of the ether lie in-plane with respect to the ring whereas some others lie out-of-plane, causing a different environment and thus a differentiation in chemical shifts, that is not averaged by the up/down CH_2 flip motion; this confirms that the flip motion must be slow on the NMR timescale. At low temperature, the rotation of the ether is slowed down and the signal becomes broader. This is possibly due to the overlap of different resonances very similar in chemical shift assigned to each CH_2 group of the ether. Reasonably, if lower temperatures might be reached, the broad signal at 65.2 ppm would split in more resonances, one for each CH_2 group.

The same behavior is observed for $[(12\text{-crown-}4)_2\cdot\text{DABCOH}_2](\text{BF}_4)_2$, for which higher activation energy is found (Figure SI-6, paragraph 3.3.5).

To get deeper insights into the dynamic, a wide-line quadrupolar echo ^2H NMR analysis was carried out on the synthesized deuterium analogous of [(12-crown-4) $_2$ ·DABCOH $_2$](ClO $_4$) $_2$, prepared by perdeuterated DABCO. In fact, it is well-known that ^2H lineshape is highly affected from different kind of motion and thus is considered a valuable tool to investigate dynamics. Figure 3.3.6 shows the VT wide-line ^2H SSNMR spectra in the 193-293 K range; however, no appreciable change in the lineshape is observed. This is in good agreement with the very low activation energy associated with the high rotational frequencies of the DABCO unit around its principal axis, already discussed above. This motion is therefore confirmed to be the only dynamic process present in the supramolecular salt, involving the DABCO unit.

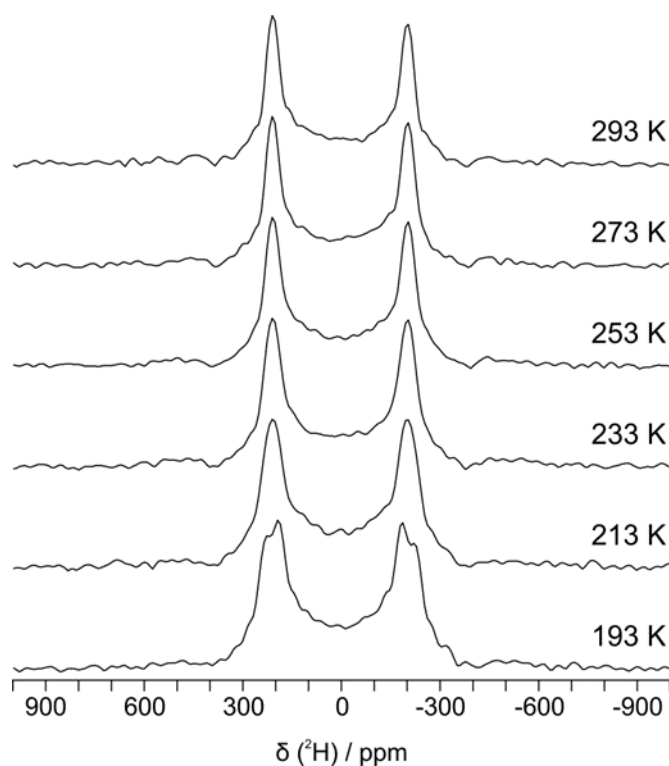


Figure 3.3.6 VT wide-line ^2H (92.1 MHz) SSNMR spectra of [(12-crown-4) $_2$ ·DABCOH $_2$](ClO $_4$) $_2$ acquired under static condition.

High-pressure experiments

Crystals of [(12-crown-4) $_2$ ·DABCOH $_2$](BF $_4$) $_2$ were compressed at isothermal conditions and the structural changes were monitored by single-crystal XRD. A comparison of the relative compression of the unit cell parameters with increasing pressure and decreasing temperature shows that the same level of

compression observed at 100 K is achieved already at 0.3 GPa (see Figure 3.3.7). However, a qualitative analysis of the thermal parameters of the high-pressure structures in comparison with the 100 K structural model reveals a completely different situation (see also Figure SI-2 and SI-3). The ellipsoids of the DABCO C-atoms are markedly elongated along the tangential direction, suggesting that the rotational motion is retained. Disordered positions for the crown ethers could be traced in the electron density residuals, however, the refinement of the distinct positions of the two enantiomeric conformations was unsuccessful.

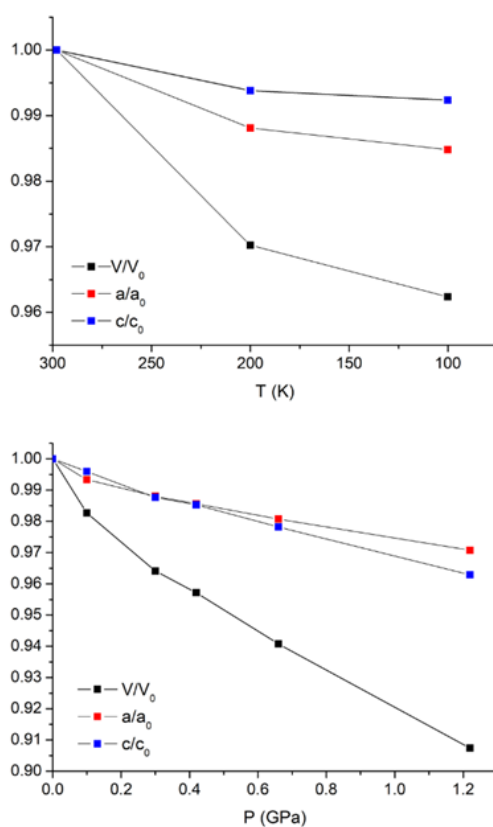


Figure 3.3.7 Relative compression of the cell parameters of [(12-crown-4)₂·DABCOH₂](BF₄)₂ as a function of temperature (top) and pressure (bottom).

Relevant intermolecular distances were monitored as a function of pressure. Given the disorder affecting the structures, the choice was made as explained in the following to ensure that comparable values could be extrapolated in the different experimental conditions. To probe the surroundings of the DABCOH₂²⁺ cations, N-H···O bonds with the crown ether and the distance between the DABCO centroid along the N-N axis and the B-

atom of the anions were selected. The distance between crown ethers was monitored through the O...O distance of neighboring rings; every ether is indeed surrounded by other four molecules of crown ether, as described in Scheme SI-1 (paragraph 3.3.5), two lay in the same plane in antiparallel fashion and two are perpendicular to the O-atom plane.

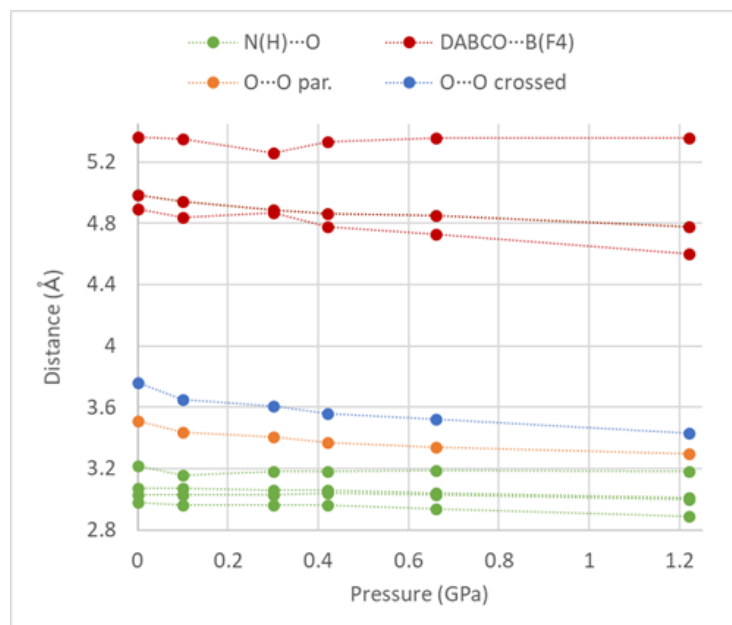


Figure 3.3.8 Intermolecular distances of $[(12\text{-crown-}4)_2\text{-DABCOH}_2](\text{BF}_4)_2$ as a function of pressure (cfr. Scheme SI-1 and Table SI-4).

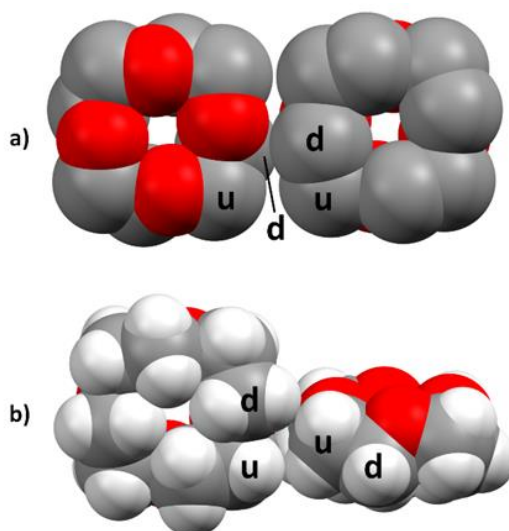


Figure 3.3.9 Spacefill structure (0.42 GPa) of the neighboring crown ethers in an antiparallel arrangement (a) and “crossed” arrangement (b); H-atoms are omitted in (a) for clarity.

The results are summarized in Table SI-4 and figure 3.3.8. Interestingly, the N-H...O bonds are roughly unaltered both at low temperature and pressure up to 1.2 GPa, coherently to the fast dynamics established by the NMR analysis. Of the four anions surrounding every DABCOH₂²⁺ cation one has a significantly longer distance. This is expected to be less interacting with the cation and its distance shows a pronounced discontinuity: it is reduced up to 0.3 GPa and grows again at higher pressure. Notably, the space group symmetry is conserved upon displacement of the anions. Finally, the distance between neighboring crown ethers is reduced both at low temperature and high pressure, as expected since they are the bulkiest building blocks; however, the thermal parameters at 0.66 GPa do not hint at any significant reduction in the dynamics (see Figure SI-2).

We suggest therefore that the rotational motions are conserved within the crystal packing thanks to their correlation. It is evident from Figure 3.3.9a that the conformations of the antiparallel crown ethers are correlated: an exchange of the up/down positions of one of the two molecules would be impossible without a structural rearrangement for steric reasons; the two molecules are thus locked and must rotate in a concerted manner. Similarly, the steric hindrance of the C-H groups in the "crossed" arrangement (Figure 3.3.9b) would obstruct the rotation of one ether if the other one was stationary. In this picture, the chiral 12-crown-4 ethers can be compared from the functionality standpoint to spiral gears, that must possess matching handedness in order to mesh. This could account for the finding that the CH₂ flip motion is strongly hindered since an inversion of the handedness of one ether must be concomitant with the inversion of the ethers meshed with it, as depicted in Figure 3.3.10, which is statistically less likely to happen.

At higher pressure than 1.22 GPa, the quality of the diffraction data decreases dramatically so that it is impossible to obtain a reliable structural model. Macroscopically, the crystals maintain their integrity up to 3 GPa, as showed in Figure 3.3.1, however, the data are not consistent with the hexagonal lattice of the ambient pressure phase. We speculate that this behavior is due to a collapse-type transition, when the crystal reduces its volume by a shear strain, reducing the crystal symmetry. From the lattice strain, it can be inferred that most likely the structure orders and the "framework" collapses to fill the empty space left due to the ordering. The usual mechanism consists in intermolecular interactions becoming stronger, as the stress is passed on through the structure, which dampens the

rota/vibrations of molecules to their full stop and the consequent reduction of the symmetry to a monoclinic or triclinic lattice. This mechanism implies the bending of at least one of the unit cell angles, that could take place with equal probability in 4 or more directions, originating twinned domains on the micro-to nano-scale that cause an overall lowering of the long-range order hampering structure solution.

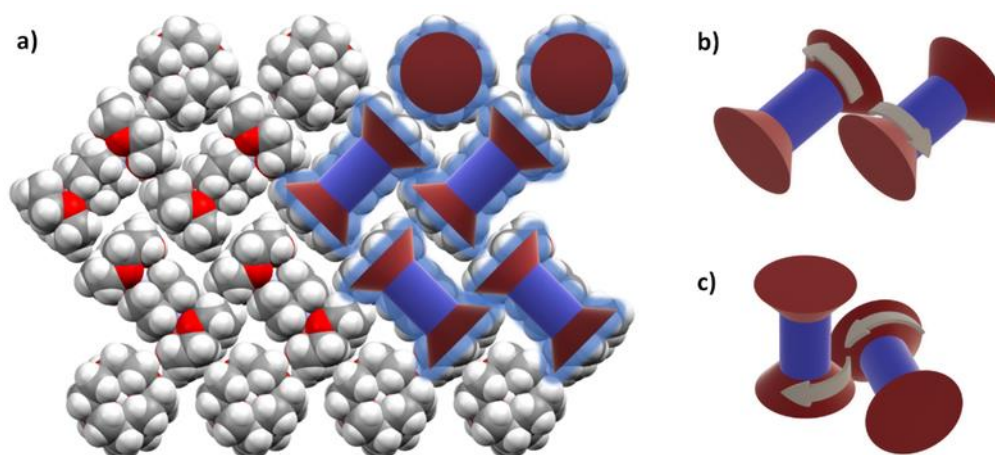


Figure 3.3.10 Crystal packing of the (12-crown-4)₂·DABCOH₂ units (a) highlighting correlation between adjacent crown ethers (anions omitted for clarity) and schematics of the proposed geared motion between antiparallel (b) and perpendicular (c) ethers.

3.3.4 Conclusions

Crystals possessing components in rapid motion are at the forefront of the research on solid-state molecular machines. The common approach envisages the modification of the molecular dynamics by acting on the thermal parameters alone. The final goal would be the development of stimuli-responsive materials based on molecular rotors. In view of this, it would be highly desirable to be able to utilize also mechanical parameters, namely pressure and volume, to control motion on the molecular scale. With this in mind, we have reported here the results of our studies on the solid-state dynamics of the supramolecular salts of general formula [(12-crown-4)₂·DABCOH₂](X)₂ (where X=BF₄, ClO₄), as a function of temperature and pressure, through the combination of X-ray diffraction and solid-state NMR spectroscopy. To the best of these authors' knowledge, this is the first time that the effect of pressure is deliberately investigated in the context of artificial molecular rotors.

The salts $[(12\text{-crown-}4)_2\text{DABCOH}_2](X)_2$ are isostructural and crystallize in the non-centrosymmetric space groups $P3_221$ and $P3_121$. All the building blocks composing the supramolecular complex display rotational processes at ambient temperature and pressure; surprisingly, however, the interconversion between the two enantiomerically-related conformations of the crown ethers is strongly hampered, accounting for the lack of an inversion center. Whereas the dynamics of the crown ethers are attenuated at low temperature through a monotonic thermal compression of the lattice, the structural disorder of the salts is substantially unaffected upon monotonic pressure-induced compression.

We have argued that the motion of the crown ethers is conserved thanks to the correlation between neighboring molecules that mesh and rotate in a concerted manner similarly to spiral gears, with pressure acting as the mean to couple and decouple the gears. At higher pressure than roughly 1.2 GPa, the experimental evidence are consistent with a collapse-type transition to an ordered structure with lower symmetry, that could not be obtained at a temperature as low as 100K, providing further confirmation that the inverse relation between temperature and pressure effects in solids does not hold.

3.3.5 Supporting Information

Single-crystal XRD

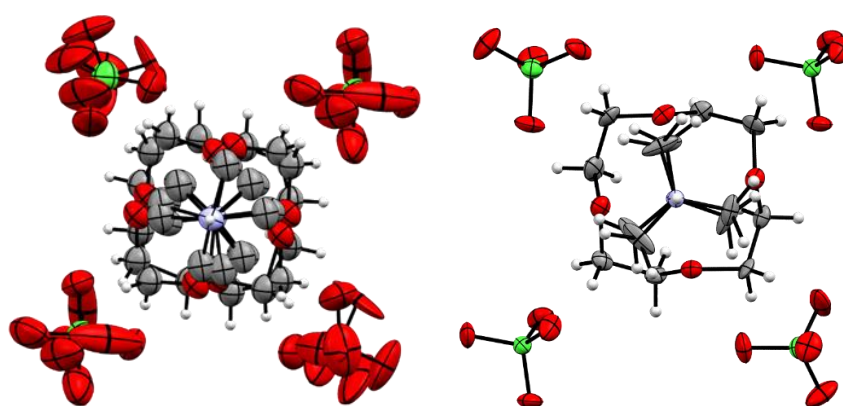


Figure SI-1 Ortep drawings (50% probability) of $[(12\text{-crown-}4)_2\text{DABCOH}_2](\text{ClO}_4)_2$ at room temperature (left) and at 100 K (right) at ambient pressure.



Figure SI-2 Variable-temperature Ortep drawings (50% probability) of [(12-crown-4)₂·DABCOH₂](BF₄)₂.

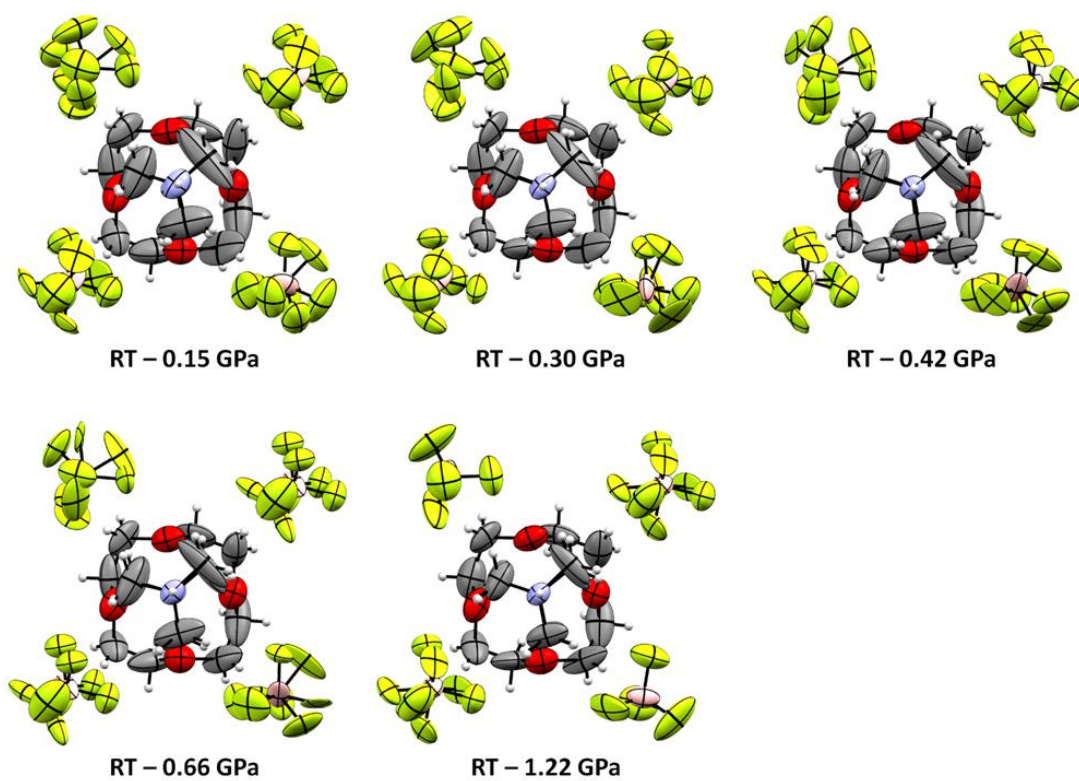


Figure SI-3 Variable-pressure Ortep drawings (50% probability) of [(12-crown-4)₂·DABCOH₂](BF₄)₂.

Table SI-1 Crystallographic data table of the compound [(12-crown-4)₂·DABCOH₂](ClO₄)₂.

	[(12-crown-4) ₂ ·DABCOH ₂](ClO ₄) ₂	[(12-crown-4) ₂ ·DABCOH ₂](ClO ₄) ₂
Empirical formula	C ₂₂ H ₄₄ Cl ₂ N ₂ O ₁₆	C ₂₂ H ₄₄ Cl ₂ N ₂ O ₁₆
Formula weight	663.49	663.49
Temperature/K	300	100
Crystal system	trigonal	trigonal
Space group	P3 ₁ 21	P3 ₁ 21
a/Å	10.3187(8)	10.1674(5)
b/Å	10.3187(8)	10.1674(5)
c/Å	25.2248(17)	25.0181(13)
α/°	90	90
β/°	90	90
γ/°	120	120
Volume/Å ³	2326.0(4)	2239.8(2)
Z	3	3
ρ _{calc} /cm ³	1.399	1.476
μ/mm ⁻¹	0.282	0.294
F(000)	1026.0	1056.0
Radiation	MoKα (λ = 0.71073)	MoKα (λ = 0.71073)
2θ range for data collection/°	6.654 to 58.322	6.73 to 49.962
Index ranges	-13 ≤ h ≤ 12, -11 ≤ k ≤ 11, -33 ≤ l ≤ 29	-12 ≤ h ≤ 8, -7 ≤ k ≤ 12, -29 ≤ l ≤ 29
Reflections collected	5909	9429
Independent reflections	3437 [R _{int} = 0.0213, R _{sigma} = 0.0477]	2627 [R _{int} = 0.0307, R _{sigma} = 0.0310]
Data/restraints/parameters	3437/48/209	2627/0/191
Goodness-of-fit on F ²	1.249	1.177
Final R indexes [I ≥ 2σ (I)]	R ₁ = 0.1242, wR ₂ = 0.3303	R ₁ = 0.0612, wR ₂ = 0.1708
Final R indexes [all data]	R ₁ = 0.1682, wR ₂ = 0.3672	R ₁ = 0.0651, wR ₂ = 0.1732
Largest diff. peak/hole / e Å ⁻³	0.45/-0.35	0.62/-0.39

Table SI-2 Crystallographic data table of compound [(12-crown-4)₂·DABCOH₂](BF₄)₂.

	[(12-crown-4)₂·DABCOH₂](BF₄)₂	[(12-crown-4)₂·DABCOH₂](BF₄)₂	[(12-crown-4)₂·DABCOH₂](BF₄)₂
Empirical formula	C ₂₂ H ₄₆ B ₂ F ₈ N ₂ O ₈	C ₂₂ H ₄₆ B ₂ F ₈ N ₂ O ₈	C ₂₂ H ₄₆ B ₂ F ₈ N ₂ O ₈
Formula weight	640.23	640.23	640.23
Temperature/K	300	200	100
Crystal system	trigonal	trigonal	trigonal
Space group	P3 ₁ 21	P3 ₁ 21	P3 ₂ 21
a/Å	10.2541(6)	10.1319(9)	10.0981(6)
b/Å	10.2541(6)	10.1319(9)	10.0981(6)
c/Å	25.0361(14)	24.881(2)	24.8445(15)
α/°	90	90	90
β/°	90	90	90
γ/°	120	120	120
Volume/Å ³	2279.8(3)	2211.9(4)	2194.0(3)
Z	3	3	3
ρ _{calc} /cm ³	1.359	1.435	1.454
μ/mm ⁻¹	0.130	0.135	0.138
F(000)	966.0	1010.0	1014.0
Radiation	MoKα (λ = 0.71073)	MoKα (λ = 0.71073)	MoKα (λ = 0.71073)
2θ range for data collection/°	6.7 to 59.046	6.76 to 49.976	6.776 to 51.958
Index ranges	-13 ≤ h ≤ 12, -14 ≤ k ≤ 11, -29 ≤ l ≤ 31	-12 ≤ h ≤ 9, -10 ≤ k ≤ 6, -29 ≤ l ≤ 19	-12 ≤ h ≤ 12, -10 ≤ k ≤ 11, -30 ≤ l ≤ 18
Reflections collected	10971	4452	4887
Independent reflections	3567 [R _{int} = 0.0525, R _{sigma} = 0.0629]	2565 [R _{int} = 0.0229, R _{sigma} = 0.0444]	2864 [R _{int} = 0.0280, R _{sigma} = 0.0626]
Data/restraints/parameters	3567/76/211	2565/24/227	2864/0/191
Goodness-of-fit on F ²	1.166	1.068	1.050
Final R indexes [I ≥ 2σ (I)]	R ₁ = 0.1267, wR ₂ = 0.3232	R ₁ = 0.0682, wR ₂ = 0.1632	R ₁ = 0.0691, wR ₂ = 0.1636
Final R indexes [all data]	R ₁ = 0.2056, wR ₂ = 0.3795	R ₁ = 0.0784, wR ₂ = 0.1707	R ₁ = 0.0910, wR ₂ = 0.1758
Largest diff. peak/hole / e Å ⁻³	0.50/-0.31	0.45/-0.22	0.58/-0.27

Table SI-3 Crystallographic data table of the high-pressure collections of compound [(12-crown-4)₂DABCOH₂](BF₄)₂.

	[(12-crown-4) ₂ DABCOH ₂](BF ₄) ₂				
Empirical formula	C ₂₂ H ₄₆ B ₂ F ₈ N ₂ O ₈	C ₂₂ H ₄₆ B ₂ F ₈ N ₂ O ₈	C ₂₂ H ₄₆ B ₂ F ₈ N ₂ O ₈	C ₂₂ H ₄₆ B ₂ F ₈ N ₂ O ₈	C ₂₂ H ₄₆ B ₂ F ₈ N ₂ O ₈
Formula weight	640.23	640.23	640.23	640.23	640.23
Pressure/GPa	0.10	0.30	0.42	0.66	1.22
Crystal system	trigonal	trigonal	trigonal	trigonal	trigonal
Space group	P ₃ ₂ 21				
a/Å	10.186(2)	10.1310(14)	10.1069(16)	10.0564(13)	9.9543(11)
b/Å	10.186(2)	10.1310(14)	10.1069(16)	10.0564(13)	9.9543(11)
c/Å	24.934(4)	24.727(2)	24.667(3)	24.490(2)	24.1063(18)
α/°	90	90	90	90	90
β/°	90	90	90	90	90
γ/°	120	120	120	120	120
Volume/Å ³	2240.3(10)	2197.9(6)	2182.1(7)	2144.8(6)	2068.6(5)
Z	3	3	3	3	3
ρ _{calc} /g/cm ³	1.424	1.451	1.462	1.487	1.542
μ/mm ⁻¹	0.135	0.137	0.138	0.141	0.146
F(000)	1014.0	1014.0	1014.0	1014.0	1014.0
Crystal size/mm ³	0.274 × 0.188 × 0.051	0.274 × 0.188 × 0.051	0.274 × 0.188 × 0.051	0.274 × 0.188 × 0.051	0.274 × 0.188 × 0.051
Radiation	MoKα (λ = 0.71073)				
2θ range for data collection/°	8.006 to 54.064	8.064 to 54.578	8.084 to 54.598	8.138 to 55.112	8.252 to 54.626
Index ranges	-7 ≤ h ≤ 7, -7 ≤ k ≤ 7, -31 ≤ l ≤ 31	-7 ≤ h ≤ 7, -7 ≤ k ≤ 7, -30 ≤ l ≤ 31	-7 ≤ h ≤ 7, -12 ≤ k ≤ 12, -31 ≤ l ≤ 31	-12 ≤ h ≤ 12, -6 ≤ k ≤ 6, -31 ≤ l ≤ 31	-7 ≤ h ≤ 7, -6 ≤ k ≤ 6, -30 ≤ l ≤ 31
Reflections collected	9499	9464	8495	9469	9090
Independent reflections	1670 [R _{int} = 0.1324, R _{sigma} = 0.1463]	1640 [R _{int} = 0.1246, R _{sigma} = 0.1285]	1604 [R _{int} = 0.1125, R _{sigma} = 0.1330]	1490 [R _{int} = 0.1178, R _{sigma} = 0.1135]	1431 [R _{int} = 0.1127, R _{sigma} = 0.1106]
Data/restraints/parameters	1670/48/227	1640/36/227	1604/30/227	1490/12/221	1431/12/209
Goodness-of-fit on F ²	1.027	1.015	1.054	1.042	1.086
Final R indexes [I ≥ 2σ (I)]	R ₁ = 0.0816, wR ₂ = 0.0986	R ₁ = 0.0750, wR ₂ = 0.1337	R ₁ = 0.0760, wR ₂ = 0.1022	R ₁ = 0.0681, wR ₂ = 0.0893	R ₁ = 0.0763, wR ₂ = 0.1326
Final R indexes [all data]	R ₁ = 0.2363, wR ₂ = 0.1352	R ₁ = 0.2203, wR ₂ = 0.1794	R ₁ = 0.2153, wR ₂ = 0.1363	R ₁ = 0.1901, wR ₂ = 0.1172	R ₁ = 0.1873, wR ₂ = 0.1696
Largest diff. peak/hole / e Å ⁻³	0.14/-0.12	0.15/-0.14	0.18/-0.13	0.17/-0.14	0.17/-0.19

Scheme SI-1 Intermolecular distances used as a reference in the crystal structure of [(12-crown-4)₂·DABCOH₂](BF₄)₂ (H-atoms omitted for clarity); (a) hydrogen bonds between DABCOH₂²⁺ and crown ethers, distances between the DABCO centroid and the anions; (b) distances between adjacent crown ethers in parallel and crossed arrangement, note that the parallel ones are equivalent by symmetry.

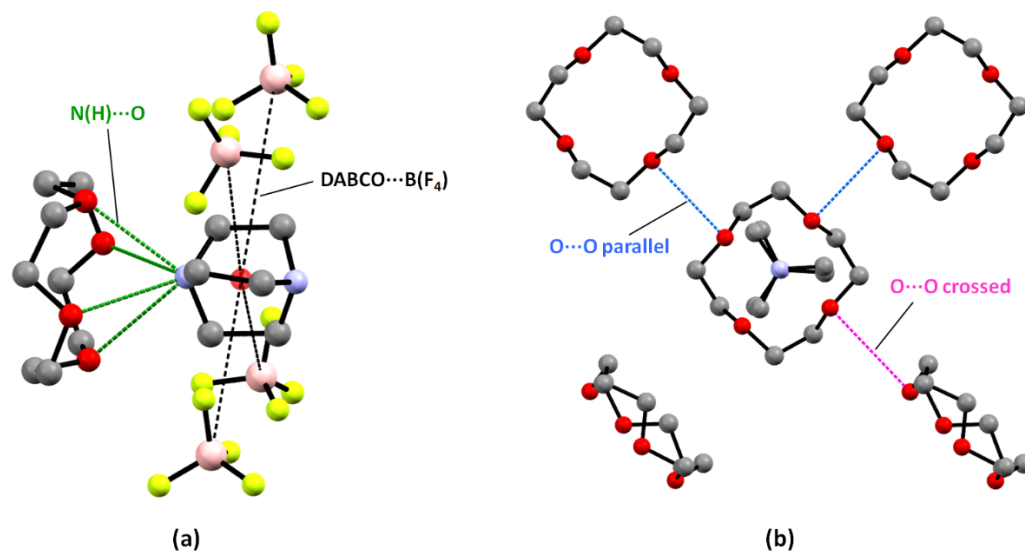


Table SI-4 List of intermolecular distances as a function of T in the crystal structure of [(12-crown-4)₂·DABCOH₂](BF₄)₂; see Scheme SI-1 for the definition of the distances.

	d(Å)		
N(H)···O	3.26(3)	3.200(6)	3.198(5)
	3.17(1)	3.082(7)	3.092(4)
	3.081(9)	3.051(6)	3.019(6)
	3.05(1)	2.935(8)	2.905(6)
	3.04(2)		
	3.01(2)		
	3.00(2)		
	2.965(7)		
	DABCO···B(F₄)	5.359	5.401
	4.982	4.899	4.878
	4.895	4.731	4.878
	4.982	4.898	4.716
O···O par.	3.51(4)	3.380(5)	3.355(7)
	3.51(1)		
O···O crossed	3.81(3)	3.678(6)	3.664(5)
	3.71(3)		
T	300 K	200 K	100 K

Table SI-5 List of intermolecular distances as a function of P in the crystal structure of [(12-crown-4)₂DABCOH₂](BF₄)₂; see Scheme SI-1 for the definition of the distances.

	d (Å)					
N(H)···O	3.26(3)	3.16(1)	3.18(1)	3.18(1)	3.19(1)	3.18(1)
	3.17(1)	3.07(2)	3.06(1)	3.06(2)	3.04(2)	3.01(2)
	3.081(9)	3.03(2)	3.03(1)	3.04(2)	3.03(1)	3.00(1)
	3.05(1)	2.96(2)	2.96(2)	2.96(2)	2.94(2)	2.89(2)
	3.04(2)					
	3.01(2)					
	3.00(2)					
DABCO···B(F₄)	2.965(7)					
	5.359	5.348	5.261	5.331	5.354	5.356
	4.982	4.940	4.889	4.864	4.851	4.776
	4.982	4.940	4.889	4.864	4.850	4.777
O···O par.	4.895	4.838	4.870	4.776	4.730	4.598
	3.51(4)	3.44(2)	3.41(2)	3.37(2)	3.34(1)	3.30(2)
O···O crossed	3.51(1)					
	3.81(3)	3.65(2)	3.61(1)	3.56(1)	3.52(1)	3.43(1)
	3.71(3)					
P	ambient	0.10 GPa	0.30 GPa	0.42 GPa	0.66 GPa	1.22 GPa

Powder XRD

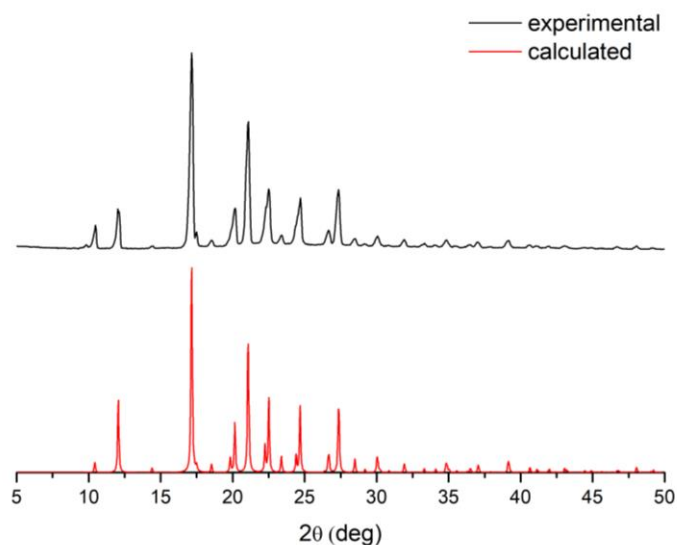


Figure SI-4 Comparison between the experimental and calculated pattern of [(12-crown-4)₂DABCOH₂](BF₄)₂.

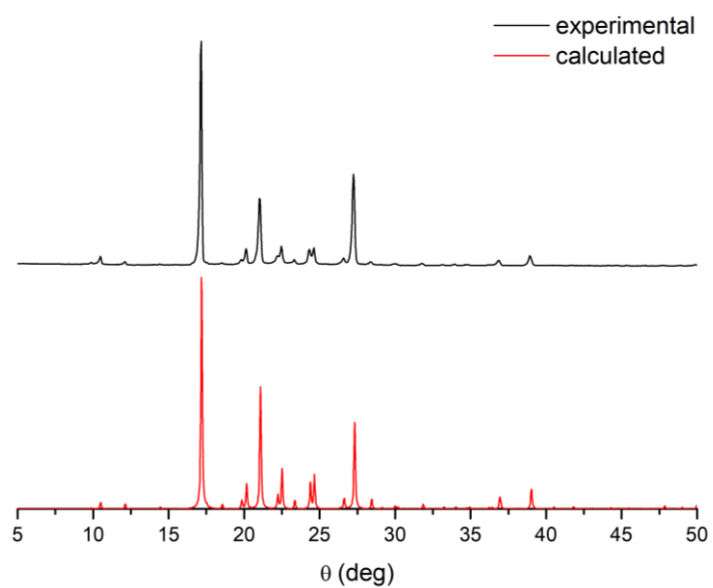


Figure SI-5 Comparison between the experimental and calculated pattern of [(12-crown-4)₂·DABCOH₂](ClO₄)₂.

Solid-state NMR spectroscopy

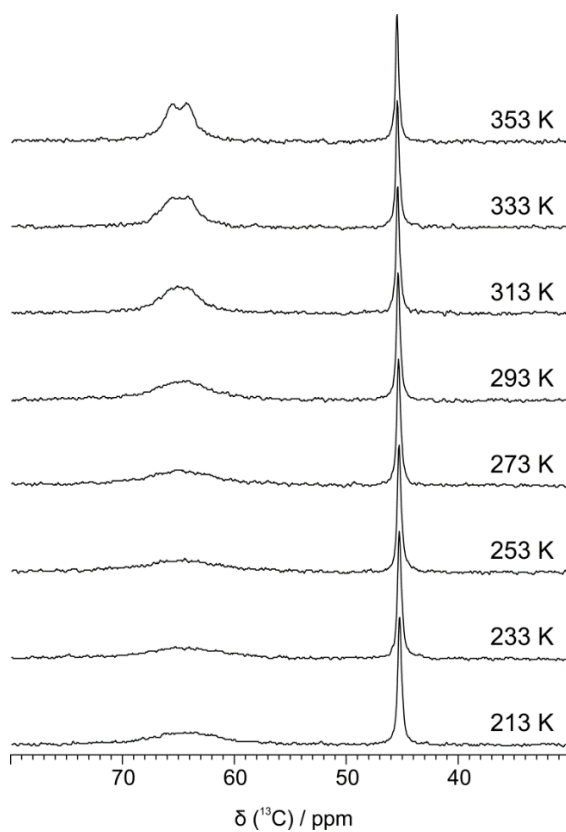


Figure SI-6 VT ¹³C (150.9 MHz) MAS SSNMR spectra of [(12-crown-4)₂·DABCOH₂](BF₄)₂ acquired at a spinning speed of 20 kHz.

Thermal analyses

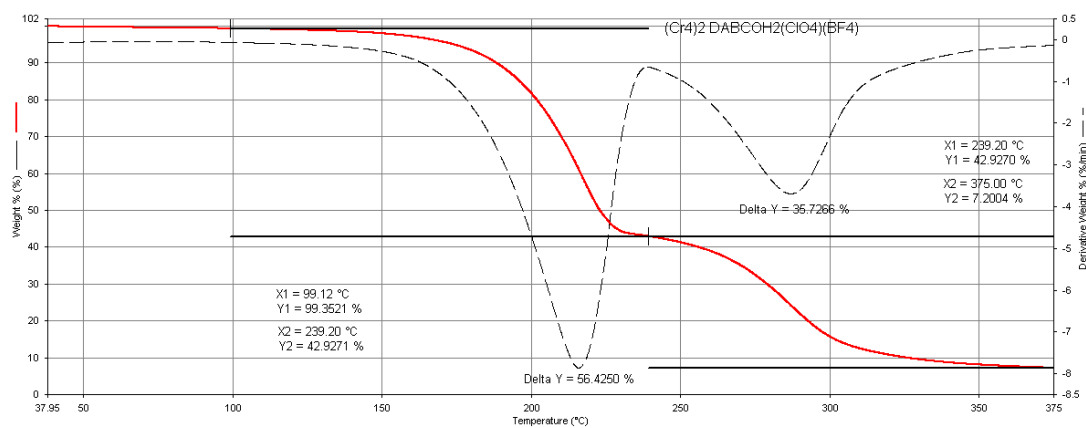


Figure SI-7 TGA track of $[(12\text{-crown-}4)_2\cdot\text{DABCOH}_2](\text{BF}_4)_2$.

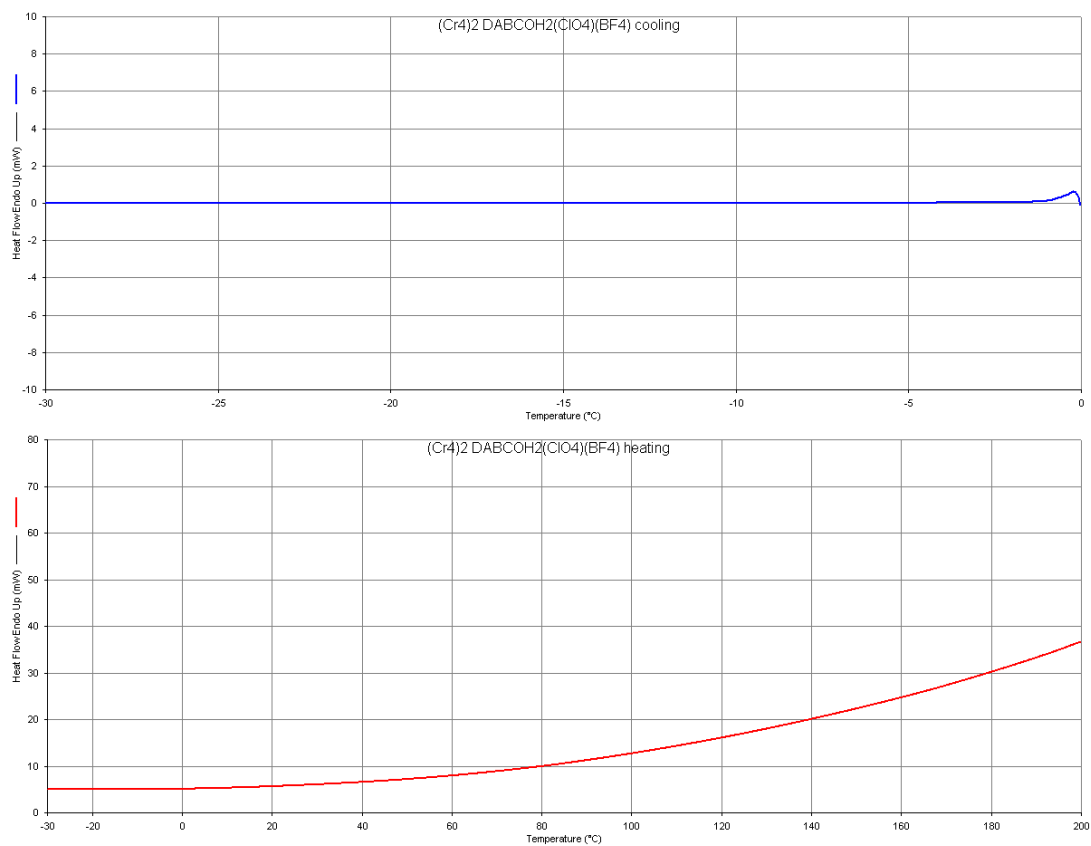


Figure SI-8 DSC track of $[(12\text{-crown-}4)_2\cdot\text{DABCOH}_2](\text{BF}_4)_2$; cooling (top) and heating ramp (bottom).

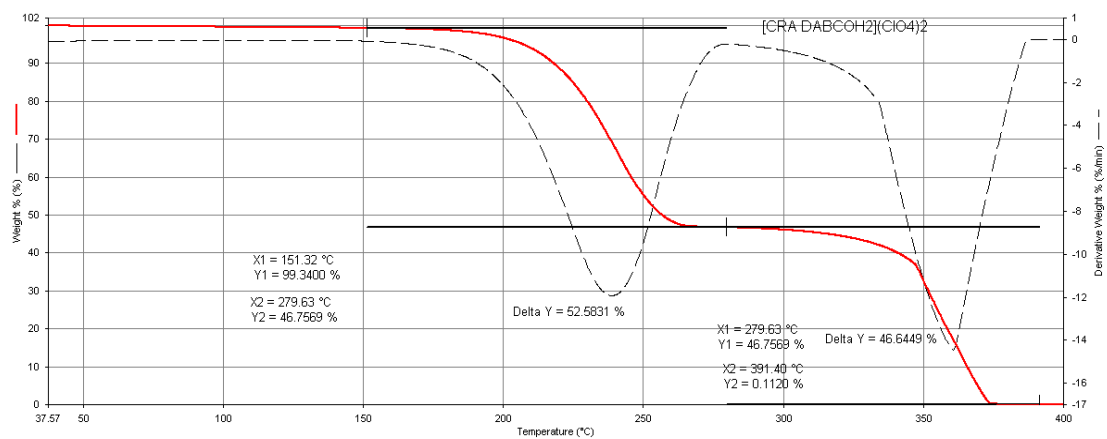


Figure SI-9 TGA track of [(12-crown-4)₂-DABCOH₂](ClO₄)₂.

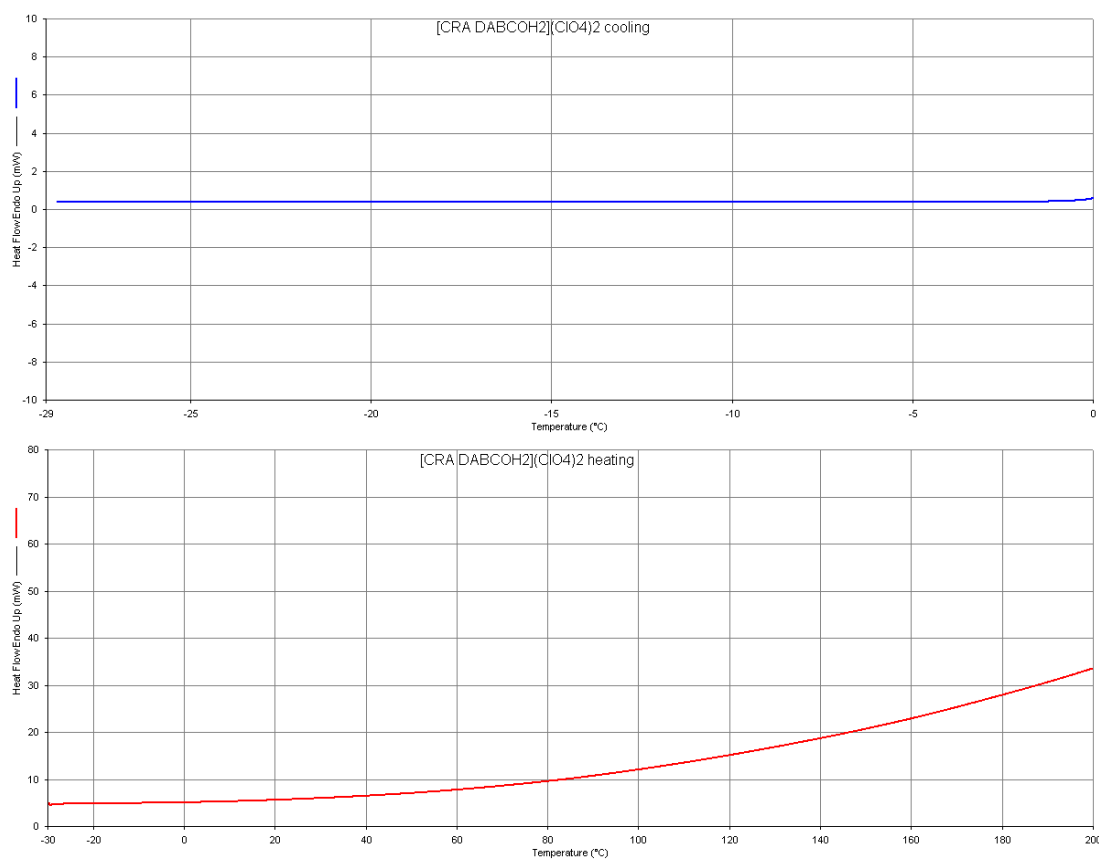


Figure SI-10 DSC track of [(12-crown-4)₂-DABCOH₂](ClO₄)₂; cooling (top) and heating ramp (bottom).

References

- (1) Gavezzotti, A.; Simonetta, M. Crystal Chemistry in Organic Solids. *Chem. Rev.* **1982**, *82* (1), 1–13.
- (2) Dunitz, J. D.; Schomaker, V.; Trueblood, K. N. Interpretation of Atomic Displacement Parameters from Diffraction Studies of Crystals. *Journal of Physical Chemistry*. American Chemical Society February 1988, pp 856–867.
- (3) Braga, D. Dynamical Processes in Crystalline Organometallic Complexes. *Chem. Rev.* **1992**, *92* (4), 633–665.
- (4) Yannoni, C. S.; Johnson, R. D.; Meijer, G.; Bethune, D. S.; Salem, J. R. ¹³C NMR Study of the C₆₀ Cluster in the Solid State: Molecular Motion and Carbon Chemical Shift Anisotropy. *J. Phys. Chem.* **1991**, *95* (1), 9–10.
- (5) Tycko, R.; Dabbagh, G.; Fleming, R. M.; Haddon, R. C.; Makhija, A. V.; Zahurak, S. M. Molecular Dynamics and the Phase Transition in Solid C₆₀. *Phys. Rev. Lett.* **1991**, *67* (14), 1886–1889.
- (6) Bürgi, H. B. Motion and Disorder in Crystal Structure Analysis: Measuring and Distinguishing Them. *Annu. Rev. Phys. Chem.* **2000**, *51* (1), 275–296.
- (7) Painter, J.; Merritt, E. A. Optimal Description of a Protein Structure in Terms of Multiple Groups Undergoing TLS Motion. *Acta Crystallogr. Sect. D Biol. Crystallogr.* **2006**, *62* (4), 439–450.
- (8) Setaka, W.; Yamaguchi, K. Thermal Modulation of Birefringence Observed in a Crystalline Molecular Gyrotop. *Proc. Natl. Acad. Sci.* **2012**, *109* (24), 9271–9275.
- (9) Akutagawa, T.; Koshinaka, H.; Sato, D.; Takeda, S.; Noro, S.; Takahashi, H.; Kumai, R.; Tokura, Y.; Nakamura, T. Ferroelectricity and Polarity Control in Solid-State Flip-Flop Supramolecular Rotators. *Nat. Mater.* **2009**, *8* (4), 342–347.
- (10) Katrusiak, A.; Szafranski, M. Ferroelectricity in NH⁺⋯N Hydrogen Bonded Crystals. *Phys. Rev. Lett.* **1999**, *82* (3), 576–579.
- (11) Bracco, S.; Beretta, M.; Cattaneo, A.; Comotti, A.; Falqui, A.; Zhao, K.; Rogers, C.; Sozzani, P. Dipolar Rotors Orderly Aligned in Mesoporous Fluorinated Organosilica Architectures. *Angew. Chemie - Int. Ed.* **2015**, *54* (16), 4773–4777.
- (12) Bracco, S.; Castiglioni, F.; Comotti, A.; Galli, S.; Negroni, M.; Maspero, A.; Sozzani, P. Ultrafast Molecular Rotors and Their CO₂ Tuning in MOFs with Rod-Like Ligands. *Chem. - A Eur. J.* **2017**, *23* (47), 11210–11215.
- (13) Hutchins, K. M.; Groeneman, R. H.; Reinheimer, E. W.; Swenson, D. C.; MacGillivray, L. R. Achieving Dynamic Behaviour and Thermal Expansion in the Organic Solid State via Co-Crystallization. *Chem. Sci.* **2015**, *6* (8), 4717–4722.
- (14) Islamov, D. R.; Shtyrlin, V. G.; Serov, N. Y.; Fedyanin, I. V.; Lyssenko, K. A. Symmetry Influence on the Rotation of Molecules in Crystals. *Cryst. Growth Des.* **2017**, *17* (9), 4703–4709.
- (15) Vogelsberg, C. S.; Garcia-Garibay, M. A. Crystalline Molecular Machines: Function, Phase Order, Dimensionality, and Composition. *Chem. Soc. Rev.* **2012**, *41* (5), 1892–1910.
- (16) Comotti, A.; Bracco, S.; Sozzani, P. Molecular Rotors Built in Porous Materials. *Acc. Chem. Res.* **2016**, *49* (9), 1701–1710.
- (17) Jiang, X.; O'Brien, Z. J.; Yang, S.; Lai, L. H.; Buenaflor, J.; Tan, C.; Khan, S.; Houk, K. N.; Garcia-Garibay, M. A. Crystal Fluidity Reflected by Fast Rotational Motion at the Core, Branches, and Peripheral Aromatic Groups of a Dendrimeric Molecular Rotor. *J. Am. Chem. Soc.* **2016**, *138* (13), 4650–4656.
- (18) Howe, M. E.; Garcia-Garibay, M. A. The Roles of Intrinsic Barriers and Crystal Fluidity in Determining the Dynamics of Crystalline Molecular Rotors and Molecular Machines. *J. Org. Chem.* **2019**, *84* (16), 9835–9849.
- (19) d'Agostino, S.; Fornasari, L.; Grepioni, F.; Braga, D.; Rossi, F.; Chierotti, M. R.; Gobetto, R. Precessional Motion in Crystalline Solid Solutions of Ionic Rotors. *Chem. - A Eur. J.* **2018**, *24* (56), 15059–15066.
- (20) Katrusiak, A. High-Pressure Crystallography. *Acta Crystallogr. Sect. A Found. Crystallogr.* **2008**, *64* (1), 135–148.
- (21) Olejniczak, A.; Ostrowska, K.; Katrusiak, A. H-Bond Breaking in High-Pressure Urea. *J. Phys. Chem. C* **2009**, *113* (35), 15761–15767.

- (22) Olejniczak, A.; Katrusiak, A.; Szafranski, M. Ten Polymorphs of NH + ···N Hydrogen-Bonded 1,4-Diazabicyclo[2.2.2]Octane Complexes: Supramolecular Origin of Giant Anisotropic Dielectric Response in Polymorph V. *Cryst. Growth Des.* **2010**, *10* (8), 3537–3546.
- (23) Olejniczak, A.; Katrusiak, A. Pressure Induced Transformations of 1,4-Diazabicyclo[2.2.2]Octane (Dabco) Hydroiodide: Diprotonation of Dabco, Its N-Methylation and Co-Crystallization with Methanol. *CrystEngComm* **2010**, *12* (9), 2528.
- (24) Cai, W.; Katrusiak, A. Giant Negative Linear Compression Positively Coupled to Massive Thermal Expansion in a Metal-Organic Framework. *Nat. Commun.* **2014**, *5*.
- (25) Marciniak, J.; Katrusiak, A. Direct and Inverse Relations between Temperature and Pressure Effects in Crystals: A Case Study on o-Xylene. *J. Phys. Chem. C* **2017**, *121* (40), 22303–22309.
- (26) Piermarini, G. J.; Block, S.; Barnett, J. D.; Forman, R. A. Calibration of the Pressure Dependence of the R1 Ruby Fluorescence Line to 195 Kbar. *J. Appl. Phys.* **1975**, *46* (6), 2774–2780.
- (27) Mao, H. K.; Xu, J.; Bell, P. M. Calibration of the Ruby Pressure Gauge to 800 Kbar under Quasi-Hydrostatic Conditions. *J. Geophys. Res.* **1986**, *91* (B5), 4673.
- (28) Sheldrick, G. M. SHELXT - Integrated Space-Group and Crystal-Structure Determination. *Acta Crystallogr. Sect. A Found. Crystallogr.* **2015**, *71* (1), 3–8.
- (29) Dolomanov, O. V.; Bourhis, L. J.; Gildea, R. J.; Howard, J. A. K.; Puschmann, H. OLEX2: A Complete Structure Solution, Refinement and Analysis Program. *J. Appl. Crystallogr.* **2009**, *42* (2), 339–341.
- (30) Budzianowski, A.; Katrusiak, A. High-Pressure Crystallographic Experiments with a CCD-Detector. In *High-Pressure Crystallography*; Springer Netherlands, 2004; pp 101–112.
- (31) Macrae, C. F.; Bruno, I. J.; Chisholm, J. A.; Edgington, P. R.; McCabe, P.; Pidcock, E.; Rodriguez-Monge, L.; Taylor, R.; Van De Streek, J.; Wood, P. A. Mercury CSD 2.0 - New Features for the Visualization and Investigation of Crystal Structures. *J. Appl. Crystallogr.* **2008**, *41* (2), 466–470.
- (32) Bielecki, A.; Burum, D. P. Temperature Dependence of 207 Pb MAS Spectra of Solid Lead Nitrate. An Accurate, Sensitive Thermometer for Variable-Temperature MAS. *J. Magn. Reson. Ser. A* **1995**, *116*, 215–220.
- (33) van Gorkom, L. C. M.; Hook, J. M.; Logan, M. B.; Hanna, J. V.; Wasylishen, R. E. Solid-State Lead-207 NMR of Lead(II) Nitrate: Localized Heating Effects at High Magic Angle Spinning Speeds. *Magn. Reson. Chem.* **1995**, *33* (10), 791–795.
- (34) Takahashi, T.; Kawashima, H.; Sugisawa, H.; Toshihide Baba. 207Pb Chemical Shift Thermometer at High Temperature for Magic Angle Spinning Experiments. *Solid State Nucl. Magn. Reson.* **1999**, *15* (2), 119–123.
- (35) Guan, X.; Stark, R. E. A General Protocol for Temperature Calibration of MAS NMR Probes at Arbitrary Spinning Speeds. *Solid State Nucl. Magn. Reson.* **2010**, *38* (2–3), 74–76.
- (36) Ratcliffe, C. I.; Buchanan, G. W.; Denike, J. K. Dynamics of 12-Crown-4 Ether in Its LiNCS Complex As Studied by Solid-State 2H NMR. *J. Am. Chem. Soc.* **1995**, *117* (10), 2900–2906.
- (37) Buchanan, G. W.; Moghimi, A.; Ratcliffe, C. I. Molecular Motion in Crown Ethers. Application of 13C and 2H NMR to the Study of 4-Carboxybenzo-24-Crown-8 Ether and Its KNCS Complex in Solution and in the Solid Phase. *Can. J. Chem.* **1996**, *74* (613), 1437–1446.
- (38) Catalano, L.; Pérez-Estrada, S.; Terraneo, G.; Pilati, T.; Resnati, G.; Metrangolo, P.; Garcia-Garibay, M. A. Dynamic Characterization of Crystalline Supramolecular Rotors Assembled through Halogen Bonding. *J. Am. Chem. Soc.* **2015**, *137* (49), 15386–15389.
- (39) Catalano, L.; Perez-Estrada, S.; Wang, H.; Ayitou, A. J.-L.; Khan, S. I.; Terraneo, G.; Metrangolo, P.; Brown, S.; Garcia-Garibay, M. A. Rotational Dynamics of Diazabicyclo[2.2.2]Octane in Isomorphous Halogen-Bonded Co-Crystals: Entropic and Enthalpic Effects. *J. Am. Chem. Soc.* **2017**, *139* (2), 843–848.

3.4 Binary and Ternary Solid Solutions of Ionic Plastic Crystals, and Modulation of Plastic Phase Transitions

Reproduced with permission from [d'Agostino, S.; Fornasari, L.; Braga, D. *Cryst. Growth Des.* **2019**, acs.cgd.9b00751.] Copyright [2019] American Chemical Society.
<https://doi.org/10.1021/acs.cgd.9b00751>

3.4.1 Introduction

Plastic crystals¹ are a family of materials characterized by disorder–order transitions that show great potential for the realization of a variety of functional materials. More specifically, organic ionic plastic crystals (OIPCs) have received much attention over the past few decades since they may have applications as solid-state electrolytes in fuel cells, batteries, and capacitors.^{2–4}

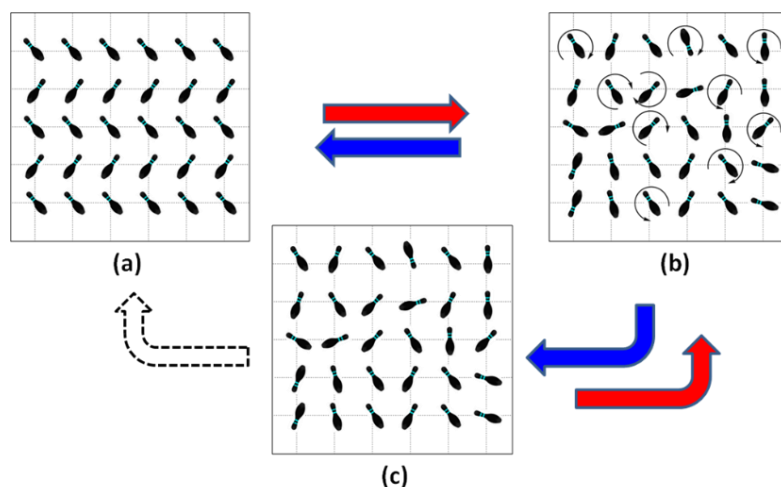
They are a type of solids in which molecular ions exhibit rotational and/or reorientational disorder, while their centers of mass occupy the ordered sites of the crystal structure;^{5,6} thus, they feature long-range order but short-range dynamical disorder. These crystal phases are also known as rotator or rotary phases.^{3,6}

Crystals made up of globular molecules and ions are prone to manifest reversible phase transitions from ordered crystalline phases to dynamically disordered structures (rotator or plastic phases) with temperature changes, which, in turn, may give rise to a reversible glassy-plastic transition when warmed and cooled again.² Scheme 3.4.1 depicts the possible transition pathways for these systems.

Salts of bulky or planar cations such as imidazolium,^{7–9} quinuclidinium,^{10,11} and metallocenium^{2,12} are widely used for the production of such materials since they frequently exhibit plastic phases at high temperatures owing to the globular shapes of the cations.

A simple, though efficient, strategy to realize OIPCs relies on a neutralization reaction from a Brønsted acid to a Brønsted base; a further step in the design is that of replacing the anion/cation through exchange reactions. However, it remains somewhat challenging to predict a priori which combination of cation and anion will work in giving salts that provide a rotator/plastic phase before melting or degradation of the material occurs as well as the transition temperature at which molecular motion starts or stops.² Therefore, the search for new design strategies that expand and modulate the

plastic phase transition and temperature range of stability is at the cutting edge in this field.



Scheme 3.4.1 Representation of the possible transitions among solid phases: (a) the ordered phase (O), (b) the dynamically disordered structure corresponding to a plastic phase (P), and (c) the statically disordered structure corresponding to a glassy phase (G).

Recently, crystalline solid solutions, which are defined as nonstoichiometric multicomponent crystals in which two, or even more, components combine homogeneously in a single-crystalline phase with random occupancy of the unit cell sites,^{13–15} have attracted researchers' attention as a promising tool for the modification of the physicochemical properties of materials. Successful examples include modulation of enantioselectivity,^{16,17} melting point,^{15,18} polymorphic phase transition,^{19,20} and the thermosalient effect,²¹ among others.

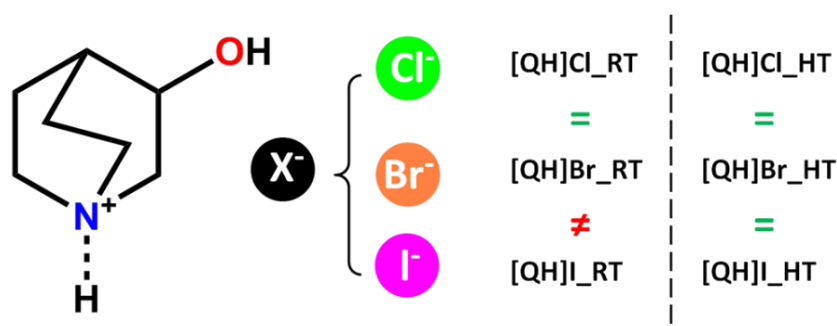
The key prerequisite for the formation of a solid solution is the mutual miscibility of the components, which in turn depends on the concepts of structural similarity in terms of size and shape. The pure components should, ideally, be isomorphous, or at least isostructural or quasi-isostructural, and according to Kitaigorodsky display a difference less than 15% in size.^{14,15,13}

The purpose of this study was 2-fold: on one side, we were interested in exploring the possibility of preparing binary and ternary solid solutions of crystalline systems, and second, in investigating how the composition of the resulting materials affects both the type and phase transition temperature of mixed systems with respect to the pure parent materials.

To this end, we have selected a series of molecular salts with the general formula [QH]X, where [QH]⁺ is the (*R*)-3-hydroxyquinuclidinium cation, and

the inorganic anion X^- is Cl^- and Br^- . These compounds are known to undergo a reversible order–disorder transition above RT that leads to a plastic phase, to which a paraelectric–ferroelectric phase transition is also coupled.¹⁰ [QH]Cl and [QH]Br were reported to exist in two polymorphic modifications that interconvert reversibly by temperature variations: a tetragonal phase at RT and a cubic one at HT; the former corresponds to the ordered crystal structure, while the latter is dynamically disordered and corresponds to a plastic phase.

We have also synthesized the novel salt (*R*)-3-hydroxyquinuclidinium iodide, [QH]I. [QH]I crystallizes as two enantiotropically related polymorphs: an ordered monoclinic phase at RT, not isomorphous to the RT structure of [QH]Cl and [QH]Br, and a dynamically disordered (plastic) structure at HT that is isomorphous to the HT phases of [QH]Cl and [QH]Br; see Scheme 3.4.2.



Scheme 3.4.2 Molecular structures of the molecular salts chosen as components for the preparation of binary and ternary crystalline solid solutions. The symbols =, and ≠ indicate isomorphism and non-isomorphism of the crystal phases, respectively.

By exploiting crystal engineering design principles,^{22,23} we attempted the preparation of binary and ternary mixed crystalline systems.

The synthesized materials were thoroughly characterized by a combination of solid-state techniques including variable-temperature single-crystal powder X-ray diffraction (XRD), thermogravimetric analysis (TGA), and differential scanning calorimetry (DSC).

The combined use of these methods has made possible to find out that, in the solid state, [QH]Cl and [QH]Br are fully miscible in the whole range of composition as they afford binary solid solutions with the general formula $[QH]Cl_xBr_{1-x}$, whereas for the couple [QH]Br and [QH]I and as well as for [QH]Cl and [QH]I it is still possible to achieve binary mixed systems of the type $[QH]Br_yI_{1-y}$ and $[QH]I_zCl_{1-z}$, but with limits in term of composition.

Finally, ternary solutions with the general formula $[\text{QH}]\text{Cl}_x\text{Br}_y\text{I}_z$, where $x, y, z = 0-1$ and $x + y + z = 1$, have also been obtained and characterized.

3.4.2 Experimental section

Synthesis. (*R*)-3-Hydroxyquinuclidinol hydrochloride, $[\text{QH}]\text{Cl}$, and (*R*)-3-hydroxyquinuclidinol were purchased from Sigma-Aldrich and FluoroChem, respectively, and used without further purification. Reagent grade solvents (from Sigma-Aldrich) and bi-distilled water were used.

$[\text{QH}]\text{Br}$ and $[\text{QH}]\text{I}$: 200 mg of (*R*)-3-hydroxyquinuclidinol was dissolved in ca. 5 mL of water and neutralized with the respective HX acid,¹⁰ undissolved material was filtered off, and the resulting solutions were left to slowly evaporate in the dark. The crystalline material so-obtained was sticky and needed purification via washing with abundant diisopropylether.

Binary and ternary solid solutions: the reactants were weighed in the proper stoichiometric ratio (see Table SI-1), dissolved in ca. 5 mL of water. The resulting solutions were sonicated up to complete dissolution and left to slowly evaporate in the dark. Crystalline materials were obtained upon complete evaporation of the solvent.

Single crystal X-ray diffraction. Single-crystal data for all salts were collected on an Oxford X'Calibur S CCD diffractometer equipped with a graphite monochromator (Mo-K α radiation, $\lambda = 0.71073 \text{ \AA}$) and with a cryostat Oxford CryoStream800. Data collection and refinement details are listed in Table SI-2. All non-hydrogen atoms were refined anisotropically. H_{CH} atoms for all compounds were added in calculated positions and refined riding on their respective carbon atoms; H_{OH} and H_{NH} atoms were either directly located or, when not possible, added in calculated positions. SHELX97²⁴ was used for structure solution and refinement on F². The program Mercury²⁵ was used for molecular graphics and to calculate intermolecular interactions. Crystal data can be obtained free of charge via www.ccdc.cam.ac.uk/conts/retrieving.html (or from the Cambridge Crystallographic Data Centre, 12 Union Road, Cambridge CB21EZ, UK; fax: (+44)1223-336-033; or e-mail: deposit@ccdc.cam.ac.uk). CCDC nos. [1917859](#)–[1917862](#).

Powder X-ray diffraction. For phase identification and variable-temperature X-ray powder diffraction diffractograms were performed on a PANalytical X'Pert Pro automated diffractometer equipped with an X'Celerator detector in Bragg–Brentano geometry, using Cu–K α radiation ($\lambda = 1.5418 \text{ \AA}$) without monochromator in the 2θ range between 3° and 40° (continuous scan mode, step size 0.0167° , counting time 19.685 s, Soller slit 0.04 rad, antiscatter slit 1/2, divergence slit 1/4, 40 mA · 40 kV) and an Anton-Paar TTK 450+LNC. The program Mercury²⁵ was used for the calculation of X-ray powder patterns on the basis of single-crystal data either retrieved from the Cambridge structural database (CSD) ([QH]Cl_RT - SIYWUT01, [QH]Cl_HT - SIYWUT02, and [QH]Br_RT - ABIQOU) or collected in this work. Chemical and structural identities between bulk materials and single crystals were always verified by comparing experimental and calculated powder diffraction patterns (see Supporting Information). For Pawley refinement and pattern indexing purposes, diffractograms in the 2θ range $3\text{--}70^\circ$ (step size, 0.026° ; time/step, 200 s; 0.02 rad soller; $V \times A$ 40×40) were collected on a Panalytical X'Pert PRO automated diffractometer operated in transmission mode (capillary spinner) and equipped with a Pixel detector. Powder diffraction data were analyzed with the software TOPAS 4.1.²⁶ A shifted Chebyshev function with six parameters was used to fit background. See Supporting Information for the difference patterns and the corresponding figures of merit.

Thermogravimetric analysis. TGA analyses were performed with a PerkinElmer TGA-7. Each sample, contained in a platinum crucible, was heated in a nitrogen flow ($20 \text{ cm}^3 \text{ min}^{-1}$) at a rate of $5 \text{ }^\circ\text{C min}^{-1}$, up to decomposition. Samples weights were in the range 5–10 mg.

Differential scanning calorimetry. Calorimetric measurements were performed with a PerkinElmer DSC-7 equipped with a PII intracooler. Temperature and enthalpy calibrations were performed using high-purity standards (*n*-decane, benzene, and indium). Heating of the aluminum open pans containing the samples (3–5 mg) was carried out at $5 \text{ }^\circ\text{C min}^{-1}$ in the temperature range $-30\text{--}200 \text{ }^\circ\text{C}$.

Hot stage and cross-polarized optical microscopy (HSM-CP). Hot Stage experiments were carried out using a Linkam TMS94 device connected to a

Linkam LTS350 platinum plate and equipped with polarizing filters. Images and movies were collected with the imaging software VisiCam Analyzer, from an Olympus BX41 stereomicroscope.

3.4.3 Results and discussion

In order to facilitate the description of the experimental results, the following section is organized with reference to the solid solutions ternary diagram, from single phase (vertices), to binary phases (sides) to the ternary phases (core). Ternary diagrams will be used to show the relationship between the compositions of the binary and ternary solid solutions and the plastic transition temperature.

Vertices of triangle - crystal structure and thermal behavior of the [QH]X salts

At room temperature, (*R*)-3-hydroxyquinuclidinium hydrochloride and hydrobromide are isomorphous (from now on, we will refer to these phases as [QH]Cl_RT and [QH]Br_RT); they crystallize in the tetragonal space group $P4_1$. Both crystals feature infinite head-to-tail chains, held by charge-assisted hydrogen bonds, that run along the a -axis direction, and in which the (*R*)-3-hydroxyquinuclidinium cations alternate with the halide anions; weak C–H \cdots X⁻ interactions are also present. See Figure 3.4.1 and Table SI-3 for distance list.

According to the literature,¹⁰ upon increasing the temperature, both [QH]Cl_RT and [QH]Br_RT undergo a transition from an ordered tetragonal phase to a plastic cubic phase at the temperatures of 67 and 50 °C, respectively, and which we will refer to as [QH]Cl_HT and [QH]Br_HT. Interestingly, such transformations take place via single-crystal to single-crystal (SCSC) transition, *vide infra*.

On the other hand, at RT (*R*)-3-hydroxyquinuclidinium hydroiodide, [QH]I_RT, is not isostructural and isomorphous to the hydrochloride and hydrobromide analogous salts since it forms a complex net of charge-assisted hydrogen bonds between the [QH]⁺ cations and I⁻ anions (Figure 3.4.1) and hydrogen bonds between the OH groups.

Moreover, [QH]I_RT crystallizes in the monoclinic space group $P2_1$ with four I⁻ anions and four [QH]⁺ cations in the asymmetric unit ($Z' = 4$). One of the (*R*)-3-hydroxyquinuclidium is disordered over two positions. To dispel any doubt about the type of disorder affecting this cation, we also carried out a variable-temperature single-crystal XRD experiment and found that at low temperature (100 K) all the (*R*)-3-hydroxyquinuclidinium cations are perfectly ordered, and the disorder is restored when the structure is brought back at RT. This might imply that in [QH]I_RT the disorder of the cationic unit is substantially due to a reorientational motion between the two position; see Figure 3.4.2.

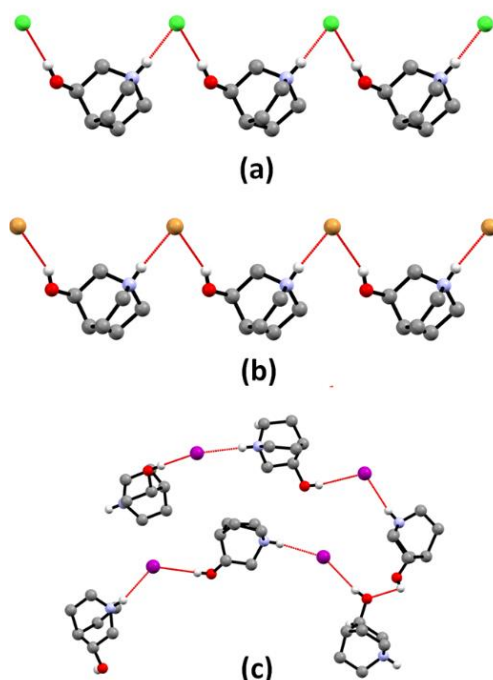


Figure 3.4.1 Intermolecular interactions in crystalline: (a) [QH]Cl_RT, (b) [QH]Br_RT, and (c) [QH]I_RT. H_{CH} atoms are omitted for clarity.

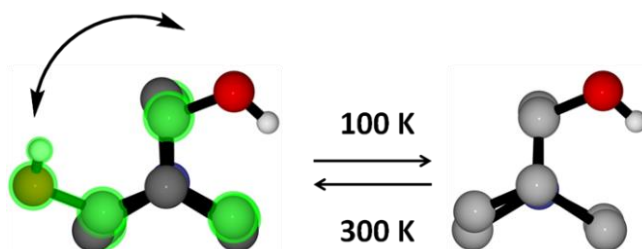


Figure 3.4.2 Representation of flip-flop of one of the [QH]⁺ cation present in the crystal structure of [QH]I_RT induced by temperature variation. H_{CH} omitted for clarity.

A polycrystalline sample of [QH]I was also subjected to thermal analyses. The TGA measurement reveals a good thermal stability up to 250 °C (Supporting Information), while DSC indicates a reversible phase transition at around 70 °C (peak maximum) (Supporting Information).

As anticipated above, we refer to the phases below and above the transition temperature as [QH]I_RT and [QH]I_HT, respectively. To probe the structural information of the high-temperature phase, both the variable-temperature single-crystal and powder X-ray diffractions were measured.

Differently to what was observed in the case of [QH]Cl and [QH]Br, in the case of [QH]I, the transition RT \leftrightarrow HT is accompanied by a collapse of the single crystals; this was confirmed also by cross-polarized hot stage microscopy (see movie in Supporting Information for a comparison). A possible explanation might be as follows: with the onset of the dynamic disorder, the crystal packing undergoes a marked rearrangement in terms of the anions' and cations' positions that have to "flow" through the lattice to minimize the ionic interactions. As a consequence, the generated stress is not released and provokes the cleavage of crystal planes, leading thus to a polycrystalline sample. For [QH]Cl and [QH]Br, such a rearrangement does not need to occur, or at least not markedly, as in their ordered crystal phases the anions and cations are already suitably in place to minimize the ionic interaction also in the plastic phase.

Interestingly, the powder pattern recorded at 70 °C shows fewer peaks with respect to one recorded at RT, this information fully agrees with the increase in symmetry accompanying the transition to a plastic phase, and it is in line with what observed in the case of the hydrochloride and hydrobromide analogous salts. Additionally, for [QH]I, the high-temperature pattern strongly resembles the ones of [QH]Cl and [QH]Br recorded at 75 and 60 °C, respectively. For [QH]I_HT, we were also able to index and refine a cubic unit cell with $a = 10.02(1)$ Å, $V = 1007.6(3)$ Å³, and $F432$ as the most plausible space group.

Therefore, we can conclude that the three salts are all isomorphous and isostructural once the transition to the respective plastic phases has taken place. Figure 3.4.3 shows a comparison of the variable-temperature powder X-ray diffraction patterns recorded for the three samples.

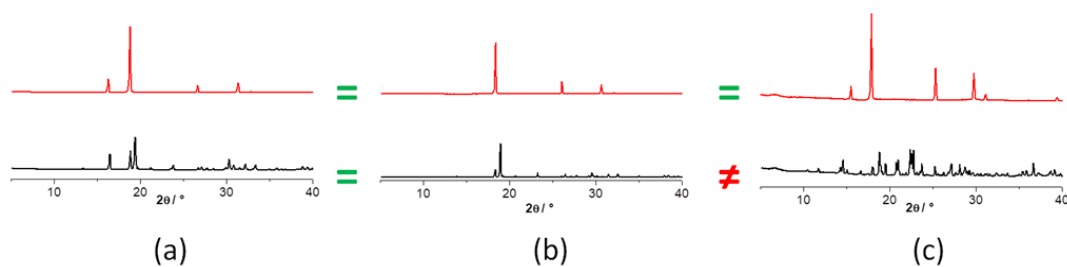


Figure 3.4.3 Variable temperature XRD patterns recorded at RT (black-line) and at high temperature (red-line) for: (a) [QH]Cl, (b) [QH]Br, and (c) [QH]I. The symbols =, and ≠ indicate isomorphism and non-isomorphism of the crystal phases, respectively.

Intrigued by these differences and similarities, in terms of structural and thermal behavior also in view of the increasing ionic radius of the three anions Cl^- (ca. 1.8 \AA^3), Br^- (ca. 1.9 \AA^3), and I^- (ca. 2.2 \AA^3), we decided to investigate the possibility of obtaining binary and ternary mixed-crystal phases. More specifically, we wondered the following: (1) would the three salts, or pairs of them, mix up in single-crystal phases thus forming true solid solutions or would they separate out in crystals of the two/three parent salts? (2) If solid solutions are formed, would they be accessible in the whole range of composition or there are limits? (3) How would the molar ratio of X^- anions in the alloy affect the phase transition behavior?

Sides of triangle - binary solid solutions of the [QH]X salts and thermal behavior

The preparation of the solid solutions of $[\text{QH}]\text{Cl}_x\text{Br}_{1-x}$, $[\text{QH}]\text{Br}_y\text{I}_{1-y}$, and $[\text{QH}]\text{I}_z\text{Cl}_{1-z}$ was obtained by slow evaporation of water solutions containing the three pairs in various stoichiometric ratio (to cover the whole range of composition). TGA, DSC, and PXRD were used to characterize the resulting solids. In some cases, single crystals were also obtained.

Since crystalline [QH]Cl and [QH]Br are isomorphous (see Table SI-2) and the difference in size between the two anions is of ca. 8%, we expected that this pair may form binary solid solutions in the whole range of composition. Indeed, crystallization from water solutions in various stoichiometric ratio affords solid solutions, as confirmed by DSC and PXRD.

A comparison of the experimental XRD patterns recorded at RT on $[\text{QH}]\text{Cl}_x\text{Br}_{1-x}$ solid solutions is shown in Figure 3.4.4. It is possible to appreciate how the patterns progressively change to those of pure components, reflecting thus the change in the unit cell volume.

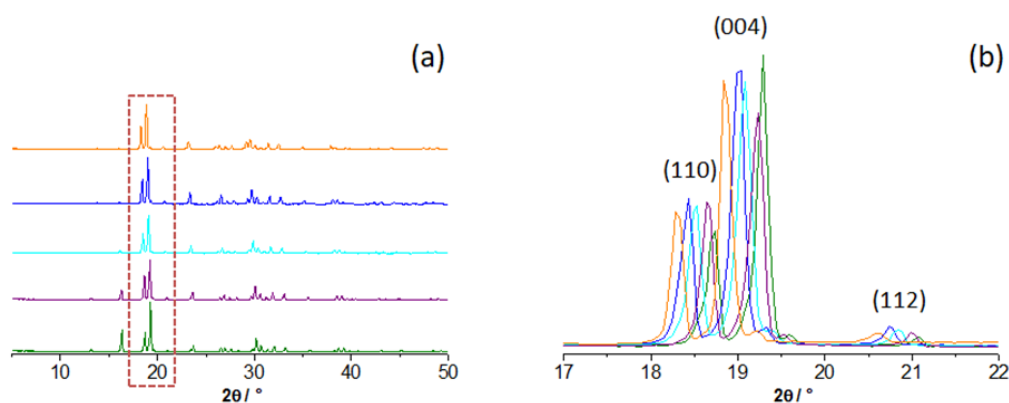


Figure 3.4.4 (a) Comparison of the powder XRD patterns for $[\text{QH}]\text{Cl}_x\text{Br}_{1-x}$ solid solutions: $x=1$ (green-line), $x=0.75$ (purple-line), $x=0.5$ (cyan-line), $x=0.25$ (blue-line), and $x=0$ (orange-line). (b) Detail showing the shifts of the (110), (004) and (112) peaks toward higher angles upon increasing the molar fraction of Cl^- .

Moreover, the DSC of each new crystal phase shows a reversible plastic phase transition with only one peak, pertaining to the solid solution product and not to the two reagents, and with a marked hysteresis. The trend of transition temperature versus composition is reported in Figure 3.4.5 and shows a smooth increase with a minimum for $y = 0.25$.

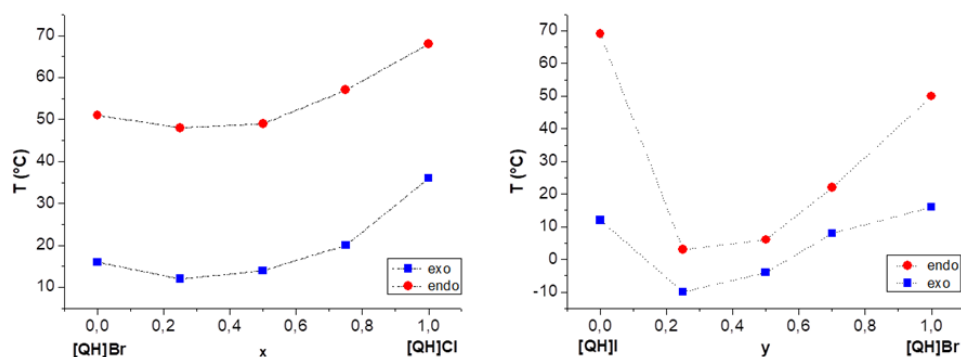


Figure 3.4.5 Temperature variations (from DSC, peak temperatures) of the transitions for the binary solid solutions (a) $[\text{QH}]\text{Cl}_x\text{Br}_{1-x}$ and (b) $[\text{QH}]\text{Br}_y\text{I}_{1-y}$.

In the case of $[\text{QH}]\text{Cl}_{0.5}\text{Br}_{0.5}$, we succeeded in growing single crystals for structural characterization. At RT, crystalline $[\text{QH}]\text{Cl}_{0.5}\text{Br}_{0.5}$ is isomorphous to the parent compounds and with a unit cell that is intermediate; see Table SI-2. When warmed above the transition temperature, $[\text{QH}]\text{Cl}_{0.5}\text{Br}_{0.5}$ also undergoes a reversible SCSC transition to a plastic phase that is a solid solution too and in which the cation is severely affected by dynamic reorientation; see Figure 3.4.6 and movie. Further evidence of the reversibility comes from variable-

temperature X-ray powder diffraction (Figure 3.4.6) performed above and below the transition temperature.

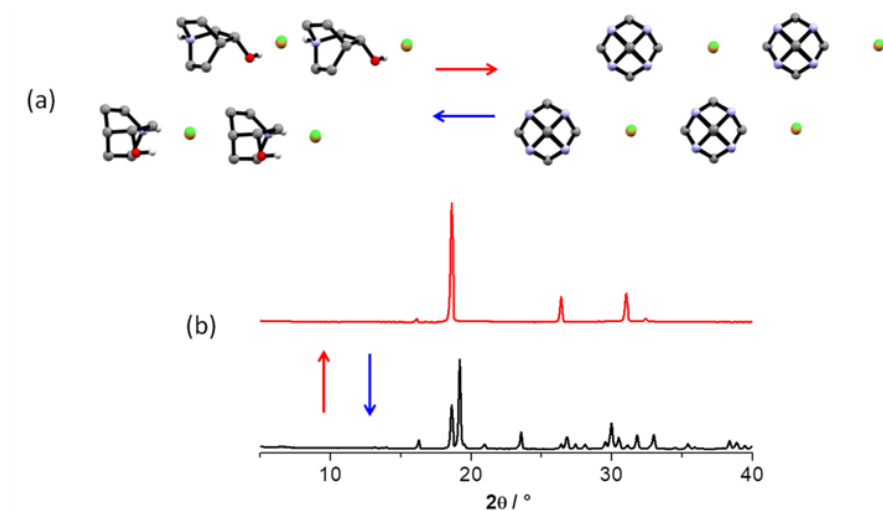


Figure 3.4.6 (a) Representation of the conversion between the RT (top) and HT (bottom) phases, corresponding to the ordered and plastic phases of $[\text{QH}]\text{Cl}_{0.5}\text{Br}_{0.5}$, respectively. H_{CH} omitted for clarity. (b) Variable temperature XRD patterns recorded at RT (black line) and at 55°C (red line) for the solid solution $[\text{QH}]\text{Cl}_{0.5}\text{Br}_{0.5}$.

Analogous investigations were carried out on solid solutions of $[\text{QH}]\text{Br}_y\text{I}_{1-y}$ and $[\text{QH}]\text{I}_z\text{Cl}_{1-z}$. However, contrary to what was observed for $[\text{QH}]\text{Cl}_x\text{Br}_{1-x}$, these two solid solutions showed a quite different behavior from both a structural and thermal point of view. Let us also keep in mind that at RT $[\text{QH}]\text{I}$ is not isomorphous to $[\text{QH}]\text{Cl}$ and $[\text{QH}]\text{Br}$ and that the difference of the anionic radius is of ca. 12% and 21% for the pairs Br^-/I^- and I^-/Cl^- , respectively.

For the pair $[\text{QH}]\text{Br}$ and $[\text{QH}]\text{I}$, mixed crystalline phases were successfully obtained from slow evaporation of solutions containing the two salts approximately in the whole range of composition. While for the pair $[\text{QH}]\text{I}$ and $[\text{QH}]\text{Cl}$, in which the anions possess the highest difference in size, mixed crystalline phases were achieved only for the 50:50 and 75:25 molar ratios, while for the 25:75 composition we obtained invariably a mixture of 50:50 and $[\text{QH}]\text{Cl}_{\text{RT}}$ phases (see Supporting Information for PXRD).

Powder diffraction patterns (Figure 3.4.7) proved the formation of a unique crystalline phase, isomorphous to those of pure HT structures, while for the other stoichiometric ratios, we found mixtures consisting in the phases of solid solution and reactant in excess.

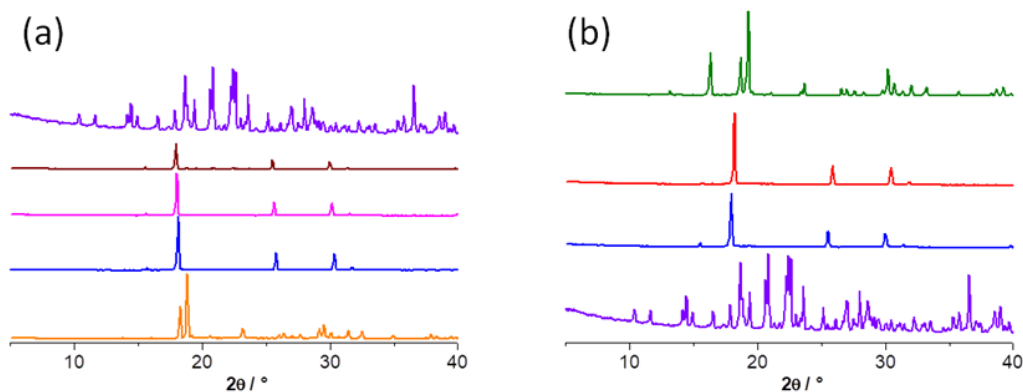


Figure 3.4.7 Comparison of the powder XRD patterns for solid solutions and parent compounds: (a) $[\text{QH}]\text{Br}_y\text{I}_{1-y}$; $y = 1$ (orange line), $y = 0.75$ (blue line), $y = 0.5$ (magenta line), $y = 0.30$ (brown line), and $y = 0$ (purple line), and (b) $[\text{QH}]\text{I}_z\text{Cl}_{1-z}$; $z = 1$ (purple line), $z = 0.75$ (blue line), $z = 0.5$ (red line), and $z = 0$ (green line).

The thermal behavior of each new crystal phase was investigated. DSC traces for $[\text{QH}]\text{Br}_y\text{I}_{1-y}$ with composition $y = 0.75$, 0.5 , and 0.30 show again a reversible transition for all the formed solid solutions (Figure 3.4.5), while for the solid solution $[\text{QH}]\text{I}_z\text{Cl}_{1-z}$ with composition $z = 0.75$ and 0.5 no peaks in DSC were detected; this probably because they fall outside the explored temperature window.

As anticipated above, contrariwise to the mixed system $[\text{QH}]\text{Cl}_x\text{Br}_{1-x}$ the solid solutions $[\text{QH}]\text{Br}_y\text{I}_{1-y}$ and $[\text{QH}]\text{I}_z\text{Cl}_{1-z}$ at RT are already in the plastic phase. Interestingly, upon cooling $[\text{QH}]\text{Br}_y\text{I}_{1-y}$ affords a statically disordered glassy phase. Since no changes are observed in the XRD pattern recorded above and below transition temperature, see Figure 3.4.8, the transition for binary system $[\text{QH}]\text{Br}_{0.5}\text{I}_{0.5}$ may be classified as an isostructural phase transition,^{27,28} while we can only hypothesize a similar behavior for $[\text{QH}]\text{I}_z\text{Cl}_{1-z}$.

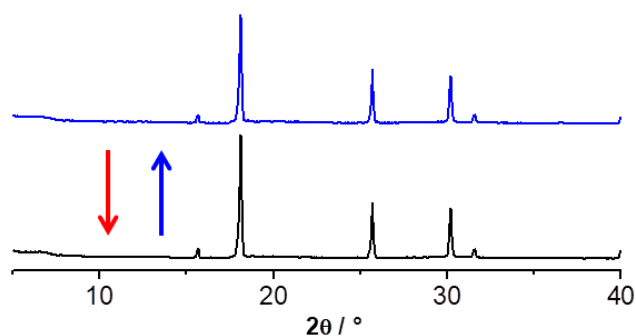


Figure 3.4.8 Variable temperature PXRD patterns of $[\text{QH}]\text{Br}_{0.5}\text{I}_{0.5}$; recorded at RT (black-line) and at -10°C (blue-line).

Core of triangle - ternary solid solutions of the [QH]X salts and thermal behaviour

Finally, we have investigated the propensity of these systems to form a ternary solid solution of general formula $[\text{QH}]\text{Cl}_x\text{Br}_y\text{I}_z$ where $x + y + z = 1$ and $x, y, z = 0-1$. Therefore, we attempted preparation of the ternary systems by slow evaporation of water solutions containing the parent compounds in various stoichiometric ratios.

Powder XRD patterns recorded on the polycrystalline samples revealed the presence of only one phase in all cases. Interestingly, for the compositions $x, y, z = 0.33, 0.33, 0.33$ and $0.2, 0.2, 0.6$ the crystal phases were isomorphous to the plastic (or HT) ones of the parent compounds, while for the compositions $x, y, z = 0.6, 0.2, 0.2$ and $0.2, 0.6, 0.2$ we found phases isomorphous to those of $[\text{QH}]\text{Cl}$ and $[\text{QH}]\text{Br}$ at RT; see Figure 3.4.9.

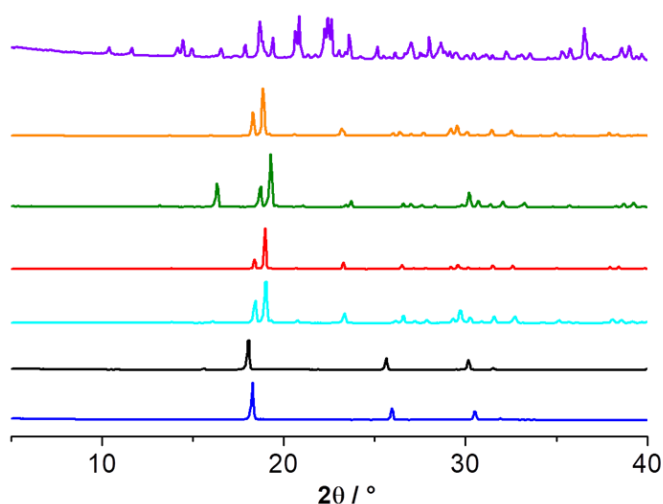


Figure 3.4.9 Comparison of the powder XRD patterns for the ternary solid solutions $[\text{QH}]\text{Cl}_x\text{Br}_y\text{I}_z$ with $x, y, z = 0.33, 0.33, 0.33$ (blue line); $0.2, 0.2, 0.6$ (black line); $0.6, 0.2, 0.2$ (dark cyan line); $0.2, 0.6, 0.2$ (red line), and parent compounds $[\text{QH}]\text{Cl}$ (green line), $[\text{QH}]\text{Br}$ (orange line), and $[\text{QH}]\text{I}$ (purple line).

The thermal behavior of these ternary systems was investigated as well. DSC measurements were quite useful in confirming the formation of ternary solid solutions, as for each phase only one peak was present in the thermogram and at temperatures sensibly lower/different compared to the ones of the parent compounds. As can be seen in the visual representation of the results given in Figure 3.4.10, the transition temperature to the plastic

phase of the solid solutions is lower than those of pure compounds and with a minimum value for the $[\text{QH}]\text{Cl}_{0.33}\text{Br}_{0.33}\text{I}_{0.33}$ composition.

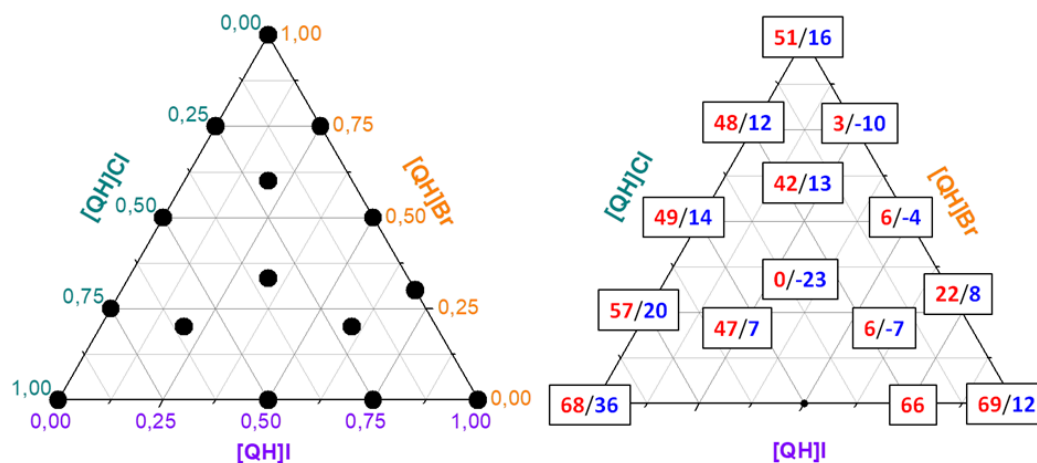


Figure 3.4.10 Ternary diagrams showing compositions of the binary and ternary solid solutions (left) and the corresponding plastic transition temperature (right). Red and blue colors indicate endothermic and exothermic peaks ($^{\circ}\text{C}$), respectively.

To assess whether an ordered or glassy phase can be obtained upon cooling the ternary solid solution, we performed variable temperature powder XRD measurements on a polycrystalline sample of $[\text{QH}]\text{Cl}_{0.33}\text{Br}_{0.33}\text{I}_{0.33}$. In this case, the XRD pattern recorded below the transition temperature shows a diffraction pattern very similar to those of $[\text{QH}]\text{Cl}_{\text{RT}}$ and $[\text{QH}]\text{Br}_{\text{RT}}$; see Figure 3.4.11. The change is reversible, and the starting plastic phase fully restores when the sample is brought back to RT.

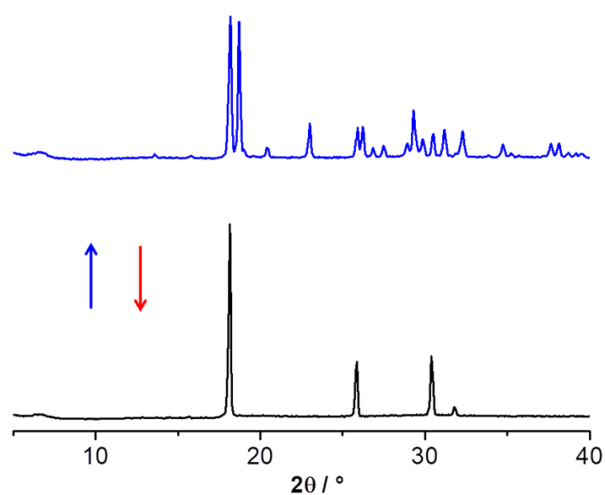


Figure 3.4.11 Variable temperature PXRD patterns of $[\text{QH}]\text{Cl}_{0.33}\text{Br}_{0.33}\text{I}_{0.33}$; recorded at RT (black-line) and at -30°C (blue-line).

For this ternary solid solution, we also succeeded in obtaining single-crystal specimens for which it was possible to follow the transition with HSM (see movie). However, the increased complexity of the system prevented a detailed structural investigation both at RT and LT.

3.4.4 Conclusions

It would be highly desirable to be able to tune solid state properties of materials by choosing the molecular/ionic building blocks, which is at the core of the crystal engineering paradigm. These prospects increase considerably if one can take advantage of the possibility of mixing different ionic/molecular species within the solid without the limitations imposed by integral stoichiometry, i.e., by preparing solid solutions. In so doing, properties of the resulting solid can, at least in principle, be controlled just by adding or decreasing the amount of certain components.

We have been able to modulate plastic transitions in the solid solutions formed by the ferroelectric salts (*R*)-3-hydroxyquinuclidinium chloride and bromide, [QH]Cl and [QH]Br. Mixed crystals of formula [QH]Cl_xBr_{1-x} have been prepared over the entire compositional range. The non-isostructural iodide analogue [QH]I has also been investigated. In spite of the structural differences, binary solid solutions [QH]I_zCl_{1-z} and [QH]Br_yI_{1-y} as well as the ternary solid solutions [QH]Cl_xBr_yI_z ($x + y + z = 1$ and $x, y, z = 0-1$) could be obtained. All solid solutions were characterized by a combination of single-crystal and powder XRD, DSC, and TGA techniques. The [QH]Cl_xBr_{1-x} solutions show a reversible order-disorder transition, while [QH]I_zCl_{1-z} and [QH]Br_yI_{1-y} undergo an unusual first-order transition from the plastic phase to a glassy low-temperature phase. The ternary solid solutions, on the other hand, display more complex behavior depending on the relative quantities of the components. It has been possible to rationalize the results on the basis of the structural differences between the components, providing a simple criterion for the engineering of these plastic phase transitions.

In conclusion, this study has afforded further insights into the subtle interplay between crystal structure and size of the component ions in determining phase stability and the trends in phase transition, especially in the ternary cases. Our aim is to extend our approach to other organic ionic

plastic crystals (OIPCs) that exhibit rotational and/or reorientational disorder systems where properties can be adapted to the target by a change in solid solution composition.

References

- (1) Janikowski, J.; Razali, M. R.; Batten, S. R.; MacFarlane, D. R.; Pringle, J. M. Organic ionic plastic crystals and low viscosity ionic liquids based on the dicyano(nitroso) methanide anion. *Chempluschem* **2012**, *77*, 1039–1045.
- (2) Mochida, T.; Ishida, M.; Tominaga, T.; Takahashi, K.; Sakurai, T.; Ohta, H. Paramagnetic ionic plastic crystals containing the octamethylferrocenium cation: Counteranion dependence of phase transitions and crystal structures. *Phys. Chem. Chem. Phys.* **2018**, *20*, 3019–3028.
- (3) Pringle, J. M.; Howlett, P. C.; MacFarlane, D. R.; Forsyth, M. Organic ionic plastic crystals: Recent advances. *J. Mater. Chem.* **2010**, *20*, 2056–2062.
- (4) Li, B.; Kawakita, Y.; Ohira-Kawamura, S.; Sugahara, T.; Wang, H.; Wang, J.; Chen, Y.; Kawaguchi, S. I.; Kawaguchi, S.; Ohara, K.; et al. Colossal barocaloric effects in plastic crystals. *Nature* **2019**, *567*, 506–510.
- (5) Wang, P.; Dai, Q.; Zakeeruddin, S. M.; Forsyth, M.; MacFarlane, D. R.; Grätzel, M. Ambient temperature plastic crystal electrolyte for efficient, all-solid-state dye-sensitized solar cell. *J. Am. Chem. Soc.* **2004**, *126*, 13590–13591.
- (6) Brand, R.; Lunkenheimer, P.; Loidl, A. Relaxation dynamics in plastic crystals. *J. Chem. Phys.* **2002**, *116*, 10386–10401.
- (7) Luo, J.; Conrad, O.; Vankelecom, I. F. J. Imidazolium methanesulfonate as a high temperature proton conductor. *J. Mater. Chem. A* **2013**, *1*, 2238–2247.
- (8) Pogorzelec-Glaser, K.; Rachocki, A.; Ławniczak, P.; Łapiński, A.; Tritt-Goc, J. Synthesis and characterization of a new proton-conducting material based on imidazole and selenic acid. *Solid State Ionics* **2012**, *227*, 96–101.
- (9) Ggor, A.; Piecha, A.; Jakubas, R.; Miniewicz, A. Crystal structure and characterization of a novel acentric imidazolium analog [C₃N₂H₅⁺][Br⁻]. *Chem. Phys. Lett.* **2011**, *503*, 134–138.
- (10) Li, P. F.; Tang, Y. Y.; Wang, Z. X.; Ye, H. Y.; You, Y. M.; Xiong, R. G. Anomalously rotary polarization discovered in homochiral organic ferroelectrics. *Nat. Commun.* **2016**, *7*, 1–9.
- (11) Yang, C. K.; Chen, W. N.; Ding, Y. T.; Wang, J.; Rao, Y.; Liao, W. Q.; Xie, Y.; Zou, W.; Xiong, R. G. Directional Intermolecular Interactions for Precise Molecular Design of a High- T c Multiaxial Molecular Ferroelectric. *J. Am. Chem. Soc.* **2019**, *141*, 1781–1787.
- (12) Braga, D.; Cojazzi, G.; Paolucci, D.; Grepioni, F. A remarkable water-soluble (molecular) alloy with two tuneable solid-to-solid phase transitions. *Chem. Commun.* **2001**, *9*, 803–804.
- (13) Lusi, M. Engineering Crystal Properties through Solid Solutions. *Cryst. Growth Des.* **2018**, *18*, 3704–3712.
- (14) Fulde, P.; Cardona, M.; Queisser, H. Springer Series in Solid-State Sciences; **1978**.
- (15) Schur, E.; Nauha, E.; Lusi, M.; Bernstein, J. Kitaigorodsky revisited: Polymorphism and mixed crystals of acridine/phenazine. *Chem. - A Eur. J.* **2015**, *21*, 1735–1742.
- (16) Rekis, T.; D'Agostino, S.; Braga, D.; Grepioni, F. Designing Solid Solutions of Enantiomers: Lack of Enantioselectivity of Chiral Naphthalimide Derivatives in the Solid State. *Cryst. Growth Des.* **2017**, *17*, 6477–6485.
- (17) Rekis, T.; Berziņš, A.; Sarceviča, I.; Kons, A.; Balodis, M.; Orola, L.; Lorenz, H.; Actiņš, A. A Maze of Solid Solutions of Pimobendan Enantiomers: An Extraordinary Case of Polymorphism and Solvate Diversity. *Cryst. Growth Des.* **2018**, *18*, 264–273.
- (18) Romasanta, A. K. S.; Braga, D.; Duarte, M. T.; Grepioni, F. How similar is similar? Exploring the binary and ternary solid solution landscapes of p-methyl/chloro/bromo-benzyl alcohols. *CrystEngComm* **2017**, *19*, 653–660.

- (19) Delori, A.; Maclure, P.; Bhardwaj, R. M.; Johnston, A.; Florence, A. J.; Sutcliffe, O. B.; Oswald, I. D. H. Drug solid solutions-a method for tuning phase transformations. *CrystEngComm* **2014**, *16*, 5827–5831.
- (20) d'Agostino, S.; Fornasari, L.; Grepioni, F.; Braga, D.; Rossi, F.; Chierotti, M. R.; Gobetto, R. Precessional Motion in Crystalline Solid Solutions of Ionic Rotors. *Chem. - A Eur. J.* **2018**, *24*, 15059–15066.
- (21) Nauha, E.; Naumov, P.; Lusi, M. Fine-tuning of a thermosalient phase transition by solid solutions. *CrystEngComm* **2016**, *18*, 4699–4703.
- (22) Braga, D.; Grepioni, F.; Maini, L.; d'Agostino, S. From Solid-State Structure and Dynamics to Crystal Engineering. *Eur. J. Inorg. Chem.* **2018**, *2018*, 3597–3605.
- (23) Braga, D.; Grepioni, F.; Maini, L.; D'Agostino, S. Making crystals with a purpose; A journey in crystal engineering at the University of Bologna. *IUCrJ* **2017**, *4*, 369-379.
- (24) Sheldrick, G. M. *SHELXS-97 and SHELXL-97* Program for crystal structure solution and refinement. **1997**.
- (25) Macrae, C. F.; Bruno, I. J.; Chisholm, J. A.; Edgington, P. R.; McCabe, P.; Pidcock, E.; Rodriguez-Monge, L.; Taylor, R.; Van De Streek, J.; Wood, P. A. Mercury CSD 2.0 - New features for the visualization and investigation of crystal structures. *J. Appl. Crystallogr.* **2008**, *41*, 466–470.
- (26) Coelho, A. *TOPAS-Academic*; Coelho Software: Brisbane, Australia, **2007**.
- (27) Rok, M.; Bator, G.; Zarychta, B.; Dziuk, B.; Repeć, J.; Medycki, W.; Zamponi, M.; Usevičius, G.; Šimenas, M.; Banys, J. Isostructural phase transition, quasielastic neutron scattering and magnetic resonance studies of a bistable dielectric ion-pair crystal $[(\text{CH}_3)_2\text{NH}_2]_2\text{KCr}(\text{CN})_6$. *Dalt. Trans.* **2019**, *48*, 4190–4202.
- (28) Boldyreva, E. V.; Sowa, H.; Seryotkin, Y. V.; Drebuschak, T. N.; Ahsbahs, H.; Chernyshev, V.; Dmitriev, V. Pressure-induced phase transitions in crystalline l-serine studied by single-crystal and high-resolution powder X-ray diffraction. *Chem. Phys. Lett.* **2006**, *429*, 474–478.

Chapter 4

Summary

The frame of this doctoral project was the synthesis of novel materials and the improvement of the physicochemical properties of new and existing ones according to the criteria of crystal engineering.

The research activity was dedicated to two main topics, that can be summarised as follows:

1. the design and synthesis of new single-component and multi-component assemblies based on hetero-aryl boronic acids and the investigation of their recognition features;
2. the study of molecular motion in some crystalline complexes and salts and the modification of those dynamics through the principles of crystal engineering.

1. Heteroaryl-boronic acids proved indeed versatile building blocks for crystal engineering, in that a variety of solids could be obtained from accessible starting materials and synthetic methods.

A simple pyridine-appended boronic acid, namely 4-pyridinylboronic acid, was found to undergo a peculiar two-step assembly. Square-shaped tetramers are formed thanks to B-N bonds, the tetramers are then further assembled into layers by means of O-H...O bonds. The crystals displayed a step-and-terrace morphology, typical of the layer-by-layer growth mechanism. They were then exfoliated by means of sonication-assisted liquid-phase exfoliation (LPE). Different morphologies were observed for the different liquid media employed, suggesting a role of the medium in the exfoliation mechanism.

Successively, the cocrystallisation of heteroaryl-boronic acids with H-bonds donor and acceptors was explored to evaluate their tendency to self-assemble as opposed to hetero-assemble. The oxocarbon acids rhodizonic acid and squaric acid were selected as cofomers in view of their propensity to establish H-bonds. The reaction of 4-pyridinylboronic acid and pyrimidine-5-boronic acid with rhodizonic acid lead unexpectedly to condensation products; boronic acid and rhodizonic acid react in a 2:1 molar ratio to form boronic esters with two zwitterionic couples. Two different types of adduct are formed from this esterification: a “tweezer” adduct defined by the conversion of rhodizonic acid in its ortho-dihydrate form, and an “axle” adduct, where instead the rhodizonic acid is converted to a dodecahydroxycyclohexane-like unit. The two types of adduct were obtained concurrently during the crystallisation and their ratio could be modulated by the rate of cooling. Moreover, all the species described

above crystallised in differently hydrate forms; the “tweezers” compounds, specifically, could be dehydrated without compromising the crystallinity of the samples and the mechanism of dehydration was elucidated by X-ray diffraction.

On the other hand, the reaction of 4-pyridinylboronic acid, 3-pyridinylboronic acid and (4-(pyridin-4-yl)phenyl)boronic acid led to the formation of cocrystals defined by the novel supramolecular synthon squarate dianion-boronic acid, held by charge-assisted hydrogen bonds. Again, ionic couples were generated by proton transfer from the squaric acid to the heteroaryl substituent. The supramolecular synthon proved robust enough to be further cocrystallised with 4,4'-bipyridine, forming a three-component system characterized by infinite chains of H-bonded molecules.

2. The supramolecular complexes of formula [(12-crown-4)·DABCOH₂](X)₂ (X=Cl, Br) were synthesised and a reversible first-order phase transition was detected for the two species, that is associated with the onset/offset of a precessional motion of the DABCOH₂²⁺ cation, as established by the combined structural and spectroscopic evidence. This transition has an impact on the symmetry of the crystals and their birefringence. Since the two solids are isostructural and the difference in size between the two anions is sufficiently small ($\approx 15\%$), solid solutions of formula [(12-crown-4)·DABCOH₂]Cl_xBr_{1-x} were successfully prepared over the entire compositional range. The temperature of the transition could be controlled in a range of roughly 20°C through the modification of the solid solution stoichiometry, with the lower temperature achieved in correspondence of the equimolar composition.

The design was further developed for the preparation of the complexes [(12-crown-4)₂·DABCOH₂](X)₂ (X=BF₄, ClO₄). The crystals are highly disordered, with dynamic processes involving the DABCOH₂²⁺ cations and the crown ethers while the anions undergo globular reorientation. [(12-crown-4)₂·DABCOH₂](BF₄)₂ was thus chosen as a model compound for high-pressure studies. Isothermal compression of the crystals was performed in steps by means of a Diamond Anvils Cell (DAC) and the structural modifications were followed with single-crystal XRD. The pressure-induced compression of crystal packing does not eliminate the disorder up to 1.2 GPa, suggesting the presence of complex collective rotations of the crown ethers analogous to meshed gears.

Finally, the chloride, bromide and iodide salts of (R)-3-hydroxyquinuclidinium, [QH]Cl, [QH]Br and [QH]I, are known to possess a

reversible transition between a ferroelectric ordered phase and a paraelectric phase characterised by fast rotational motions of the quinuclidinium molecules. Given the structural similarities between the three salts, the solid-solution approach was again applied; binary and ternary solid solutions were thus obtained, and the composition-dependent field of stability of the paraelectric and ferroelectric phases was mapped. It was observed that the alloying of the salts and the control of their molar ratio allowed the modification of the ferroelectric-paraelectric transition temperature in a predictable fashion over a range of approximately 70°C.

Concluding, the crystal engineering “toolbox” has been successfully employed for the design of solid-state rotors and plastic crystals, as well as the deliberate modification of their dynamical properties. The understanding and control of molecular motions in the solid state could open up to the development of new functional materials.

Acknowledgments

I wish to express my gratitude to my supervisor, Prof. Dario Braga, and my *de facto* co-supervisor, Dr. Simone d'Agostino, for their guidance, support, their enthusiasm and for giving me the chance to pursue my research interests.

This work is the conclusion of a three-years-long process and it would not have been possible without help along the way of a lot of people through collaboration, assistance, discussion, advice. I am deeply thankful to Prof. Roberto Gobetto, Prof. Michele Remo Chierotti and Federica Rossi of the NMR lab in Turin, Prof. Andrzej Katrusiak, Dr. Anna Olejniczak, Aleksandra Pólrolniczak, Szymon Sobczak and the other members of Katrusiak's lab in Poznań who welcomed me for five months, Prof. Elisa Boanini, Dr. Giacomo Bergamini, Dr. Raffaello Mazzaro, Katia Rubini.

I am grateful also to Prof. Fabrizia Grepioni and Prof. Lucia Maini for their encouragement, the discussions and all those small things that they have been teaching me day to day. To Lucia Casali, Oleksii Shemchuk, Chiara Cappuccino, Francesco Marin and the other former students of the Molecular Crystal Engineering group.

In closing, I wish to thank my family and Laura who have been with me all the time.